CONCENTRATION POLARIZATION AND COLLOIDAL FOULING IN THE VIBRATION ENHANCED REVERSE OSMOSIS MEMBRANE DESALINATION SYSTEM

A Dissertation

by

XU SU

Submitted to the Office of Graduate and Professional Studies of
Texas A&M University
in partial fulfillment of the requirements for the degree of

DOCTOR OF PHILOSOPHY

Chair of Committee,	Alan Palazzolo
Committee Members,	Shehab Ahmed
	Sai Lau
	Dion S. Antao
Head of Department,	Andreas A. Polycarpou

December 2018

Major Subject: Mechanical Engineering

ABSTRACT

The focus of this study was on concentration polarization (CP) and colloidal fouling control in the vibration enhanced reverse osmosis desalination system and the fundamentals of centrifugal reverse osmosis (CRO).

A two-dimensional numerical model simulating colloidal particle fouling was proposed aiming at visualizing the process of colloidal fouling accumulation and leading a better understanding of the mechanism of colloidal fouling in a spacer-filled membrane channel. This model predicts the porous cake layer thickness distribution among membrane surface and its effect on the cake enhanced osmotic pressure (CEOP) phenomenon. Results show that colloidal fouling has a huge influence on the membrane performance with up to 47% of the permeate flux decline and 1.77 of the *NaCl* CP modulus within 12 hours.

A novel vibration enhanced reverse osmosis technique was employed to control the concentration polarization phenomenon and colloidal fouling by silica colloids during the reverse osmosis membrane desalination process. Both simulations and experimental results show that membrane performance can be improved by vibration enhanced reverse osmosis technique for all 7 systems investigated in this study. Membrane *NaCl* CP modulus decreases and the permeate flux increases as the vibration frequency increases up to 60 Hz, with a constant vibration amplitude. A maximum 60% improvement of the normalized permeate flux and 25% reduction of the *NaCl* accumulation after 12 hours was found.

In addition, a new CRO concept was proposed to reduce the energy consumption and device size. Results show that the energy cost of the new CRO concept is competitive compared with current medium and large size SWRO systems, while the capital cost is only 0.1% of them. The operation cost is 30% lower compared with the convectional membrane desalination plant. Return on Investment (ROI) study also shows that a total profit over 60k USD and 87% of the ROI can be achieved within 30 years operation of the new CRO system.

The outcomes of this study may lead to a better understanding of the vibration enhanced reverse osmosis desalination process, membrane colloidal fouling simulation and control, and the CRO desalination process.

DEDICATION

To my parents for all their love and encouragement.

ACKNOWLEDGEMENTS

First and foremost, I would like to express my deepest gratitude to my supervisor, Professor Alan Palazzolo. Thank you for giving me the tireless guidance, support and guidance in the last five and half years of study at Texas A&M University. I am gratified and honored for having the opportunity to learn from a person of high caliber and with great knowledge in membrane desalination.

My sincere thanks go to Professor Shehab Ahmed for his encouragement and extensive support during my study. The same thanks are extended to Professor Sai Lau and Professor Dion S. Antao for their guidance of my research and the service as my committee members.

I would also like to thank to Mr. Erwin Thomas for his continuous help on the experimental test rig design and my teammate: Mr. Wende Li, for his three years teamwork. Without their teamwork and effort, this dissertation would not have been possible.

Finally, and most importantly, I would like to thank my parents for their unconditional love, patience, and financial support.

CONTRIBUTORS AND FUNDING SOURCES

This work was supported by the Qatar National Research Fund (NPRP No.: 6-213-2-090, Centrifugal Pressure Vibrating Membrane Reverse Osmosis Desalination and Fracking Waste Water Recovery) and the Water Seed Grant – FY17 sponsored by the State of Texas – State Appropriation.

NOMENCLATURE

u	Velocity component in the x-direction ($m\ s^{-1}$)
v	Velocity component in the y-direction ($m\ s^{-1}$)
x	Axial coordinate (cross-flow direction) (m)
y	Lateral coordinate (channel height direction) (m)
D	Diffusion coefficient ($m^2\ s^{-1}$)
c	Solute concentration ($g\ g^{-1}$)
ΔP	Transmembrane pressure (Pa)
J	Permeate flux ($m\ s^{-1}$)
h	Height (m)
$\bar{u}$	Averaged x-direction velocity ($m\ s^{-1}$)
Re	Reynolds number
a_{acc}	Membrane move acceleration ($m\ s^{-2}$)
r_s	Spacer radius (mm)
k	Boltzmann constant $= 1.38064852 \times 10^{-23}\ m^2\ kg\ s^{-2}\ K^{-1}$
T	Temperature (K)
A_{cell}	Cell bottom face area (m^2)
a	Colloidal silica particle radius (m)
P	Pressure (pa)
m	Fouling mass per unit depth($kg\ m^{-1}$)
TCF	Temperature correction factor
k_t	Coefficient constant used in the TCF equation
R	Hydraulic resistance (m^{-1})
CP	Concentration polarization
l	Membrane length (m)
S	Deposition rate ($kg\ s^{-1}\ m^{-2}$)

$\vec{n}$	Normal direction
f	Vibration frequency (*Hz*)
A	Vibration peak amplitude (*m*)
Δt	Time step (*s*)
$\hat{J}_{t,fHz}$	Normalized permeate flux at time t with f Hz vibration
K	Hydrodynamic permeability ($m^2\ s\ kg^{-1}$)
Sh	Sherwood number
k_m	Mass transfer coefficient ($m\ s^{-1}$)
d_h	Hydraulic diameter (*mm*)
R_{rej}	Membrane intrinsic rejection
V_{tot}	Total channel volume
V_{sp}	Volume occupied by spacers
VBI_i	Refutas index of each component
VBI_β	Refutas index of the blend
T_{per}	Time period (s)
P_{total}	Total power consumption (*W*)
P_{ideal}	Ideal power consumption (*W*)
P_{loss}	Pressure loss power consumption (*W*)
P_f	Bearing friction power consumption (*W*)
r	Centrifuge radius (*m*)
Q_f	Volumetric flow rate of feed water (m^3/s).
P_e	Power collected from high pressure water (*W*)
d_b	Bearing bore diameter (m).
P_b	Equivalent dynamic bearing load (*N*)
F_r	Actual radial bearing load (*N*)
F_a	Actual axial bearing load (*N*)
X	Radial load factor for the bearing
Y	Axial load factor for the bearing

W_c	Weight of the CRO device (*N*)
G	Unit power consumption ($kWh\ m^{-3}$)
ROI	Return on Investment

Greek

μ	Fluid dynamic viscosity (*Pa s*)
ρ	Density ($kg\ m^{-3}$)
π	Solute osmotic pressure (*Pa*)
τ	Cake tortuosity
γ	Shear rate (s^{-1})
Φ	Volume fraction (*L/L*)
α	Specific cake resistance ($m\ kg^{-1}$)
ε	Cake porosity
θ	Fraction of particles deposited
Γ	Concentration polarization modulus
δ_{BLT}	Boundary layer thickness (*mm*)
Λ	Voidage of the spacer-filled membrane channel
ω	Centrifuge angular velocity (*rad/s*)
Γ_d	Angular momentum in the driving process ($kg\ m^2\ s^{-1}$)
Γ_e	Angular momentum in the collection process ($kg\ m^2\ s^{-1}$)
δ	Recovery ratio
Γ_p	Angular momentum in the permeate water ($kg\ m^2\ s^{-1}$)
Γ_f	Frictional moment ($N\ m$)
μ_b	Constant coefficient of friction for the bearing

Subscripts

b	Bulk flow
m	Membrane

n	Solute *NaCl*
c	Colloidal silica particle
0	Initial property without effect of porosity
br	Brownian diffusion
i	Solute i
p	Permeate flow
sh	Shear-induced diffusion
crit	Critical flux
min	Minimum
ch	Channel
rms	Root mean square

TABLE OF CONTENTS

Page

LIST OF FIGURES

Page

LIST OF TABLES

Page

1. INTRODUCTION

1.1. Problem Statement

Drinking water resources have been becoming more and more limited in the world caused by the increased population, industry and agriculture growths, improved living standard, etc. In 2015, member states of the United Nations adopted the '2030 Agenda for Sustainable Development' and proposed the goal that achieving universal and equitable access to safe and affordable drinking water for all by 2030 [1]. However, according to the report from WHO in 2017 [2], 844 million people currently still lack even a basic drinking water service.

Desalination, especially seawater and brackish water desalination, has been proved to be an effective technological solution to meet the fast growing need of fresh drinking water worldwide. Desalination capacity has also been increased rapidly in the last two decades due to the significant reduction in the operation cost benefited from the technological advances.

Desalination technology is becoming an important part or even the main drinking water source in some countries. Qatar relies 100% on the desalinated water for the whole country usage [3]. Currently, the cost of desalinated seawater is lower than 1.00 US$/$m^3$ for a large-scale commercial seawater reverse osmosis membrane desalination plant. In the year 2012, the total global desalination capacity was around 66.4 million m^3/d. 58.9% of the desalinated water source is seawater; while another 21.2% comes from brackish groundwater [4].

Desalination process can be classified into two types: phase change desalination or membrane desalination based on the corresponding separation mechanisms [5]. The phase change desalinations include multistage flash distillation (MSF), multi effect distillation (MED) and vapor compression (VC), etc.; while the membrane desalinations include electrodialysis (ED), reverse osmosis membrane (RO) and ultrafiltration (UF), etc. RO membrane desalination is currently considered as more environmentally friendly (no harmful chemicals used or produced) and energy efficient (energy recovery device installed) than other methods such as MSF and MED. RO membrane desalination system can also be made small and portable to fit offshore individual households filtration system requirement.

A disadvantage of RO membrane desalination method is that the RO membrane is sensitive to membrane fouling caused by particle deposition, scaling, growth of organic solvents, etc. Membrane fouling will cause the permeate flux decline, irreversible membrane degradation, and thus, reduce the membrane lifetime. Commonly encountered colloidal matters in seawater and brackish water treatment processes are difficult to remove by conventional pre-treatment processes. Some small colloids can even pass through the micro-filtration (MF) membrane with 0.2 μm pore size. During the RO membrane desalination process, these colloidal particles can be deposited on the membrane surface and form a porous cake-layer which prevents permeate flux passing through the membrane piece.

Currently, there is a lack of comprehensive simulation model to predict the colloidal fouling evolution and long-term performance of a RO membrane under the

influence of colloidal fouling. The fouling cake layer growth should be non-uniform and highly location dependent due to the complex hydrodynamics and solute concentration distribution inside a spacer-filled membrane channel. The uniform-effective cake layer height assumption is too coarse to evaluate the colloidal fouling details of membrane, especially for spacer-filled membrane system.

In addition to the colloidal fouling prediction model, there is also the need for proposing mechanical method to address the RO membrane concentration polarization and colloidal fouling problem, with the aim of increasing membrane permeate flux, reducing both membrane salt concentration and colloidal fouling.

1.2. Objectives and Scope

The objectives and scope of this research study and the breakdown of the dissertation structure are outlined as follows:

(1) Critically review the available literatures on membrane desalination, concentration polarization (CP), colloidal fouling as well as the membrane fouling control (Chapter 2).

(2) Develop a vibration enhanced reverse osmosis cell desalination test rig to perform experiments.

(3) Develop a CP prediction model for a membrane filtration channel with spacer filaments considered (Chapter 3).

(4) Couple the CP prediction model with the colloidal fouling growth model to predict the membrane colloidal fouling and animate the colloidal fouling layer growth under different operation conditions and feed solutions (Chapter 4).

(5) Simulate membrane CP inside the vibration enhanced RO membrane system and compare with experimental results (Chapter 3).

(6) Simulate membrane colloidal fouling inside the vibration enhanced RO membrane system and compare with experimental results (Chapter 5).

(7) Propose a new centrifuge reverse osmosis (CRO) concept and investigate the power consumption, operation cost and ROI of the new CRO concept (Chapter 6).

1.3. Significance

The significant outcomes of this research are:

(1) A novel vibration enhanced reverse osmosis membrane desalination technique is proposed.

(2) Detailed hydrodynamics were analyzed using transient computational fluid dynamics (CFD) simulation consisting of the fully coupled fluid dynamics and solute transportation governing equations. Concentration dependent fluid properties and axial variation of permeate flux were considered in the simulation model.

(3) A novel numerical model, which includes both critical flux theory and CEOP phenomenon, was proposed to analyze the process of membrane colloidal

fouling. The animation of the colloidal fouling layer growth with time was depicted based on this simulation model.

(4) Simulations of concentration polarization and colloidal fouling in vibration enhanced RO membrane desalination system with experimental validation.

(5) A new CRO concept was proposed with the analysis of power consumption, operation cost and ROI study.

2. LITERATURE REVIEW

This chapter provides the basic principles of the RO membrane desalination, concentration polarization, colloidal fouling and fouling control methods in conventional RO membrane desalination system.

2.1. Fundamentals of RO Membrane Desalination

2.1.1. Membrane process and membrane module

Pressure driven membrane desalination refers to a process that a feed stream consisting of both solute and solvents is separated by a membrane module into a permeate stream and a concentrated stream. This separation characteristics are mainly determined by the corresponding pore size of the porous membrane structure. And they are classified as microfiltration (MF), ultrafiltration (UF), nanofiltration (NF) and reverse osmosis (RO). MF has the largest effective pore size (0.05 – 10 μm) and the lowest driven pressure which is less than 2 bar. It is the conventional coarse filtration and is typically used for water treatment, retaining suspensions and emulsions [6]. UF has finer pore size (1 – 100 nm) compared with MF and it has also higher driven force (less than 10 bar). UF is mainly used in dairy, food, metallurgy, textile, etc. RO has the finest effective pore size (less than 1 nm) with the highest operation pressure requirement. It needs 12-23 bar pressure for brackish water desalination, and 40-80 bar for seawater desalination. This extreme high pressure is needed to create enough transmembrane pressure to overcome the solution osmotic pressure and reverse the flow.

Osmosis is a natural phenomenon in which water (solvent) passes through a semi-permeable membrane from the side with lower solute concentration to the higher solute concentration side until equilibrium of water (solvent) chemical potential is reached [7].

There are four types of conventional RO membrane modules available:

1) Spiral wound module. RO membrane pieces form thin membrane channels and are wrapped in the spiral formation to increase the effective membrane area for a given membrane module volume. There are typically 5-10 membrane envelop channels in one commercial spiral wound RO module.
2) Plate and frame module. One thin membrane channel which includes one or both membrane walls.
3) Tubular module.
4) Hollow fiber module. Both tubular module and hollow fiber module are cylindrical membrane tubes with different diameters.

Table 1 summarizes the general characteristics of these four membrane modules [7]. Spiral wound module is the most commonly used membrane module since it has good packing density, acceptable tendency of fouling and tolerant feed stream filtration requirement. In the spiral wound module, the feed spacer is added in the feed channel to reduce the feed pressure drop and tendency of fouling.

Table 1. General characteristics of RO membrane modules.

Characteristics	Module type			
	Spiral wound	Hollow fiber	Tubular	Plate frame
Packing density (m^2/m^3)	800	6000	70	500
Feed flow rate (m/s)	0.25-0.50	0.005	1-5	0.25-0.50
Feed pressure drop (bar)	3-6	0.1-0.3	2-3	3-6
Feed stream filtration requirement	10-25 μm	5-10 μm	Not required	10-25 μm
Tendency of fouling	Average	High	Low	Average

2.1.2. Membrane performance

To describe the behavior of a membrane filtration system, permeate flux and intrinsic rejection coefficient of the membrane are commonly used.

The permeate flux is defined as the volume of permeate water collected per unit effective membrane area per second with the unit of m/s. And it can be evaluated using Darcy's law for porous media:

$$J = K(\Delta P - \Delta \pi) \tag{1}$$

where K is the membrane hydrodynamic permeability, ΔP is the applied trans-membrane pressure which equals the difference between the feed channel pressure and permeate pressure and $\Delta \pi$ is the osmotic pressure difference across the membrane.

Another form of the equation (1) is:

$$J = \frac{\Delta P - \Delta \pi}{\mu R_m} \tag{2}$$

where R_m is the resistance of membrane and μ is the fluid dynamics viscosity.

Both equations (1) and (2) are used for a clean membrane. For fouled membrane system, additional cake layer resistance term R_c needs to be added in the equation (2) and will be introduced in Chapter 4:

$$J = \frac{\Delta P - \Delta \pi}{\mu (R_m + R_c)} \tag{3}$$

Intrinsic rejection coefficient of the membrane $R_{i,rej}$ is used to describe the efficiency of membrane to separate water with other solutes with the range of 0 to 1 and is defined as

$$R_{i,rej} = 1 - \frac{c_{i,p}}{c_{i,m}} \tag{4}$$

where $c_{i,p}$ and $c_{i,m}$ are the permeate concentration and membrane local concentration of solute *i*. In this work, the $c_{i,p}$ are experimentally measured, and the $c_{i,m}$ are unknown and obtained via the CFD simulation. When the rejection coefficient = 0, both solute and solvent pass through the membrane freely; while the rejection coefficient = 1 means all solutes are completely blocked by membrane and this is the ideal situation in the membrane filtration process.

2.2. Membrane Concentration Polarization

Membrane concentration polarization is one of the most important factors which restricts the usage of membrane desalination. During the membrane desalination process, the solutes including ions and colloidal particles are rejected by the membrane while the permeate flux goes across the membrane. The solute concentration near the membrane surface increases and the accumulated solute will also cause a back-diffusion to transport solute from membrane surface to bulk. And this will eventually reach a steady-state condition where the convective solute accumulation caused by permeate flux equals to the back diffusion of the solute to the bulk flow. The build of the increased concentration boundary layer is well-known as the concentration polarization phenomenon in the membrane desalination process and is depicted in the Figure 1.

On the one hand, membrane concentration polarization will increase the corresponding solute osmotic pressure on the feed side, and thus reduce the membrane permeate flux; on the other hand, accumulated solute on the membrane surface will promote the membrane fouling. Inorganic salts, such as Ca^{2+}, CO_3^{2-} and SO_4^{2-}, may form insoluble salts and scaling while the accumulated concentration exceeds the corresponding solubility limit. In addition, accumulated silica colloidal particles on the membrane surface may transfer from liquid phase (concentration polarization) to the solid phase (porous cake) [8].

In order to have a better understanding of concentration polarization and eliminate the effect the concentration polarization, several different models were

proposed to describe it including film theory model, osmotic pressure model and boundary layer resistance model.

The film theory model assumes the mass transfer near the membrane surface is one dimensional convection-diffusion process and describes the permeate flux prediction as [9]:

$$J = \frac{D}{\delta_{BLT}} \ln \frac{\left(c_m - c_p\right)}{\left(c_b - c_p\right)} \tag{5}$$

where D is the solute diffusion coefficient, δ_{BLT} is the boundary layer thickness, c_m is the concentration at the membrane surface, c_p is the permeate flux concentration, and c_b is the bulk flow concentration.

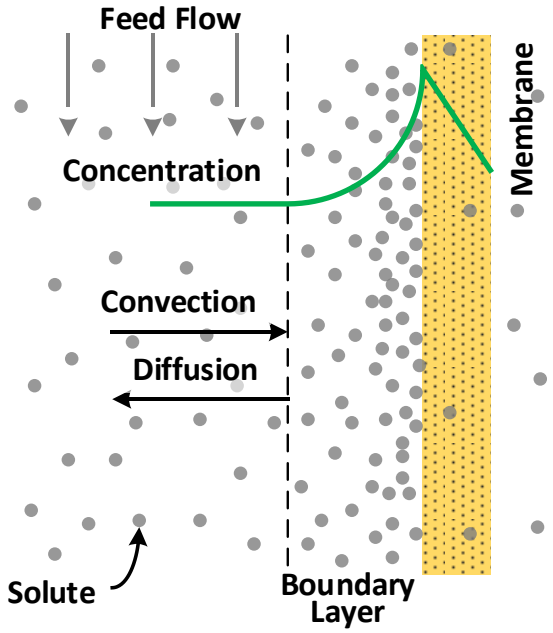

Figure 1. Membrane concentration polarization phenomenon.

The osmotic pressure model contributes the permeate flux decline caused by concentration polarization as the increase of osmotic pressure [6]. High concentration of molecules will cause high osmotic pressure and reduce the effective transmembrane pressure. The permeate flux is given by:

$$J = \frac{\Delta P - \Delta \pi}{\mu R_m} \tag{6}$$

The boundary layer resistance model treats membrane concentration polarization as an additional hydraulic resistance when considering the separation process [10]. By assuming all resistances act in series, we have:

$$J = \frac{\Delta P}{\mu (R_m + R_{cp})} \tag{7}$$

All these models are simple one-dimensional models assuming: a) permeate flux is constant throughout the boundary layer; b) solute convection-diffusion mass transport is only one dimensional; c) concentration polarization (CP) and permeate flux doesn't depends on the axial position and thus remain constant along the whole membrane channel [11]. All these assumptions are too coarse for the current industrial membrane desalination research. The combination of CFD simulation with traditional CP models overcomes all above mentioned limitations and provides detailed hydrodynamics information of the membrane desalination. As mentioned in the review by Ghidossi et al. [12], CFD is becoming more important in RO membrane science since it can provide

more detailed flow and solute distribution information, especially when combining CFD simulation with laboratory membrane module experiments.

Eric Lyster and Yoram Cohen [11] analyzed the concentration polarization in both rectangle reverse osmosis module and laboratory plate-and-frame RO membrane module by solving fully coupled fluid dynamics and mass transfer equations in COMSOL. Simulation results demonstrated the importance of considering local permeate flux variability among axial direction in order to predict local concentration variations, especially flow recirculation regions. Flow recirculation regions were responsible for the local concentration polarization consistent with available experimental results for membrane scale formation.

Lianfa Song and Shengwei Ma [13] investigated the impact of geometry of spacer filaments on concentration polarization and permeate flux in spiral wound reverse osmosis modules using the 2-D finite element model. The patterns of concentration polarization along the spacer-filled membrane channel were first investigated respectively for the membranes attached to and opposite to the transverse filaments.

Ana I. Cavaco Morão, Ana M. Brites Alves and Vítor Geraldes [14] studied the flow structure and solute concentration distribution in a nanofiltration / reverse osmosis plate-and-frame module with radial thin feed channels considering the entrance and outlet effects using CFD method. Flow instability was found in the entrance and outlet regions, however, those instabilities don’t affect significantly the average concentration polarization on the membrane surface up to Re = 570. Mass transfer correlations for a

plate-and-frame module with 3D flow structure and highly non-uniform concentration polarization was derived.

S. Wardeh and H.P. Morvan [15] developed a computational model with the help of ANSYS-CFX to study flow in the spacer-filled membrane channels. Simulation results, including the detailed flow patterns, pressure loss, and wall shear stresses, suggest that the zig-zag type of feed spacer is more economical and efficient compared with the submerged feed spacer from the aspect of reducing concentration polarization at the membrane surface.

Abhijit Chaudhuri and Anoop Jogdand [16] presented ANSYS FLUENT simulation results for a closed rotor-dynamic RO filtration system. Simulation results showed that the more fluid mixing and permeate flux, less concentration polarization will be found for higher angular speed of the rotor. System level energy analysis showed that energy required to rotate the disk is very small compared to the energy supplied for permeate flow for small Reynolds number flow.

Experiments with ladder-type, spacer-filled rectangular channels with a tracer injection flow visualization technique were performed by Geraldes et al. [17] to study the effects of spacer parameters on membrane performance. The flow visualization and friction factor measurements showed that critical Reynolds numbers increase with the decrease of the distance between spacers.

Fimbres-Weihs et al. [18] studied transient unsteady flows inside two dimensional spacer-filled channels using the CFD method. Unsteady flow patterns were observed inside the feed channels at Reynolds number of 841 and 1683. Vortices formed

and grew behind the feed spacer moving downstream with the bulk flow. The regions where the fluid flowed near the membrane wall contained both high mass transfer rate and high shear rate.

2.3. Membrane Colloidal Fouling

Membrane colloidal fouling is one main type of membrane fouling during the membrane desalination process. It refers the process that colloidal particles deposited on the membrane surface and formed a uniform porous cake layer to prevent permeate flux going through the membrane. Colloids are usually in the size range of 1 – 1000 nm and have a large surface area to volume ratio due to the small diameters [19].

In the RO crossflow desalination process, the colloidal particles are transported by both the bulk crossflow and permeate flux. Convection-diffusion equations are typically used to describe the colloidal particle transport in the membrane desalination process. The drag produced by the permeate flux is the main driven force of the particle accumulation and deposition on the membrane surface. And the back-diffusion will induce the particle near the membrane surface to move back to the bulk flow to reduce the particle accumulation. When building up the cake layer of particles, effective colloidal particle diffusion coefficient D_c is used to depict the process that crossflow induced colloidal particle backtransport into the bulk flow. When this backtransport force equals to the permeate flux induced drag force, temp-equilibrium was created. Several different mechanisms were pointed to be responsible for the particle backtransport phenomenon, including Brownian diffusion, shear-induced diffusion,

inertial-lift forces, etc [20]. Detailed discussion of the backtransport mechanism will be presented in Chapter 4.2..

Since the particle transportation is highly related with the permeate drag, the concept of critical flux was introduced to describe the limit of colloidal fouling. The critical flux is defined as a certain value of permeate flux below which a decline of flux with time does not occur; above it fouling is observed [21]. No obvious permeate flux reduction will be found when the membrane system permeate flux reaches its critical flux level. In other words, this system can be seen as a 'steady-state' system and this steady-state permeate flux can be treated as its critical flux.

The critical flux concept has been widely and successfully applied in microfiltration, reverse osmosis and membrane bioreactor [22–25] and was clarified both theoretically and from an experimental viewpoint. It was found that the value of critical flux is highly related with flow hydrodynamics [21] and particle transport properties such as particle size and local shear rate [26]. The net flux $(J - J_{crit})$ is used to identify whether colloidal particles will be deposited or not. The particle deposition rate is assumed to be proportional to the local net flux and local colloidal particle concentration [27].

Particles deposited on the membrane surface are expected to form a porous cake layer which introduces additional hydraulic resistance for permeate flux going through the membrane. This kind of resistance is well-known as the cake resistance and are developed and coupled with traditional osmotic pressure model mentioned in the membrane CP theory (Chapter 2.2.). As the result, equation (6) is rewritten as:

$$J = \frac{\Delta P - \Delta \pi}{\mu (R_m + R_c)} \tag{8}$$

where R_c is the hydraulic resistance caused by the porous cake layer itself and is pointed out to be highly dependent on the particle size [28,29].

Above mentioned hydraulic resistance is not the only effect of porous cake layer on membrane desalination. Porous cake will also make the membrane concentration polarization more serious and this phenomenon is so called cake enhanced osmotic pressure (CEOP) phenomenon which was first introduced by Hoek and Elimelech [30,31]. The solute back diffusion is hindered by the porous cake since the solute inside the cake layer needs to transport through the tortuous paths towards the bulk flow. [32]. Therefore, the CP phenomenon of salt solutes at the membrane surface is significantly increase which will greatly enhanced the corresponding osmotic pressure. According to the expression of permeate flux in equation (8), increased osmotic pressure will reduce the effective applied pressure, and thus reduce the permeate flux.

Both cake hydraulic resistance and CEOP phenomenon contribute to the permeate flux decline for membrane under colloidal fouling. Experiments performed by Hoek, Kim and Elimelech [31] showed that CEOP effect may be the main reason of permeate flux decline for silica particles with 100 nm ± 30 nm particle size, in which the cake hydraulic resistance is comparatively negligible.

Numerous simulations and experiments were performed to study the mechanism of the CEOP phenomenon. Kim and Chen [33] used the random walk simulation approach to study the diffusive tortuosity factor for solid and soft cake layers. Four

different structures were investigated including simple cubic, body-centered cubic, face-centered cubic, and random colloidal cake structures. They found that for volume fraction less than 0.5, influence of cake structure can be ignored. This conclusion was also confirmed by Neale and Nader [34].

Chong [35] used sodium chloride tracer response technique to investigate the CEOP phenomenon for two model foulants, colloidal silica and alginic acids, in unstirred fouling layers during RO desalination process. The results of constant permeate flux experiments confirmed that the colloidal fouling layers in RO could significantly reduce membrane apparent permeability, and this was predominantly through the CEOP effect rather than through an additional cake hydraulic resistance.

Systematic studies performed by Sim et al. [36] suggested that a lower crossflow velocity, higher permeate flux, higher salinity, and higher fouling concentration will cause more severe concentration polarization and a denser foulant layer. This will also induce an earlier occurrence of the colloidal metastability phenomenon. They also confirmed that a combination of TMP measurements and direct measurement of the foulant layer thickness via UTDR can be successfully used to study the colloidal fouling in RO systems.

Lee and Clark [37] presented a numerical scheme to solve the steady-state two-dimensional convection diffusion equation by assuming the solute concentration at the membrane surface cannot exceed a certain limiting value. They proved the effects of both molecular diffusion coefficient and shear-induced diffusion coefficient on membrane steady-state permeate flux. Their results also show that the steady-state

permeate flux increases with the axial velocity and decreases with the feed concentration. One limitation of their model is that they only considered the steady-state permeate flux for membrane desalination. In addition, the process of colloidal fouling growth and its effect on permeate flux is not discussed.

Chong and Fane [38] proposed a predictive mathematical model, which includes both critical flux theory and CEOP phenomenon, to account for the performance of colloidal fouling controlled reverse osmosis desalination system. Effect of different variables such as cake thickness, critical flux, particle size, feed solution concentration and operation conditions on membrane performance were investigated using this calculation model. However, it is only a one dimensional fouling model which doesn't includes the detailed fluid hydrodynamics calculation inside their model. And the cake thickness was assumed to be uniformed among the membrane.

Weihs and Wiley [39] developed a cake-layer mass transfer model which incorporates CFD simulation to investigate the 2D CEOP phenomenon. They compared the simulation results with existing experimental results to validate the effect of CEOP phenomenon. In their model, the cake layer does not form part of the fluid domain and thus does not affect the hydrodynamics of the channel feed flow. Inside the cake layer, one-dimensional solute diffusion and hydrodynamics were studied.

2.4. Fouling Control in Membrane Systems

In the previous section, we discussed about the mechanism of membrane fouling. Considering its effect on membrane performance and membrane lifetime, many efforts were devoted in the area of membrane system fouling control. There are three main categories of methods to control membrane fouling:

1) Pretreat the feed solution to reduce the absolute amount of foulant which enters the membrane desalination system [40].
2) Use anti-scalants or chemical cleaning [41].
3) Mechanically increase the shear rate and shear stress on the membrane surface [42].

Investigation [43] showed that the softening pretreatment can reduce the membrane scaling by removing a large fraction of Ca^{2+} ions in the feed solution. However, when considering the RO membrane colloidal fouling, the use of microfiltration (MF) or even ultrafiltration (UF) as a pretreatment step, may not completely remove colloidal particles with small size.

Chemical treatment such as the use of antiscalants has been studied to show the effect in mitigating silica fouling [44,45] and inorganic fouling [46]. However, it was also found that antiscalants may induce additional organic fouling in seawater desalination [47] and biofouling in groundwater treatment [48].

High shear rate at the membrane surface to reduce solute/particle deposition is known to be an effective way to reduce membrane fouling [49–52]. As mentioned in

Chapter 2.3, membrane system critical flux is highly related to the membrane local shear rate. By mechanically increasing the shear rate, the corresponding critical flux will also be increased. Since the critical flux is the sign of fouling occurs, membrane fouling will also be reduced when the critical flux is increased. Instead of traditional ways including increasing feed flow rate or reducing cross-section area, applications such as vibrating hollow fibers module (VHFM) [53], rotating disks systems [54] and vibratory shear enhanced processing (VSEP) [55] impose membrane vibration to increase the shear rate at the membrane surface.

Inorganic fouling control performance of mechanical vibration in the dead-end hollow fiber membrane desalination was examined by Li et al. [56]. Hollow fiber membranes with diameters of 1.7mm and 2mm were vibrated at moderate frequencies (0–15 Hz) and small amplitudes (0–12 mm). The experimental results showed that the hollow fiber membrane performance can be greatly improved when the vibration frequency or the vibration amplitude increases beyond a threshold magnitude.

Bilad et al. [57] proposed a novel magnetically induced membrane vibration system to study the effect of membrane vibration for membrane bioreactors. The results indicated significant improvement of critical flux, fouling rate and sustainability of operation in the vibrating system over conventional MBR processes.

The performance of a VSEP module was investigated in both microfiltration (MF) and ultrafiltration (UF) of UHT skim milk [58]. The permeate flux was found increasing with the membrane surface shear rate in both MF and UF with torsional

vibration frequency in the range of 56 Hz to 61 Hz. The better performance of the VSEP can be attributed to its higher membrane shear rate which reduces concentration at membrane and the mass transfer.

Experimental research investigated by Shi and Benjamin [59,60] indicated that inorganic fouling can be reduced by high shear rate at the RO membrane surface using the torsional vibration. They also found that an increase in vibration amplitude will decrease the membrane fouling and increase the rejection of most solutes. Instead of related with solely vibration frequency or vibration amplitude, membrane fouling rate is more sensitive to the membrane averaged shear rate. Another study performed by Shi and Befamin [61] also confirmed the membrane vibration will improve membrane natural organic matter (NOM) and heated aluminum oxide particle (HAOPs) rejections in both dead-end and crossflow modes.

3. CONCENTRATION POLARZATION PREDICTION FOR VIBRATION ENHANCED REVERSE OSMOSIS MEMBRANE SYSTEM WITHOUT FOULING[1]

The performance of a vibration enhanced reverse osmosis membrane module for desalination of artificial seawater was investigated with computational fluid dynamics (CFD) simulations and experiments. The computational model couples fluid dynamics with solutes transport inside the full length domain containing 'zigzag' spacers using a two dimensional, transient Large Eddy Simulation turbulence model. Both the local concentration dependent solute properties and variation of permeate flux over the membrane surface were predicted with the model. Membrane local permeate flux, concentration polarization, shear rate, and mass transfer were also calculated. The results suggest concentration polarization in the seawater desalination process could be reduced by imposing vibration on the reverse osmosis membrane. It was determined that the higher the vibration frequency the higher the membrane permeate flux while keeping the vibration amplitude constant. The CFD simulation predictions are validated against experimental data of permeate fluxes with good agreement.

[1] Parts of this section are reprinted with permission from Su, Xu, et al. "Concentration polarization and permeate flux variation in a vibration enhanced reverse osmosis membrane module." Desalination 433 (2018): 75-88, Copyright [2018] by Elsevier.

3.1. Introduction

High pressure seawater reverse osmosis (RO) is one of the most economic approaches for desalination. One challenge of RO membrane system is the concentration polarization phenomenon caused by the accumulation of rejected solutes and particles on the membrane surface. Concentration polarization will reduce permeate flux through the membrane and accelerate the membrane fouling, which limits the membrane lifetime [62]. Therefore, accurate predictions of the solute local concentration profile, and concentration polarization improvement are highly desired for improved design and operation of membrane desalination systems.

High shear rate at the membrane surface to reduce solute/particle deposition is known to be an effective way to reduce concentration polarization and increase the permeate flux in cross-flow membrane filtration [49–52]. Imposing motion of the membrane is one way to increase the shear rate at the membrane surface. Yeh and Cheng [63] used boundary layer theory to analyze membrane surface slip effect on the permeate flux in ultra-filtration. They found that the mass-transfer rate as well as permeate flux increase with the increase of the membrane slip velocity, which reduces the concentration polarization. A similar conclusion was also found by Chellam et. al [64] according to their 2D simulation of a channel bounded by one porous membrane wall boundary subject to uniform suction.

The vibratory shear enhanced filtration process (VSEP) [55] is a commercial unit that relies on rapid membrane motion to induce large shear rate. The VSEP system can

be treated as a disk-shaped desalination cell attached to a central shaft, utilizing high frequency torsional vibration of membrane to impose membrane motion. AI Akoum et al. [65] performed experiments to investigate the performance of VSEP module in yeast microfiltration (MF) and bovine albumin ultrafiltration (UF). They found that for both yeast MF and bovine albumin UF, the higher the membrane shear rate, the higher the permeate flux with torsional vibration frequency in the range of 56 Hz to 61 Hz. Experimental research investigated by Shi and Benjamin [59] indicated that inorganic fouling can be reduced by high shear rate at the membrane surface imposed by the torsional vibration of VSEP system. A study proposed by Shi and Benjamin [60] revealed that an increase in vibration amplitude will decrease the membrane fouling and increase the rejection of most solutes. Varying both vibration frequency and amplitude showed that membrane fouling rate was almost invariant as long as the averaged shear rate is the same. However, the vibration amplitude of points near the center of shaking will have less effective shaking amplitude for the torsional vibration utilized in the VSEP system. This may not fully utilize the vibration benefit on salt concentration polarization reduction and fouling mitigation.

In this study, a novel vibration enhanced desalination technique is proposed to address the RO membrane concentration polarization problem, with the aim of increasing membrane permeate flux and reducing membrane salt concentration. In this technique, a RO membrane desalination cell is driven by linear actuators to impose axial rapid membrane vibration and large membrane surface shear rates. Fifteen cases for different vibration and flow conditions were first performed in the vibration enhanced

reverse osmosis membrane desalination setup to experimentally study the effect of vibration on RO membranes for seawater desalination. Detailed hydrodynamics were then analyzed using transient CFD simulation consisting of the fully coupled fluid dynamics and solute transportation governing equations performed for the 2D spacer-filled, full length vibration membrane channel. Finally, the simulation results were validated by the corresponding experimental observations.

3.2. Experimental Work

3.2.1. Simulated seawater feed solution composition and membranes

Distilled water was used to prepare the artificial seawater feed solution. The composition of feed solution is listed in Table 2. All chemicals used in feed water preparation were reagent grade and purchased from Fisher Scientific.

The membrane used in all tests had 20 cm length × 3 cm width, yielding an effective membrane area of 60 cm^2. Specifications for the membrane are summarized in Table 3 [66].

Table 2. Feed water composition.

Chemical	*mol / L*
NaCl	0.4187
MgSO4	0.0503
CaCl2	0.0342
Na2SO4	0.0172

Reprinted with permission from [82]

Table 3. Specification of the membrane.

Membrane	SWC6 MAX
Vender	Hydranautics
Material	Composite Polyamide
Permeate Flow[a]	7.2 lpd
Salt Rejection	99.8 %
pH Range, Continuous	2 - 11
Max Cl_2 concentration	0.1 ppm
Max Temperature	318 K

[a]At 55 bar applied pressure

Reprinted with permission from [82]

3.2.2. Vibratory RO membrane test cell set up

Figure 2 shows the vibratory RO membrane cell module, which is employed for all experiments. This membrane cell module has two separate parts. The upper part contains the high pressure feed channel, a feed water inlet port and a retentate outlet port. The height of the feed channel is 0.78 mm and the feed spacer is placed inside the feed channel. The feed spacer used in experiments is cut from conventional RO membrane unit. Square rubber O-rings are used for sealing. The bottom part contains the permeate channel and two permeate outlet ports. The permeate carrier is placed inside the permeate channel which collects and transports permeate water to permeate ports.

The RO desalination cell is fixed on two shafts and supported by four linear bearings in Figure 3. A linear actuator (LinMot Inc., P01-48×360F/60×210) is controlled by a laptop-based program and is used to vibrate the cell at desired amplitude and frequency. For all vibration cases, vibration amplitude is fixed at 1.2 mm while vibration frequency varies from 20 Hz to 50 Hz.

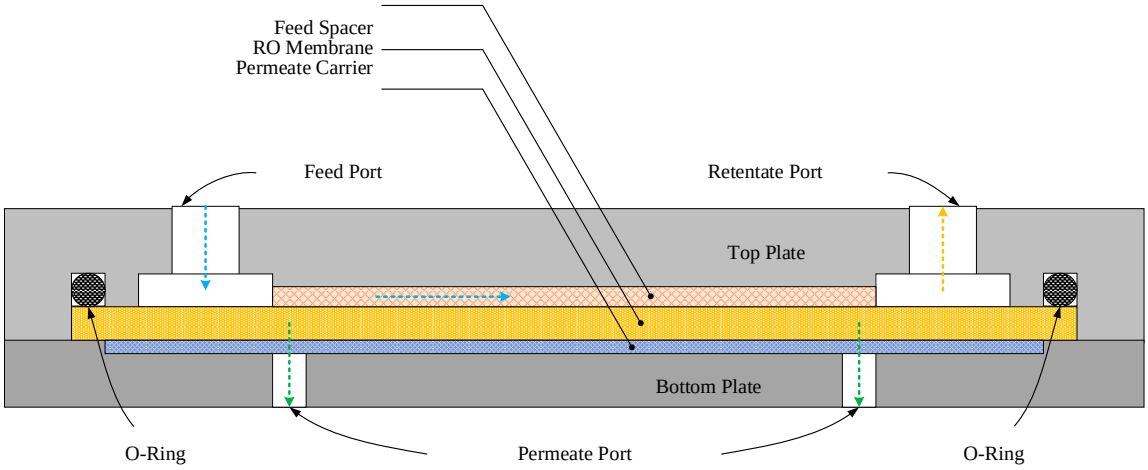

Figure 2. Vibratory RO membrane cell diagram. *Reprinted with permission from [82]*

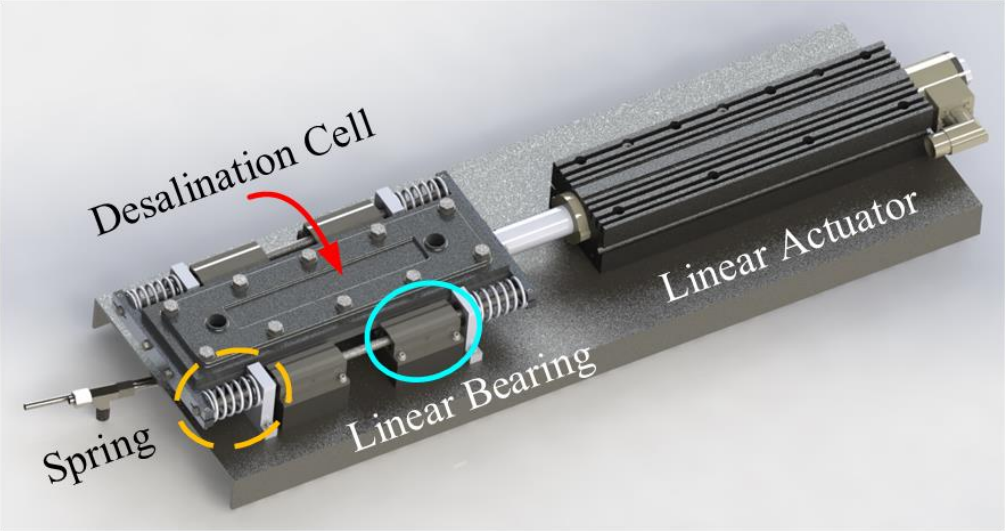

Figure 3. Solid model of test cell arrangement. *Reprinted with permission from [82]*

Figure 4 shows a hydraulic circuit diagram of the test installation. The stainless steel feed tank has a volume of 22.7 liters and serves as a supply for the stainless steel diaphragm pump (Hydra-Cell, M03BABTHFECA) which pressurizes the feed solution. The pulsation dampener (CAT, 6028) is used to absorb the feed flow pressure fluctuations. The inlet pressure and flow rate are measured by a digital pressure transducer (Omega, PX309-1KGV) and in-line flow meter just upstream of the desalination cell. The pressure relief valve and regulating valve are used to adjust the cell pressure and feed flow rate, respectively. The retentate flow goes through the regulating valve to reduce pressure to atmosphere and goes back to the feed tank. The permeate flow is collected and measured at the desalination cell side. Permeate flow is poured back to the feed tank after measuring in order to keep the feed water salinity

constant. The concentration of the feed water and permeate water was measured by a conductivity meter (Hana Instruments Inc., HI98192), which has an EC accuracy of 0.01 S/cm.

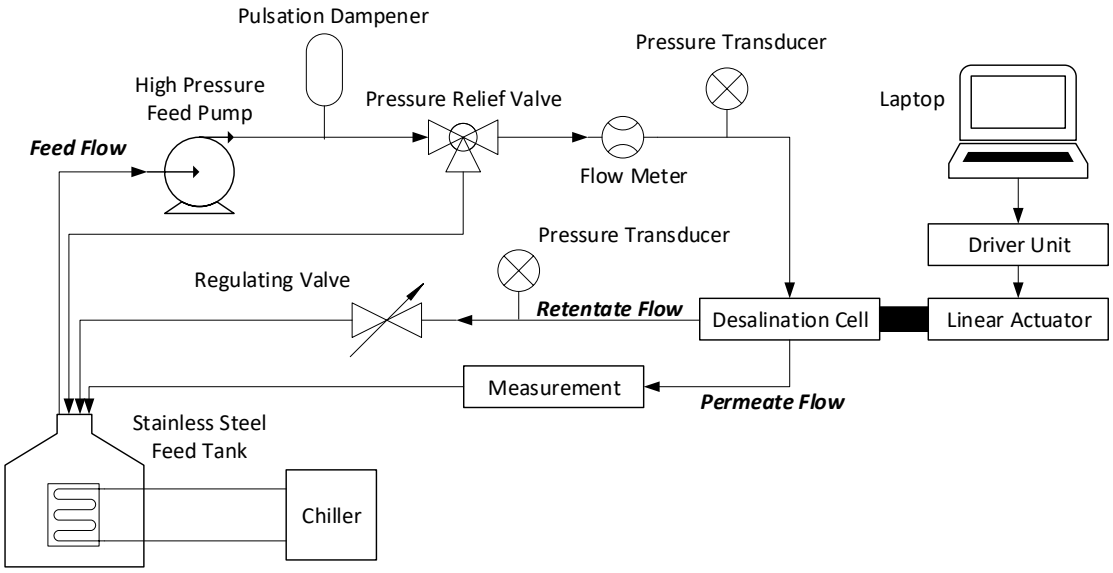

Figure 4. Experimental system diagram. *Reprinted with permission from [82]*

3.2.3. Experiment Procedure

A new membrane was used for each experiment and was first compacted using distilled water at an operating pressure of 55 bar for at least 4 hours until a stable baseline permeate flux was obtained.

Non-vibration membrane cases with three different inlet flow rate were performed in order to establish the benchmark data to compare with the vibration test cases. Vibration values, permeate flux, permeate salinity, feed pressure and feed water temperature were recorded during each vibration membrane test, while keeping the feed flow rate and feed pressure constant.

A feed pressure of 55 bar was employed for all tests and three different feed flow rates were utilized: 0.3785 lpm, 0.5678 lpm, and 0.7570 lpm. These feed flow rates produced three different inlet Reynolds numbers: Re = 344, 516 and 688, respectively. The feed solution temperature was kept in the temperature range of 25 ± 1 ^{o}C and measured by a J-type thermocouple with 0.1 ^{o}C accuracy.

3.3. Theory and CFD Numerical Simulations

3.3.1. Governing equations

The hydrodynamics of the transient two-dimensional flow inside a spacer-filled RO membrane channel is described by the following governing equations.

Continuity equation:

$$\frac{\partial \rho}{\partial t} + \frac{\partial (\rho u)}{\partial x} + \frac{\partial (\rho v)}{\partial y} = 0 \tag{9}$$

Momentum equations:

$$\frac{\partial(\rho u)}{\partial t}+\frac{\partial(\rho u^2)}{\partial x}+\frac{\partial(\rho uv)}{\partial y}=-\frac{\partial P}{\partial x}+\bigtriangledown\cdot(\mu\bigtriangledown u) \tag{10}$$

$$\frac{\partial(\rho v)}{\partial t}+\frac{\partial(\rho uv)}{\partial x}+\frac{\partial(\rho v^2)}{\partial y}=-\frac{\partial P}{\partial y}+\bigtriangledown\cdot(\mu\bigtriangledown v) \tag{11}$$

Solute transport of a non-reacting solution in the RO membrane channel is governed by the convection-diffusion equation:

$$\frac{\partial(\rho c_i)}{\partial t}+\frac{\partial}{\partial x}(\rho u c_i-D_i\frac{\partial c_i}{\partial x})+\frac{\partial}{\partial y}(\rho v c_i-D_i\frac{\partial c_i}{\partial y})=0 \tag{12}$$

where c_i and D_i are the concentration and diffusivity of solute i.

Please note that, although the flow velocity is below the Mach number, fluid density is not a constant. It depends on the local salt concentrations which is mentioned in Table 4. The density change is relatively small (less than 3%) and it is not sufficient to generate pressure waves. Pressure induced density change is neglected.

3.3.2. Geometry and mesh generation

A rectangular 2D membrane channel filled with 'zigzag' cylindrical spacers was adopted as the computational domain. The simulation domain is 200 mm in length and 0.78 mm in height, which has the same dimensions as the experimental setup described in Section 2.2. The left and right boundaries are the inlet and outlet for this channel. The top wall is impermeable wall while the bottom is a semi-permeable RO membrane.

Structured mesh generated using ICEM-CFD (Ansys, Inc., Canonsburg, PA) was adopted in this simulation to obtain accurate results with low computing time. Figure 6 depicts representative details of the mesh structure. The mesh near the membrane is much finer due to the expected large concentration gradient near its surface.

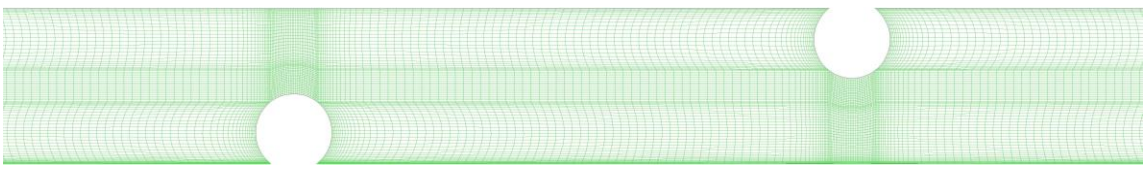

Figure 5. Representative mesh structure. *Reprinted with permission from [82]*

Each set of two successive spacers comprises one 'cell element' as shown in Figure 6. This pattern is repeated 35 times in the simulation domain. The entire computational domain consists of the 35 repeated 'cell elements' and a 0.5mm length exit area. Each 'cell element', has l_m = 2.85 mm and $r_s = \frac{1}{4}h$ = 0.195 mm. This 'zigzag' geometry is closely similar with the spacer-filled channel in the experiments.

Four simulations were conducted using 4.06×10^5, 6.80×10^5, 8.48×10^5 and 10.6×10^5 cells in order to eliminate the effect of mesh quality and size on the results. Figure 7 shows the steady membrane permeate flux profile in the middle of the 18th cell element which is far enough inward to avoid the influence of the inlet and outlet. A mesh with 6.80×10^5 cells has a good enough accuracy when predicting membrane permeate

flux. Hence, the computational grid was constructed using 6.80×10^5 cells. For this mesh size, the first cell height on the membrane boundary and spacer wall boundary are 0.8 μm and 3 μm, respectively.

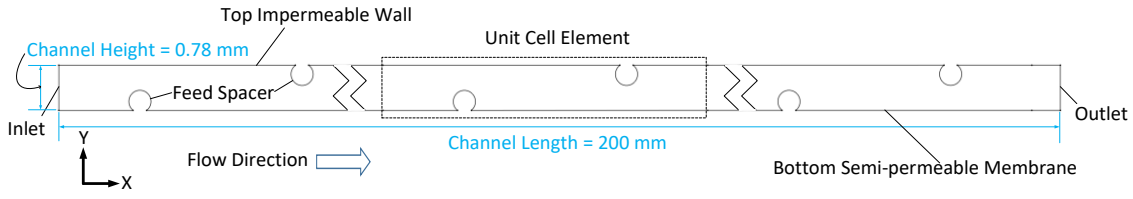

(A)

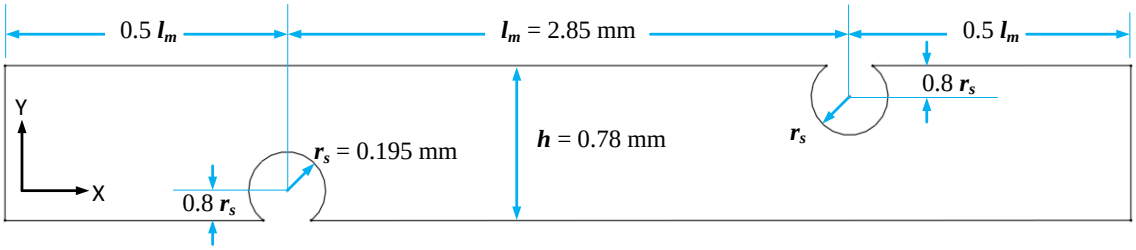

(B)

Figure 6. Model geometry. (A) The whole simulation domain. The dashed box shows one unit cell element. The unit cell element is repeated 35 times in the simulation domain. (B) One unit cell element. *Reprinted with permission from [82]*

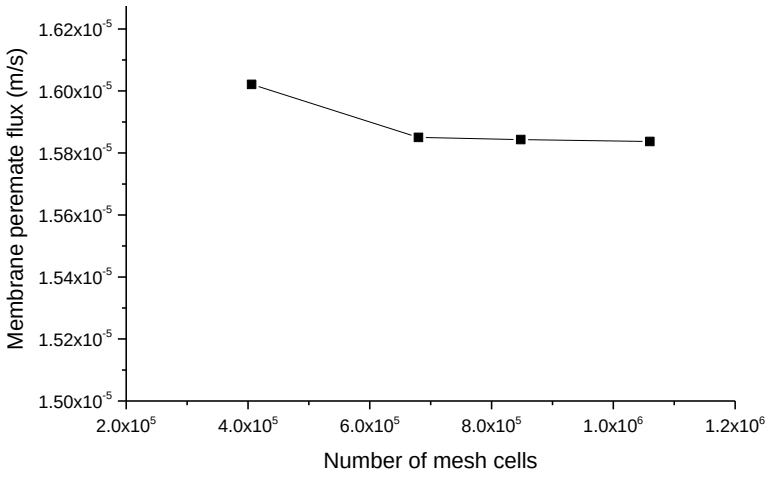

Figure 7. Membrane permeate flux profile using different mesh sizes. *Reprinted with permission from [82]*

3.3.3. Boundary conditions

The membrane local permeate flux is defined by Darcy's law for porous media:

$$J = K(\Delta P - \Sigma \Delta \pi_i) \tag{13}$$

where K is the membrane hydrodynamic permeability, ΔP is the applied trans-membrane pressure which equals the difference between the feed channel pressure and permeate pressure and $\Delta \pi_i$ is the osmotic pressure difference across the membrane for solute i.

In this case, K is assumed to be a constant for a given membrane system and can be calculated from pure water experiments. There is no solute inside the system in the pure water experiment. So for this case, the above equation becomes:

$$K = \frac{J}{\Delta P} \tag{14}$$

The constant K is obtained using Equation (14) and measuring J and ΔP with a flow meter and pressure gauge, respectively.

The following fully developed velocity profile and solutes concentrations are imposed at the inlet (x=0) as:

$$\begin{gathered} u = 6\bar{u}\frac{y}{h}(1-\frac{y}{h}) \\ v = 0 \\ c_i = c_{i,b} \end{gathered} \tag{15}$$

where $c_{i,b}$ is the inlet bulk concentration of solute i and $\bar{u}$ is the averaged feed inlet velocity which is set to match the corresponding experimental flow condition. The experiment's feed composition shown in Table 2 was also utilized in the simulation. Three given feed channel Reynolds numbers 344, 516 and 688, corresponding with the experimental inlet flow rates 0.3785 lpm, 0.5678 lpm, and 0.7570 lpm, are considered in the simulations.

The channel Reynolds number is defined as [67]:

$$Re_{ch} = \frac{\rho \bar{u} d_h}{\mu} \tag{16}$$

where d_h is the hydraulic diameter for the spacer-filled membrane channel:

$$d_h = \frac{4\Lambda}{2/h + (1-\Lambda)(2/r_s)} \tag{17}$$

where h is the channel height = 0.78 mm, r_s is the spacer radius = $\frac{1}{4}h$ = 0.195 mm, Λ is the voidage of the spacer-filled membrane channel:

$$\Lambda = \frac{V_{tot} - V_{sp}}{V_{tot}} \tag{18}$$

where V_{tot} and V_{sp} are the total channel volume (channel length × channel height for 2D simulations) and volume occupied by spacers (area of circular spacers cutplane for 2D simulations), respectively.

The pressure outlet boundary condition in the simulations is set equal to the measured outlet pressure of the membrane channel, and the velocity gradient and solute concentration gradient are assumed to be zero since the outlet boundary is far away from the membrane zone.

$$\frac{\partial v}{\partial x} = 0, \frac{\partial c_i}{\partial x} = 0 \tag{19}$$

The given vibration velocity and no solute flux boundary condition are imposed at the non-membrane wall:

$$u = 2\pi f A \sin(2\pi f t) \qquad v = 0 \tag{20}$$

$$\frac{\partial c_i}{\partial \vec{n}} = 0$$

where A and f are the vibration amplitude and frequency, and A is 1.2 mm, and f is 20 Hz, 30 Hz, 40 Hz and 50 Hz in the simulations. $\vec{n}$ is the unit normal vector at the wall boundary. In the FLUENT simulation, the velocity value calculated in equation (20) was added as the boundary velocity using UDF code to achieve the boundary vibration in the given manner.

The boundary conditions for x flow velocity equal to vibration velocity, diffusive and convective fluxes being equal, and salt solute concentration are imposed at the membrane wall as:

$$u = 2\pi f A \sin(2\pi f t)$$

$$\begin{aligned} v &= -J \\ D_i \frac{\partial c_i}{\partial y} &= -J c_i R_{i,rej} \end{aligned} \tag{21}$$

where J is the membrane local permeate flux determined via Equation (13), $R_{i,rej}$ is the intrinsic rejection coefficient of the membrane:

$$R_{i.rej} = 1 - \frac{c_{i,p}}{c_{i,m}} \tag{22}$$

where $c_{i,p}$ and $c_{i,m}$ are the permeate concentration and membrane local concentration of solute i. In this simulation, the $c_{i,p}$ are experimentally measured, and the $c_{i,m}$ are unknown and obtained via the CFD simulation.

3.3.4. Numerical simulation

Transient simulations were performed using the LES turbulence model in order to obtain an accurate prediction of the vibratory membrane performance in reducing concentration polarization. The LES model separates the turbulent flow field into a combination of the large, energy-containing part and sub-grid part using the Smagorinsky-Lilly subgrid-scale model [68]. The resolved part represents the large eddies which control the flow behavior and the turbulent transport. The subgrid part represents the small scales which are assumed to be isotropic [69].

The space filter which was used to separate large and small scales in the whole domain D has the filtering kernel G [70]:

$$\bar{u}_i(\vec{x},t) = \int_D G(\vec{x}-\vec{\xi},t)u(\vec{\xi},t)d(\vec{\xi}) \tag{23}$$

After applying the filtering operation, the filtered Navier-Stokes equations of motion become [71]:

$$\frac{\partial\bar{\rho}}{\partial t} + \frac{\partial(\bar{\rho}\tilde{u}_j)}{\partial x_j} = 0 \tag{24}$$

$$\frac{\partial(\bar{\rho}\tilde{u}_i)}{\partial t}+\frac{\partial}{\partial x_j}(\bar{\rho}\tilde{u}_i\tilde{u}_j+\bar{p}\delta_{ij}-\tilde{\sigma}_{ji})=-\frac{\partial\tau_{ji}}{\partial x_j} \tag{25}$$

where sub-grid stresses (SGS) τ_{ji} are defined as:

$$\tau_{ji}=\bar{\rho}(u_j u_i-\tilde{u}_j\tilde{u}_i) \tag{26}$$

Fluent (Ansys, Inc., Canonsburg, PA) was used here as the CFD based solver of the coupled continuity, momentum and solute transport equations via the SIMPLEC algorithm. A second order upwind scheme is applied to interpolate solute variables, and the momentum equations are spatially discretized with the bounded central differencing approach. Time is discretized using a 2nd order implicit method.

The concentration dependent model parameters such as viscosity, diffusivity, and osmotic pressure are shown in Table 4 [11,72–74]. In this table, c denotes solute concentration in $mol\ L^{-1}$ unit.

Table 4. Concentration dependent viscosity, diffusivity and osmotic pressure for single salt solutions.

Solute c (mol L^{-1})	Density ρ (kg m^{-3})	Viscosity μ ($\times 10^3$ Pa s)	Diffusivity D ($\times 10^9$ m^2 s^{-1})	Osmotic Pressure π (bar)
NaCl	995.7 + 38.54c	1.004 + 0.08c	1.45 for 0.1 < c < 1.5	47.93c
$CaCl_2$	995.7 + 89.72c for c < 0.6	1.004 + 0.2981c for c < 0.6	(1.176 + 107.5c)/(1 + 95.24c + $26.03c^2$) for c < 0.132; $1.134 - 0.3213c + 0.2319c^2 - 0.1553c^3$ for 0.132 < c < 0.6	$62.35c + 13.14c^2 + 8.993c^3$ for c < 0.6
Na_2SO_4	995.7 + 11.91c for c < 0.6	1.004 + 0.4094c for c < 0.6	(1.08 + 129.3c)/(1 + 124.5c + $40.92c^2$) for c < 0.108; $1.042 - 0.3225c + 0.1048c^2 - 0.07547c^3$ for 0.108 < c < 0.6	$56.29c - 28.37c^2 + 23.05c^3$ for c < 0.6
$MgSO_4$	995.7 + 11.88c for 0.05 < c < 0.5	1.004 + 0.06092c for 0.05 < c < 0.5	$0.7288 - 0.1929c + 0.1517c^2 - 0.9297c^3$ for 0.05 < c < 0.5	$33.08c - 178.9c^2 + 942.7c^3$ for 0.05 < c < 0.5

Reprinted with permission from [82]

The Refutas index method [75] was used to predict the blend viscosities of the mixture. In this method, the Refutas index of each component (VBI_i) and the Refutas index of the blend (VBI_β) are calculated using Equations (27) and (28). In Equation (20), ω_i is the mass fraction of component *i*.

$$VBI_i = 23.097 + 33.469 \log\log(\upsilon_i + 0.8) \tag{27}$$

$$VBI_\beta = \sum_1^n \omega_i VBI_i \tag{28}$$

Very small time steps are required to adequately resolve the unsteady flow inside the vibratory channels for turbulence simulation. A time step of 2.0×10^{-6} s was used for all non-vibration and vibration cases. This value is smaller than time steps used in previous simulations [15,18,76,77], and the chosen time step also yields a maximum Courant number of approximately 0.2 which is sufficiently small to perform LES simulation.

Simulations were judged to be converged once the absolute mass, momentum, and solute concentration residuals were smaller than 5×10^{-6}, 5×10^{-6} and 1×10^{-9}, respectively. Higher convergence requirements are needed for solutes concentration since it plays a pivotal role in calculating membrane concentration polarization and permeate flux variation along the membrane surface.

3.3.5. Post-processing

3.3.5.1. Concentration polarization modulus

The concentration polarization (CP) modulus of solute i is evaluated from the simulated solute concentration $c_{i,m}$ at the membrane surface as:

$$\Gamma_i(x) = \frac{c_{i,m}}{c_{i,b}} \tag{29}$$

3.3.5.2. Membrane surface shear rate

The membrane surface x direction shear rate is calculated from:

$$\dot{\gamma}(x) = \frac{\partial u}{\partial y}|_{y=0} \tag{30}$$

3.3.5.3. Membrane surface Sherwood number

The membrane surface Sherwood number for solute i is determined from:

$$Sh_i(x) = \frac{k_m(x) d_h}{D_i} \tag{31}$$

where $k_m(x)$ is the membrane local mass transfer coefficient at position x and is calculated as

$$k_m(x) = \frac{D_i \frac{\partial c_i}{\partial y}|_{y=0}}{c_{i,b} - c_{i,m}} \tag{32}$$

In Equation (32), $c_{i,b}$ and $c_{i,m}$ are the bulk flow concentration and adjacent membrane concentration of solute i, respectively. The parameter d_h is the hydraulic diameter for a spacer-filled membrane channel which is defined in Equation (17).

3.4. Results and Discussion

Table 5 shows the model parameters used in CFD simulations, including twelve different vibration cases and three non-vibration cases. The CFD computations were performed for one vibration period in all vibration cases since the vibration period T is much larger than the vortex shedding time and the vibration has a higher influence on the membrane desalination. Non-vibration cases were also studied for 0.02 s as the control group.

Table 5. Summary of CFD simulation conditions.

Run No.	Re	Vibration Frequency (Hz)	Vibration Amplitude (mm)	Pressure (bar)
1	344	0	NA	55
2	344	20	1.2	55
3	344	30	1.2	55
4	344	40	1.2	55
5	344	50	1.2	55
6	516	0	NA	55
7	516	20	1.2	55
8	516	30	1.2	55
9	516	40	1.2	55
10	516	50	1.2	55
11	688	0	NA	55
12	688	20	1.2	55
13	688	30	1.2	55
14	688	40	1.2	55
15	688	50	1.2	55

Reprinted with permission from [82]

3.4.1. Membrane local concentration polarization profile

NaCl is the dominant solute in the feed solution responsible for most part of the salt osmotic pressure. A lower membrane *NaCl* CP modulus means that a lower operation pressure is needed to get the same permeate production for a given membrane system and feed solution. This will reduce the energy cost significantly in the real RO membrane seawater desalination system. Additionally, $CaSO_4$ is a barely soluble mineral salt in the feed solution, which leads to mineral salt scaling on the membrane surface. Therefore, both *NaCl* and $CaSO_4$ membrane concentration polarization profiles were predicted and are shown in this section. Since the solubility of $CaSO_4$ in water is lower than other possible calcium compounds such as $CaCl_2$, gypsum crystals are more eager to appear at the membrane surface compared with $CaCl_2$ crystals for the given solution and desalination operation used in experiments. the authors use the concentration value of Ca^{2+} as the amount of potential $CaSO_4$ dissolved in the solution and use this value to check the possibility of the gypsum formation.

Figure 8 depicts membrane local *NaCl* concentration polarization modulus variation at the membrane surface with time for fifteen different flow and vibration cases. For three non-vibration cases (black lines), the higher the Reynolds number was, the lower *NaCl* CP modulus was. Increased inlet Reynolds number mitigates the salt accumulation near the membrane for the non-vibration cases. More salt will be transported back into the bulk flow thus avoiding the membrane surface accumulation at the high Reynolds number condition.

Similar with the non-vibration cases, increasing the inlet Re numbers will also reduce the *NaCl* CP modulus for vibration cases while keeping the vibration frequency the same (the same line color). Consideration of the effects of vibration, all vibration cases have lower *NaCl* CP modulus than the corresponding non-vibration cases for all three Re numbers.

From Equations (20) and (21), the membrane wall moves with acceleration:

$$a = (2\pi f)^2 A\cos(2\pi ft) \tag{33}$$

As shown in Equation (33), the vibration acceleration at the membrane boundary forms a cosine curve for all vibration frequencies. The vibration acceleration equals to zero when T = 0.25 and 0.75. The local NaCl CP modulus reaches local maximum at these times. Similarly, vibration acceleration reaches its peak value when T = 0, 0.5 and 1, and the local *NaCl* CP modulus reaches a local minimum at these times. The wave form of *NaCl* CP curves for all vibration cases are similar with sine wave, especially for low Re case. These results strongly indicates that the *NaCl* CP is highly dominated by membrane vibration, especially for low Re case. For the high Re cases, due to the complexity of the fluid flow itself, *NaCl* CP is not strongly affected by membrane vibration compared with low Re cases.

Cases with the higher vibration frequencies have lower *NaCl* CP modulus when keeping the Reynolds number the same (the same line symbol). Increasing the vibration frequency, while keeping the vibration amplitude constant, causes an increase in the overall shear rate at the membrane surface.

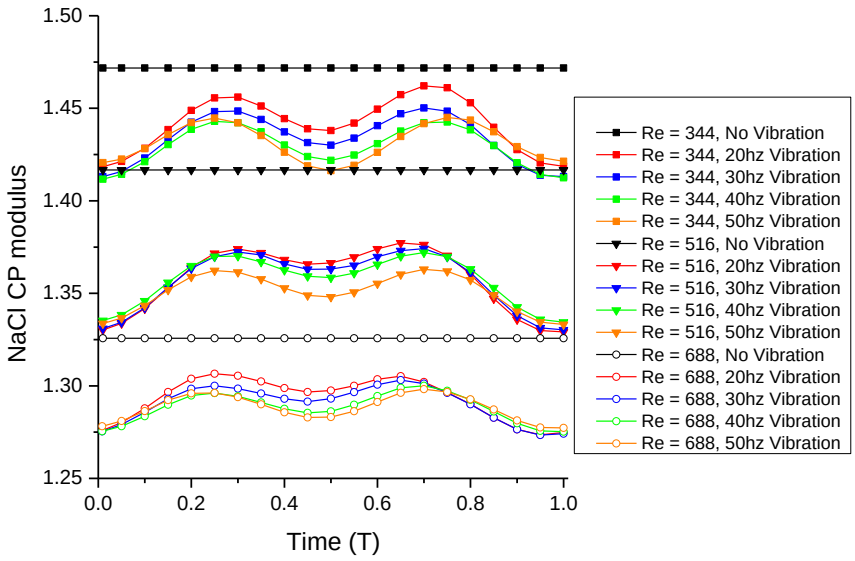

Figure 8. Membrane *NaCl* concentration polarization modulus variation with time. *Reprinted with permission from [82]*

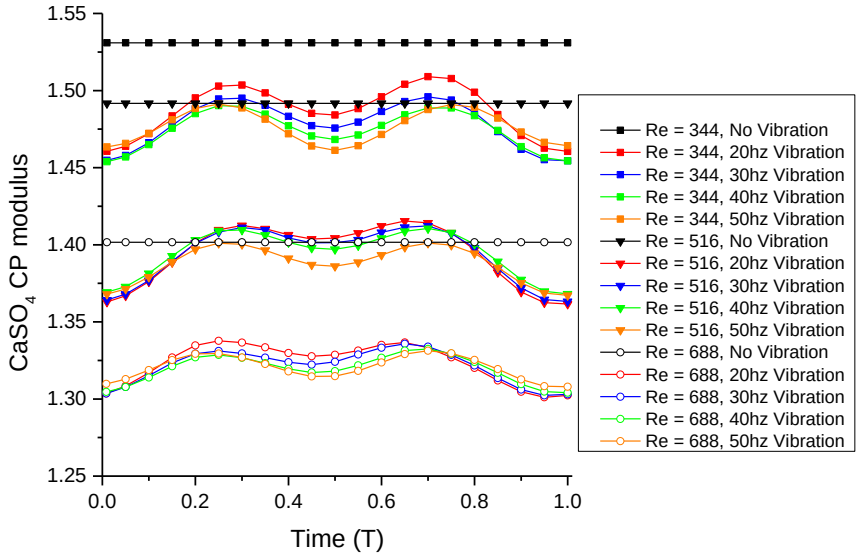

Figure 9. Membrane *$CaSO_4$* concentration polarization modulus variation with time. *Reprinted with permission from [82]*

Figure 9 shows the membrane surface $CaSO_4$ concentration polarization modulus variation with time for different flow and vibration conditions. Similar with the *NaCl* CP profile, higher inlet Reynolds number and higher vibration frequency will result in lower $CaSO_4$ CP modulus.

Figure 10 shows the time averaged *NaCl* and $CaSO_4$ concentration polarization modulus at the membrane surface for cases with different vibration frequencies. Similar to the conclusions based on Figure 8, under the same vibration conditions, cases with higher Reynolds numbers have lower membrane surface salt CP modulus, and with the same inlet Reynolds number, a higher frequency induces a lower salt CP modulus. By comparing *NaCl* and $CaSO_4$ values, it is found that under the same flow and vibration conditions, the $CaSO_4$ CP modulus is slightly higher than *NaCl* CP modulus. This shows that the $CaSO_4$ accumulation is more severe than *NaCl*. Thus $CaSO_4$ is more difficult for the bulk flow to carry out from the membrane surface area.

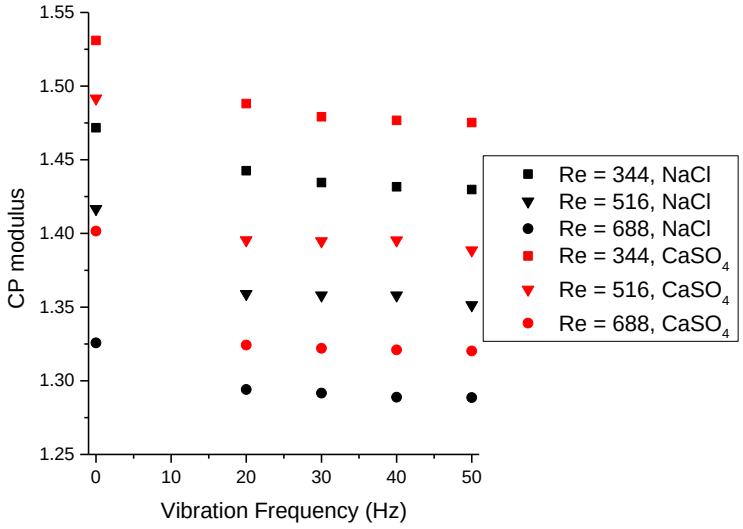

Figure 10. Time averaged membrane *NaCl* and *CaSO₄* concentration polarization modulus. *Reprinted with permission from [82]*

Figure 11 shows the *CaSO₄* CP modulus distribution in the middle filament at different times for the Re = 344, 50 Hz vibration case (top) and Re = 344, non-vibration case (bottom). The middle (the 18th) cell element was chosen as the example cell element to visualize detailed flow characteristic, salt solute concentration, and membrane local permeate flux since it is far enough to avoid the influence of the inlet and outlet conditions. From these figures, there is no obvious change of the *CaSO₄* CP modulus distribution inside the non-vibration case (bottom figures) and the corresponding maximum *CaSO₄* CP modulus is 3.8. For the Re = 344, 50 Hz vibration case (top figures), obvious transient patterns were observed. Salt accumulated on the membrane

surface near the spacer was transported back to the bulk flow. The maximum $CaSO_4$ CP modulus is 2.5 which is much lower than 3.8 in non-vibration case.

Previous investigations [78–80] show that reducing the local $CaSO_4$ CP modulus will reduce the rate of gypsum precipitation and membrane fouling since the new nuclei nucleation rate and crystal growth rate are related to local $CaSO_4$ concentration and degree of saturation. Our simulation shows that membrane vibration reduces $CaSO_4$ concentration at the membrane surface, especially at the membrane-spacer connection area. This $CaSO_4$ concentration reduction will also reduce the gypsum precipitation and membrane fouling potential.

3.4.2. Shear rate and detailed flow behavior

Figure 12 shows the membrane surface shear rate variation with time when Re = 344. As expected there is almost no variation in shear rate for the non-vibration case. The figure also shows that the boundary-peak shear rate significantly increases with vibration frequency.

(a) t = 5 ms

(b) t = 10 ms

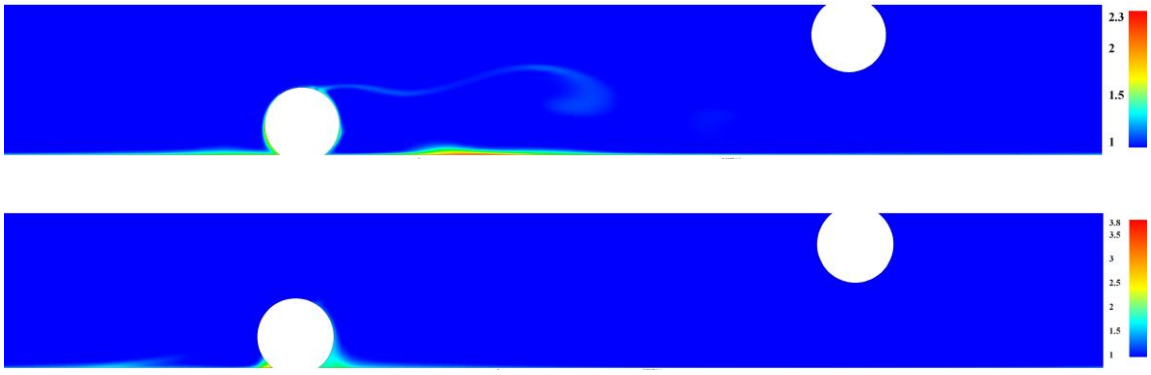

(c) t = 13.8 ms

Figure 11. *$CaSO_4$* CP modulus distribution in the middle filament when (a) t = 5ms, (b) t = 10 ms and (c) t =13.8 ms for 50 Hz vibration (top) and non-vibration case (bottom). *Reprinted with permission from [82]*

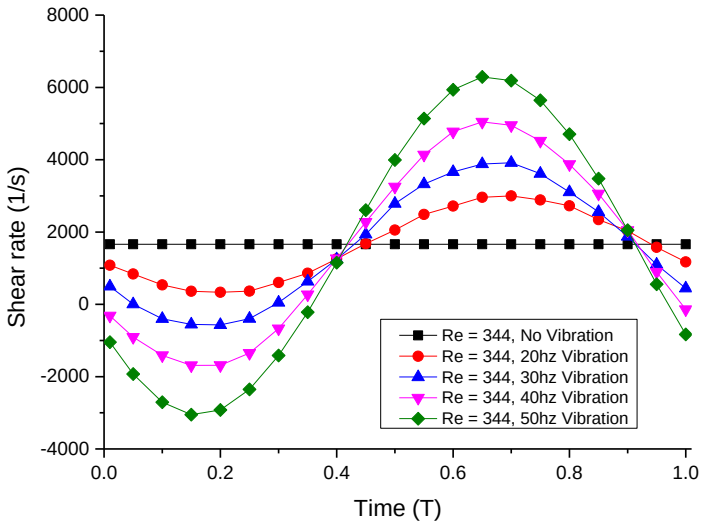

Figure 12. Membrane boundary shear rate variation with time for Re = 344 cases. *Reprinted with permission from [82]*

The root mean square (RMS) value of membrane shear rate was adopted in order to show the effect of vibration on membrane shear rate. The expression for RMS value of the membrane shear rate in one vibration period is shown in Equation (34). Figure 13 shows the RMS of membrane boundary shear rate value vs. vibration frequency. It is clear that boundary shear rate is greatly increased by vibration especially for the Re = 344 case. The shear rate increase induced by membrane vibration for Re = 688 is significant but relatively smaller than in the low Re case. This is due to the complexity of the flow condition near the feed spacers with Re = 688.

$$\gamma_{rms} = \sqrt{\frac{1}{T_{per}} \int_0^T \left| \gamma(t) \right|^2 dt} \tag{34}$$

Velocity vectors near the downstream face and the upstream face of the membrane spacer are visualized in this section. The physical significance of this is that the fluid behavior in the feed channel especially near the spacers plays a very important role in the salt accumulation and diffusion near the membrane. The Re = 344 and 50 Hz vibration were chosen for the example to show the difference between non-vibration and vibration cases.

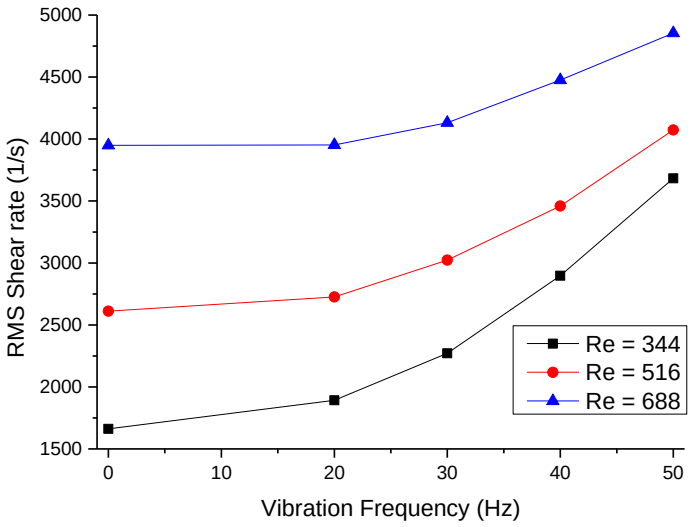

Figure 13. RMS of membrane boundary shear rate vs. vibration frequency. *Reprinted with permission from [82]*

Figure 14 shows the velocity vector profile in the middle filament over 20 ms for the Re = 344, 50 Hz vibration case (top) and Re = 344, non-vibration case (bottom). Similar with previous investigations [18,81], it is useful to label vortices near the bottom spacer area to track their generation, growth, movement and decay over time.

A small recirculation region was formed near the spacer upstream face while a larger recirculation region was located at the spacer downstream area in both non-vibration and vibration cases. Vortices formed in both regions and moved downstream with the bulk flow, and vortex shedding is found in the spacer downstream area. In all subfigures of Figure 14, two or three successive big vortices can always be found in the downstream area of the spacer, whether the membrane vibrate or not. They tend to move with the bulk flow and slightly towards the membrane. These successive vortices will be called 'dominant downstream' vortices for simplicity in the following discussion.

The membrane boundary velocity is positive during the first half cycle of shaking, t = 0 ms - 10 ms, for the 50 Hz vibration case. Near the start of the calculation, when t = 0.8 ms (Figure 14(a)), three 'dominant downstream' vortices are marked as vortex 1 - 3. There are no vortices in the upstream side of the spacer, which describes the non-vibration case and the vibration case.

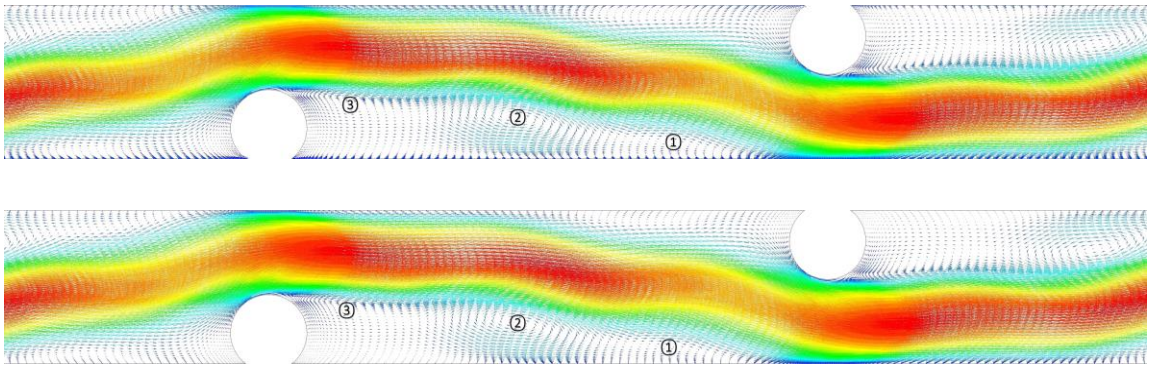

(a) t = 0.8 ms

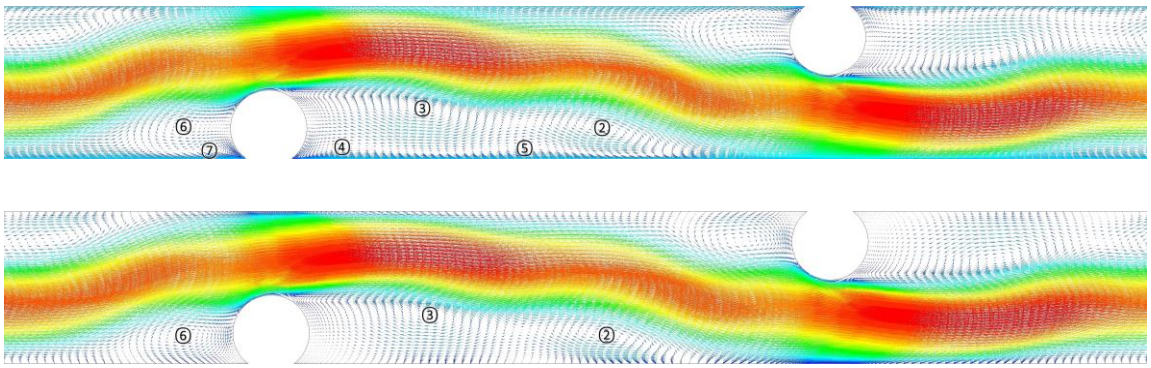

(b) t = 3 ms

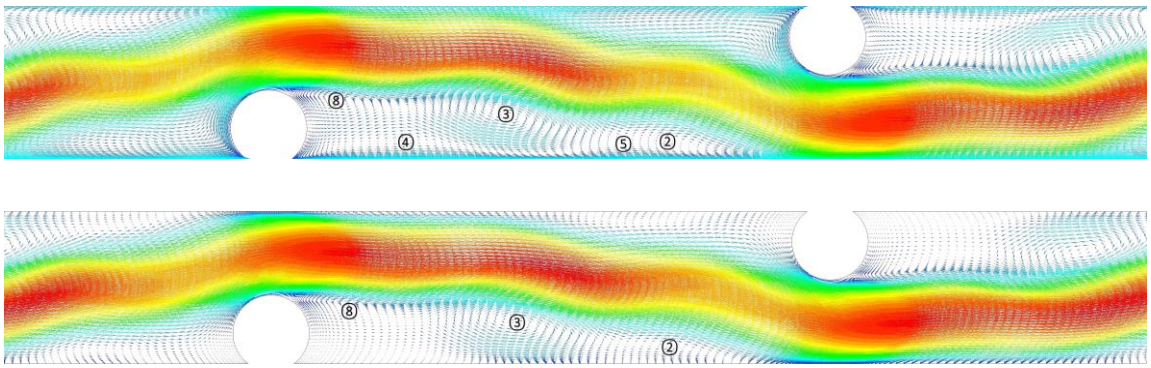

(c) t = 5 ms

Figure 14. Velocity vector profile in the middle filament during one vibration time period (20ms) for 50 Hz vibration (top) and non-vibration case (bottom). Shed vortices are identified by numbers 1-15. *Reprinted with permission from [82]*

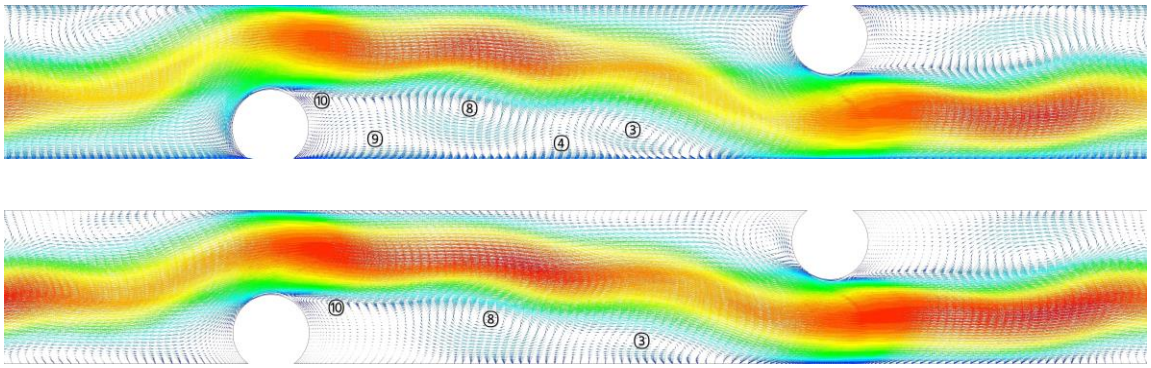

(d) t = 8.4 ms

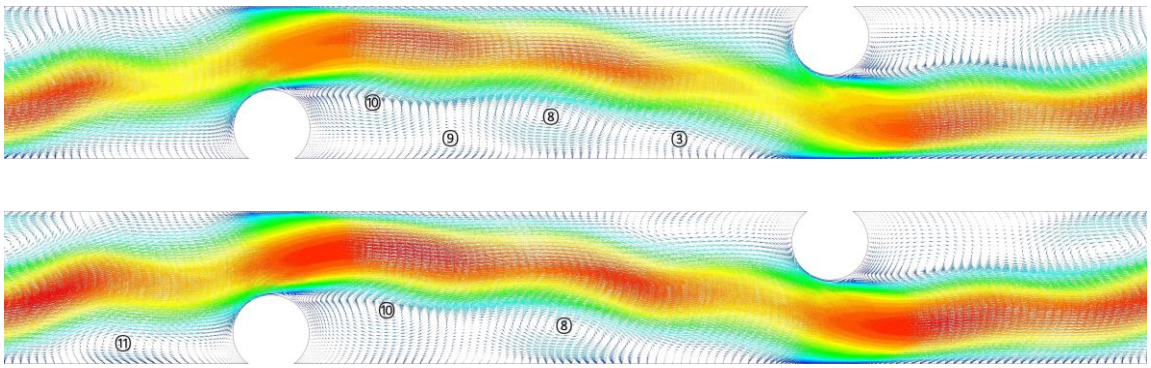

(e) t = 10 ms

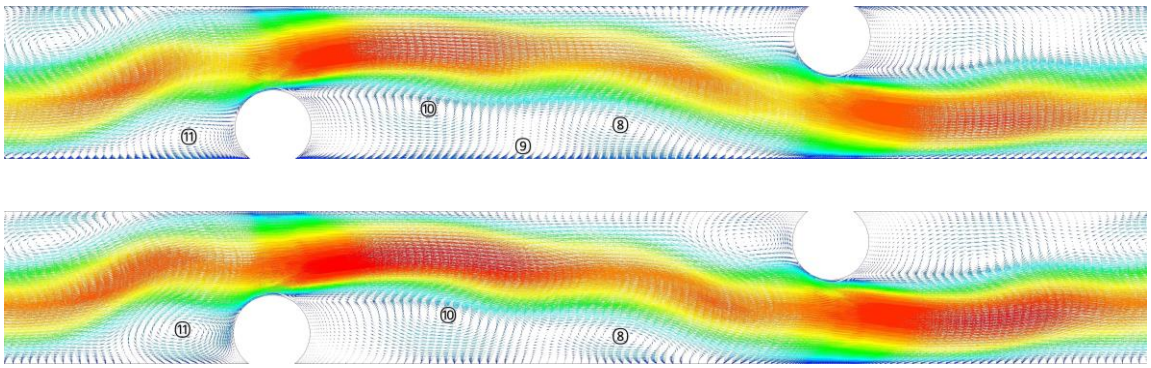

(f) t = 11.4 ms

Figure 14. Continued.

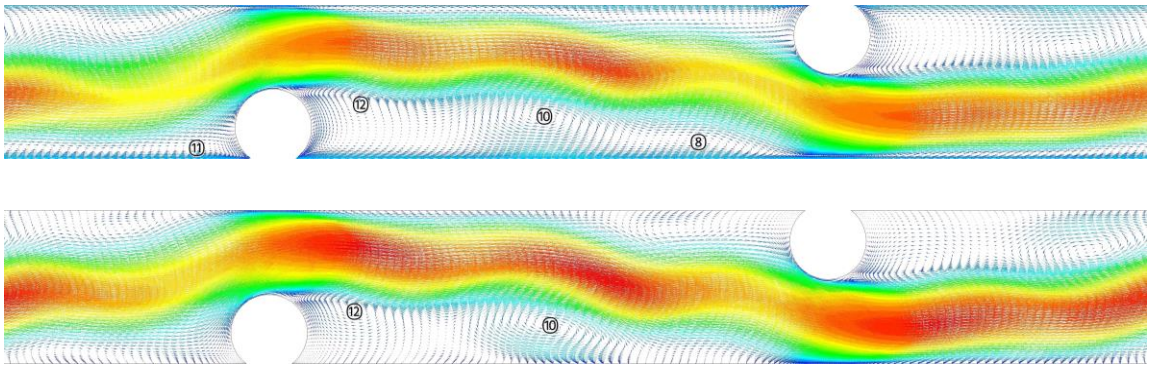

(g) t =13.8 ms

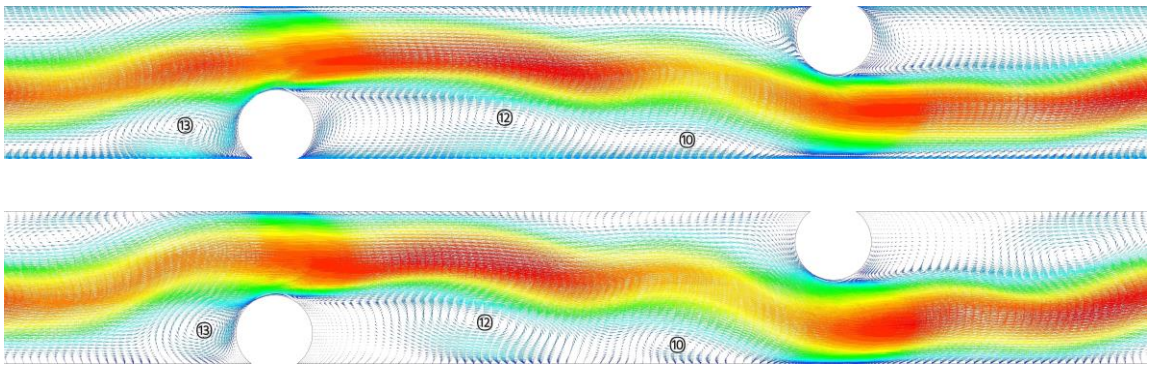

(h) t = 17.2 ms

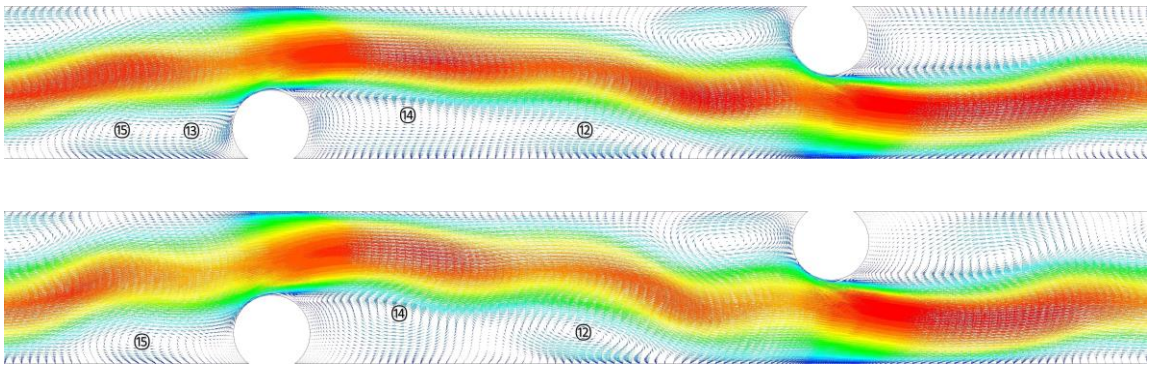

(i) t = 20 ms

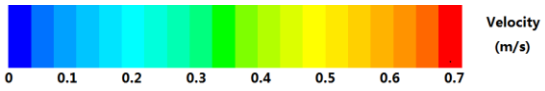

Figure 14. Continued.

When t = 3 ms (Figure 14(b)), it is interesting to note that there are two vortices 4 and 5 formed between the membrane and the two 'dominant downstream' vortices for the vibration case. This is mainly due the interaction between positive x-velocity at the membrane surface and negative x-velocity in the bottom of the 'dominant downstream' vortices. Two parallel vortices 6 and 7 are created at the upstream side of the membrane spacer, and have the opposite rotation direction. These two vortices will enhance the membrane local salt mass transfer and reduce the concentration polarization. Low membrane local velocity will reduce the salt mass transportation process. There are no vortices 4 and 5 formed near the membrane for non-vibration case. Another difference is that there is only one vortex 6 formed at the upstream face for the non-vibration case compared with two vortices in the vibration case. In the vibration case, the different velocity direction between the bottom of vortex 6 and membrane boundary induces vortex 7, increases flow complexity and enhances local mass transport. Similar with Figure 14(b), in Figure 14(c) and Figure 14(d), more vortices appear near the membrane in the vibration case compared with the corresponding non-vibration case. The membrane boundary velocity equals to 0 when t = 10 ms (Figure 14(e)), which is the same as the non-vibration case.

From Figure 14(e) to Figure 14(i), the difference in the number of vortices between the vibration case and the non-vibration case is not that obvious as in the time period: 0 ms - 10 ms. The reason is that during t = 10 ms - 20 ms, the membrane boundary velocity will become negative which is the same direction as the x-velocity of the fluid in the bottom of the 'dominant downstream' vortices.

Summarizing key observations: (a) flow in both the vibration and non-vibration cases follow the ‘zigzag’ pattern formed by the spacer geometry, (b) significant unsteady flow behavior occurs for the non-vibration and vibration cases, (c) imposed boundary vibration spawns vortex generation and decay at the membrane surface and also increases the boundary shear rate, and (d) as a result of imposed boundary vibration salt mass transfer is enhanced, salt CP modulus is reduced and membrane permeate flux is increased.

3.4.3. Membrane local mass transfer and Sherwood number

The Sherwood number is widely used when evaluating membrane performance since it eliminates the effect of inlet conditions and channel length. By calculating the Sherwood number, we can evaluate the salt mass transfer especially near the membrane surface for different inlet Reynolds numbers and different vibration frequencies.

Figure 15 depicts membrane surface *NaCl* Sherwood number profile variation with time for different flow and vibration conditions. The *NaCl* Sherwood number is seen to increase with Reynolds number by considering the three non-vibration cases (black lines). Increased inlet Reynolds number will increase the membrane local salt mass transport rate to the bulk flow. All vibration cases show better Sherwood number profile compared with corresponding non-vibration case. A second trend is that the higher vibration frequency, the higher the *NaCl* Sherwood number.

Figure 16 shows membrane surface $CaSO_4$ Sherwood number profile variation with time for different flow and vibration conditions. Figure 17 shows the time averaged membrane *NaCl* and $CaSO_4$ Sherwood number profile vs. vibration frequency.

Time averaged *NaCl* Sherwood number is increased by vibration for all Re numbers. The maximum Sherwood number increment is around 13% for the 50 Hz vibration cases. $CaSO_4$ Sherwood number profile shows similar trends with *NaCl* Sherwood number profile. By comparing time averaged *NaCl* and $CaSO_4$ Sherwood number profile, it is found that under the same flow and vibration conditions, $CaSO_4$ Sherwood number is slightly higher than *NaCl* Sherwood number. For the concentration appearing in this simulation set, the diffusivity of $CaSO_4$ is much lower than *NaCl* as shown in Table 4. Since the Sherwood number is the ratio of convective mass transfer rate and diffusive mass transport rate shown in equation (31), even with a higher Sherwood number, the $CaSO_4$ solution convective mass transfer rate $k_m(CaSO_4)$ is still lower than *NaCl* which means $CaSO_4$ is easier to accumulate at the membrane surface. This also explains the phenomenon found in the concentration polarization section, namely that the CP modulus of $CaSO_4$ is higher than *NaCl*.

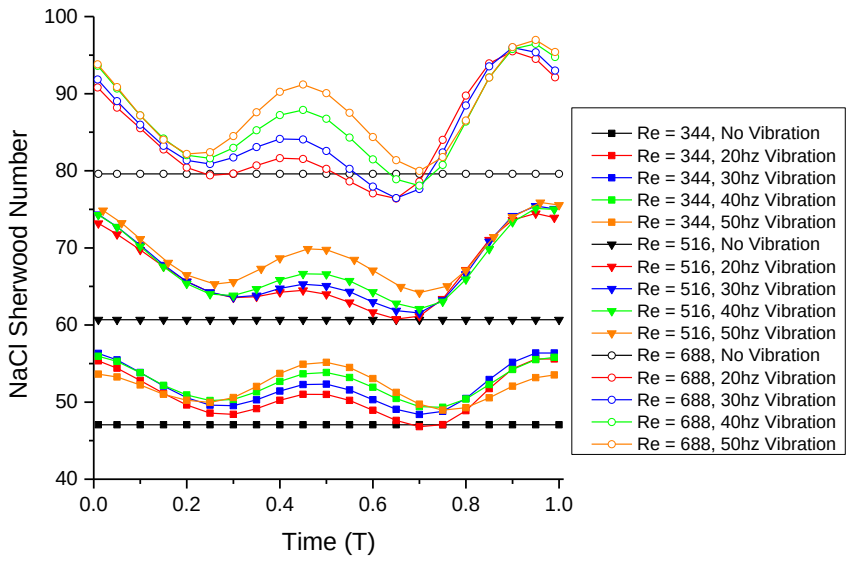

Figure 15. Membrane *NaCl* Sherwood number variation with time. *Reprinted with permission from [82]*

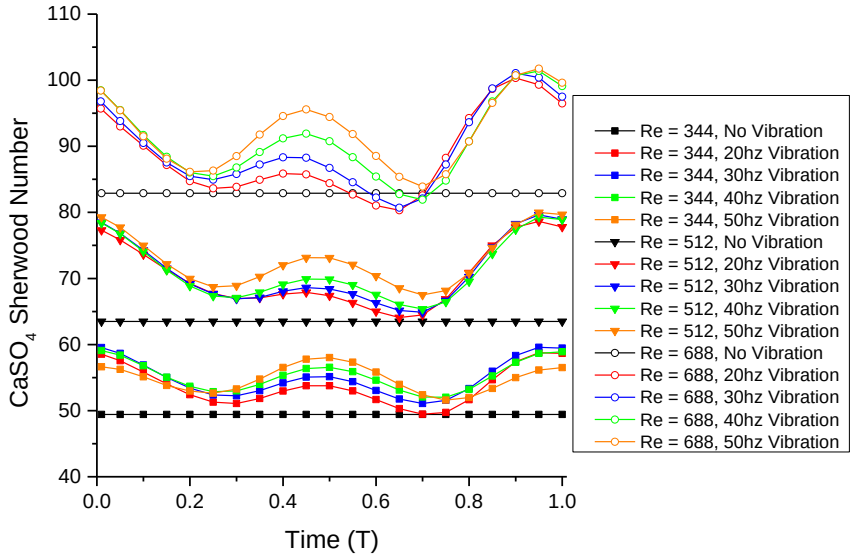

Figure 16. Membrane *CaSO₄* Sherwood number variation with time. *Reprinted with permission from [82]*

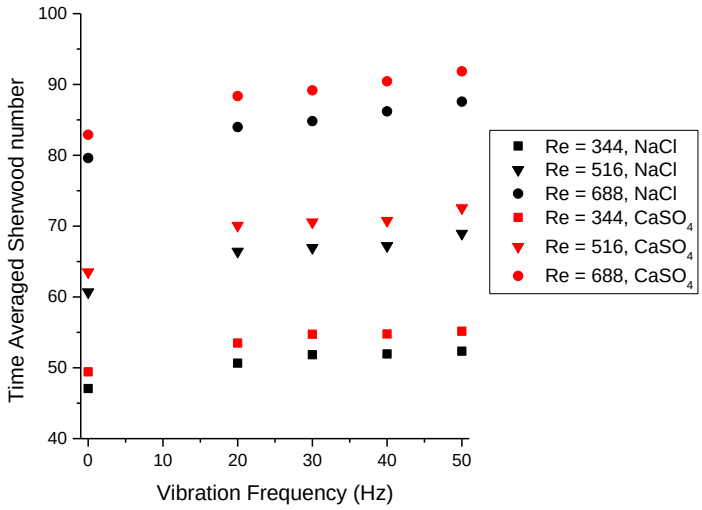

Figure 17. Time averaged membrane *NaCl* and *$CaSO_4$* Sherwood number vs. vibration frequency. *Reprinted with permission from [82]*

3.4.4. Membrane local permeate flux profile

Figure 18 shows normalized permeate flux variation with time for different flow and vibration conditions. Permeate fluxes for all cases were compared with the Re = 344, no vibration case to get the normalized permeate flux for better understanding of the effect of both Re numbers and vibrations. Equation (13) and Table 4 show that the higher the membrane local salt concentration, the lower the membrane permeate flux.

Consistent with the CP modulus profile shown in Figure 10, the time averaged permeate flux for vibration cases are higher than for the non-vibration cases over all Re numbers.

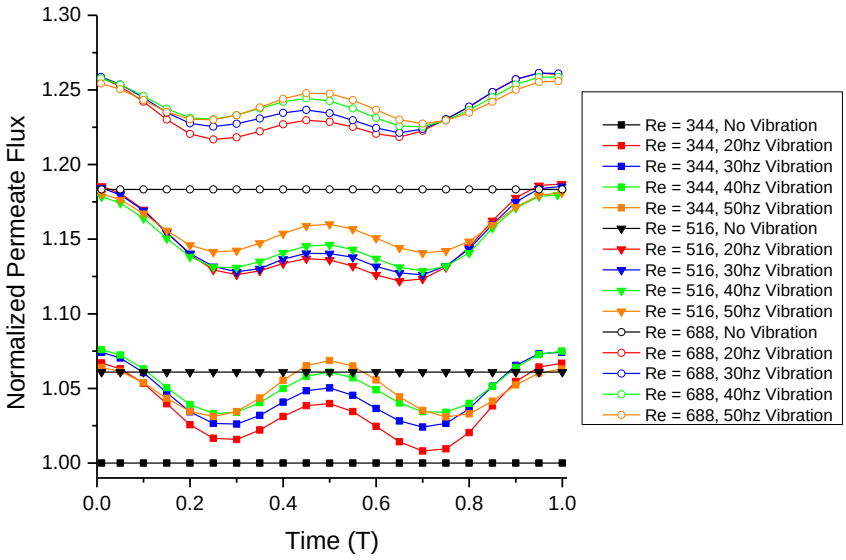

Figure 18. Normalized permeate flux variation with time.
Reprinted with permission from [82]

3.4.5. Comparison between CFD simulation results and experimental results

Figure 19 shows very good agreement between simulation and experiment derived time averaged normalized permeate flux. The zero frequency point in this figure corresponds to the no vibration case. The trend shows that the higher the vibration frequency, the higher the permeate flux. By comparing the 50 Hz and non-vibration cases for Re = 516, a maximum increase of 10 % was found. As expected, Figure 18 and Figure 19 show similar trends for the dependency of permeate flux on Re and frequency.

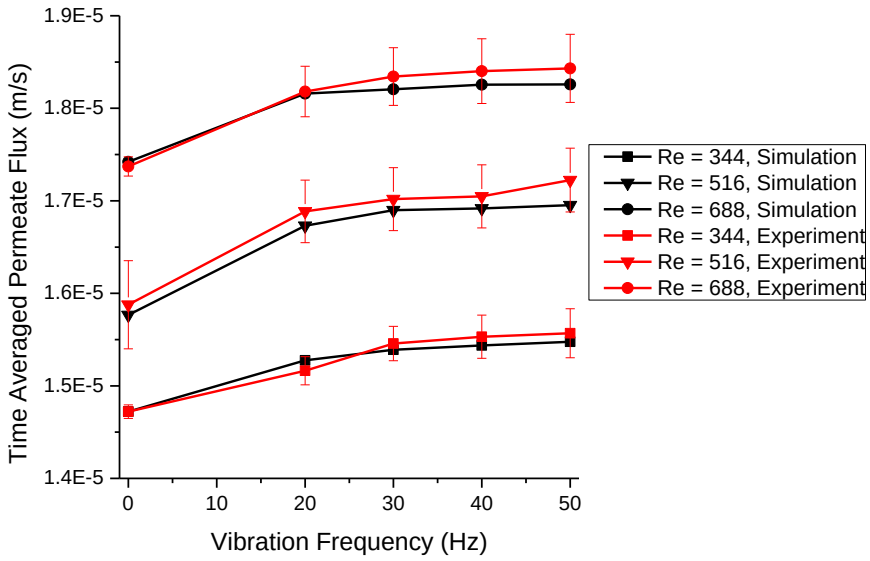

Figure 19. Time-averaged permeate flux in both simulations and experiments. *Reprinted with permission from [82]*

3.5. Conclusions

The effectiveness of a new approach to desalination utilizing RO membrane vibration was confirmed utilizing experimentation with artificial seawater and by CFD simulations including coupled motion and mass transfer equations. The CFD simulations provided highly accurate, time-dependent membrane surface permeate flux distribution, *NaCl* and $CaSO_4$ concentration polarization profiles, and mass transfer and flow patterns in the spacer-filled channel over one vibration time period. The CFD derived transient flow patterns were intuitively consistent for the non-vibration and vibration cases. The CFD predicted eddies near the membrane surface in the vibration cases reduced the

NaCl and $CaSO_4$ concentration polarization and consequently increased the membrane mass transfer rate. The reduced membrane $CaSO_4$ concentration polarization resulting from the imposed vibration also reduces the membrane local gypsum fouling rate. The simulations showed that the CP modulus decreases and the permeate flux increases as the vibration frequency increases, with a constant amplitude imposed vibration. The improvements in CP and flux change rapidly up to 20 Hz, and then slow considerably for higher frequencies. This suggests that in tuning the vibratory system it is important to locate and use the minimum frequency above which added benefits are relatively small. This will save power and equipment costs. This result was also confirmed by experimental measurements.

4. COLLOIDAL FOULING LAYER EVOLUTION FOR REVERSE OSMOSIS MEMBRANE SYSTEM WITHOUT VIBRATION

A two-dimensional numerical model simulating colloidal particle deposition and fouling was developed by integrating fluid flow and solute mass transfer inside the membrane feed channel. This model is able to animate the process of colloidal fouling accumulation by simulating the process of colloidal particles deposition on membrane surface and occupying the fluid zone into the porous cake zone. The cake layer was treated as homogeneous porous media domain with constant porosity. This model predicts the porous cake layer thickness distribution among membrane surface and its effects on the cake-enhanced osmotic pressure (CEOP). The performance of the membrane system under the influence of silica colloidal fouling in terms of initial permeate flux, channel Reynolds number, concentration of silica particles and feed spacers were investigated using this model. Model simulations are validated against experimental data of permeate fluxes with good agreement.

4.1. Introduction

Crossflow membrane filtration is one of the most economic approaches for seawater and brackish water desalination. Membrane concentration polarization (CP) phenomenon, which is caused by the accumulation of rejected solutes and particles, will increase particle concentration at the membrane surface for both clean and fouled

membranes. Several experimental and numerical investigations were performed to study the CP effect without considering the effect of membrane fouling [11,17,18,82].

When talking about the long-term operation performance, membrane colloidal fouling may be considered a critical problem since it will greatly reduce the membrane lifetime and increase the membrane surface CP. The salt ion back-diffusion is hindered inside the fouling layer [32]. Therefore, the CP phenomenon of salt solutes at the membrane surface is significantly increased which will greatly enhance the corresponding osmotic pressure. This phenomenon is the so-called *cake enhanced osmotic pressure* (CEOP) effect. Simulations ignoring the CEOP phenomenon have been reported to overestimate the effect of 'cake resistance' itself on permeate flux decline [30].

The concept of critical flux is utilized to predict the membrane performance under the effect of fouling. Noticeable flux decline with time does not occur when a membrane system operates below the level of critical flux [21], and operation above the corresponding critical flux level will cause particle deposition and cake layer formation. The critical flux theory has been widely used to characterize the membrane colloidal fouling [83].

In this chapter, a novel mechanistic model, which includes both the critical flux theory and the CEOP phenomenon, is proposed to analyze the process of membrane colloidal fouling. The cake layer, which was treated as homogeneous porous media, was generated by colloidal particles occupying the fluid domain inside the channel. In this

process, the porous cake layer formed by colloidal particles also reduces the channel height, and affects the hydrodynamics inside the channel flow. Concentration dependent fluid properties and an axial variation of permeate flux were considered in the simulation model. The animation of the colloidal fouling layer growth with time was obtained based on this simulation model. Then, the impacts of membrane desalination system operation conditions were studied. Finally, model simulation results were compared with experimental data.

4.2. Theory

4.2.1. Fluid flow governing equations

The hydrodynamics of the two-dimensional steady state flow inside a spacer-filled RO membrane channel can be described by the following governing equations:

Continuity equation:

$$\frac{\partial(\rho u)}{\partial x}+\frac{\partial(\rho v)}{\partial y}=0 \tag{35}$$

Momentum equations:

$$\frac{\partial(\rho u^2)}{\partial x}+\frac{\partial(\rho uv)}{\partial y}=-\frac{\partial P}{\partial x}+\bigtriangledown\cdot(\mu\bigtriangledown u) \tag{36}$$

$$\frac{\partial(\rho uv)}{\partial x}+\frac{\partial(\rho v^2)}{\partial y}=-\frac{\partial P}{\partial y}+\nabla\cdot(\mu\nabla v) \tag{37}$$

Since the concentration of colloidal particles is much lower than the concentration of sodium chloride, the influence of the colloidal particles on fluid properties was ignored. The sodium chloride concentration-dependent fluid properties such as density, viscosity, osmotic pressure and diffusivity were shown in Table 6 [74], where c_n is the sodium chloride concentration with the unit of $g\ g^{-1}$ and data in this table is valid for $0 < c_n < 0.09$. It should be noted that, although the effect of pressure on fluid density is neglected and the flow velocity is below the Mach number, fluid density is not a constant and can be treated as a function of the local sodium chloride concentration. The density change is relatively small (less than 3%) and it is not sufficient to generate pressure waves.

Table 6. Concentration dependent fluid properties.

Density ρ ($kg\ m^{-3}$)	$997.1\times(1+0.696\ c_n)$
Viscosity μ ($\times 10^3\ Pa\ s$)	$0.89\times(1+1.63\ c_n)$
Osmotic pressure π (bar)	$805.1\times\ c_n$
Diffusivity $D_{n,0}$ ($\times 10^9\ m^2\ s^{-1}$)	$max(1.61\times(1-14\ c_n), 1.45)$

4.2.2. Porous cake filtration model

The cake filtration model has been widely adopted to analyze membrane permeate flux [84]. Prior to membrane fouling, the permeate flux may be expressed as:

$$J = \frac{\Delta P - \Delta \pi}{\mu R_m} \tag{38}$$

where ΔP is the applied transmembrane pressure, R_m is the membrane intrinsic resistance, μ is the fluid dynamic viscosity, and $\Delta \pi$ is the sodium chloride osmotic pressure difference across the membrane.

For a fouled membrane, an additional hydraulic resistance R_c caused by the porous cake is added in series to increase the total effective resistance:

$$J = \frac{\Delta P - \Delta \pi}{\mu (R_m + R_c)} \tag{39}$$

It should be noted that R_c is not the only difference between the two systems. For a fouled membrane, the porous cake increases the concentration polarization at the membrane surface and the osmotic pressure difference term, $\Delta \pi$. By increasing the total hydraulic resistance and *NaCl* concentration at the membrane surface, the colloidal fouling cake reduces the membrane performance and permeate production rate.

The cake resistance R_c can be deduced from the mass of the colloidal particle deposited per unit membrane area m_c, since:

$$R_c = \alpha_c m_c \tag{40}$$

where α_c is the specific cake resistance and can be estimated via the Carman-Kozeny equation [85]:

$$\alpha_c = \frac{45(1-\varepsilon)}{\rho_c a^2 \varepsilon^3} \tag{41}$$

where ε is the local cake porosity, ρ_c is density of colloidal particle, and a is the radius of colloidal particle. In this study, porosity of fully deposited cake layer is assumed to be a constant = 0.4 [86].

4.2.3. Solute NaCl mass transfer and CEOP effect

The two-dimensional transient transportation of solute *NaCl* was depicted by the following convection-diffusion equation:

$$\frac{\partial(\rho c_n)}{\partial t} + \frac{\partial}{\partial x}(\rho u c_n - D_n \frac{\partial c_n}{\partial x}) + \frac{\partial}{\partial y}(\rho v c_n - D_n \frac{\partial c_n}{\partial y}) = 0 \tag{42}$$

where c_n and D_n are the concentration and diffusion coefficient of *NaCl*.

For a desalination system with a fouled membrane, the fouling cake is on the membrane surface and is assumed to be an isotropic porous medium for both fluid flow and solute transport [34]. Equation (42) can be applied in both the fluid domain and the porous cake domain. Inside the porous cake domain, the solute needs to transport

through tortuous paths towards the bulk flow. As a result, the solute back diffusion is hindered by the porous cake and concentration polarization is increased. This is known as the cake enhanced osmotic pressure (CEOP) phenomenon [30,31]. In order to depict the influence of CEOP phenomenon on the local mass transfer, the *NaCl* solute diffusion coefficient inside the porous domain is revised by considering the cake porosity [32]:

$$D_n = D_{n,0}\frac{\varepsilon}{\tau} \tag{43}$$

where $D_{n,0}$ is the diffusivity without effect of porous media which can be obtained by Table 6, ε is local cake porosity; $\tau\left(\approx 1-\ln\varepsilon^2\right)$ is local cake tortuosity.

By equation (43), the porous cake greatly reduces the salt mass transfer near the membrane surface. As an example, for a cake layer with porosity of 0.4, the expected effective solute diffusivity is only 14% of the unhindered solute diffusivity. This will result in a much higher membrane surface concentration polarization value compared with clean membrane.

4.2.4. Colloidal particle mass transfer and critical flux concept based deposition model

The concept of critical flux was introduced by Field et al. [21] and has been widely used to analyze membrane performance and characterize colloidal fouling [87]. Noticeable flux decline with time does not occur when a membrane system operates below the level of critical flux [88]. Operation above the corresponding critical flux level will cause particle deposition and cake layer formation. In other words, this can be seen

as a 'steady-state' system and this steady-state permeate flux can be treated as its critical flux. Based on the concept of critical flux, net flux $(J - J_{crit})$ is used in this study to identify whether colloidal particles will be deposited on the membrane surface or not. The particle deposition rate S_c is assumed to be proportional to the local net flux $(J - J_{crit})$ and the colloidal particle concentration $c_{c,b}$:

$$S_c = \theta c_{c,b}(J - J_{crit}) \tag{44}$$

where θ is the deposition fraction of colloidal particles, which has the range of 0 to 1. Since the permeate flux can be calculated using equation (39) and the particle concentration is also given, the only unknowns are the critical flux, J_{crit}, and the deposition fraction, θ.

S_c can be expressed as the deposited colloidal particle mass per unit time per unit area. In the particle deposition process, colloidal particles dissolved in the liquid solution are consumed and converted to porous cake. Particle deposition behaves as a solute sink term of the particle solute in the liquid phase. To describe the colloidal particle mass transfer, the convection-diffusion equation needs to be rewritten by subtracting this particle deposition term:

$$\frac{\partial(\rho c_c)}{\partial t} + \frac{\partial}{\partial x}(\rho u c_c - D_c \frac{\partial c_c}{\partial x}) + \frac{\partial}{\partial y}(\rho v c_c - D_c \frac{\partial c_c}{\partial y}) - S_c = 0 \tag{45}$$

where D_c is the effective colloidal particle diffusion coefficient.

During the fouling cake building process, there are two main forces acting on the colloidal particles near the membrane surface: the crossflow induced back diffusion force transports the accumulated colloidal particles back to the bulk flow, and the drag force induced by the permeate flux pushes the colloidal particle towards the membrane. The solute temporary equilibrium is obtained when the diffusion back-transport force is equal to the drag force. Several different transport mechanisms were reported to be responsible for the particle back diffusion. Considering the low crossflow velocity in this investigation and sizes of typical silica colloidal particles, only Brownian diffusion and shear-induced diffusion are discussed here [37].

For dilute suspension crossflow filtration, assuming that Brownian diffusion dominates the particle transport, the length-averaged permeate critical flux can be obtained by solving the governing convection-diffusion equation [89]:

$$J_{crit,br} = 1.31 \cdot (\frac{\dot{\gamma} D_{br}^2}{L})^{\frac{1}{3}} \cdot ln(\frac{\phi_{c,m}}{\phi_{c,b}}) \tag{46}$$

where L is the membrane length, $\Phi_{c,m}$ is the particle volume fraction at the membrane surface, and $\Phi_{c,b}$ is the particle volume fraction in the bulk flow, and D_{br} is the Brownian diffusion coefficient of colloidal spheres and can be calculated by the Stokes-Einstein equation [90]:

$$D_{br} = \frac{kT}{6\pi\mu a} \tag{47}$$

where k is Boltzmann constant, T is the fluid temperature, μ is the fluid viscosity, and a is the particle radius.

For colloidal suspensions, the theoretical permeate flux predicted by Brownian diffusion is much less than the experimental results, which is the so-called *flux paradox* [91]. Brownian diffusion was found to dominate only in cases with small diameter particles and very low shear rate. The velocity gradient at the membrane surface caused by crossflow and membrane vibration definitely increases the particle back diffusion coefficient. The shear-induced diffusion mechanism needs to be combined with the Brownian diffusion to accurately predict the particle back diffusion and critical flux profile.

In cases where shear-induced diffusion is the dominating back diffusion mechanism, the shear-induced diffusion coefficient can be calculated as [92]:

$$D_{sh} = 0.03\dot{\gamma}a^2 \tag{48}$$

By inserting the expression of the shear-induced diffusion coefficient into the Leveque expression, the expression for the corresponding length-averaged critical flux based on shear-induced diffusion becomes [92]:

$$J_{crit,sh} = 0.078 \cdot \dot{\gamma}(\frac{a^4}{L})^{\frac{1}{3}} \cdot ln(\frac{\phi_{c,m}}{\phi_{c,b}}) \tag{49}$$

Comparing equations (46) and (49), it can be found that Brownian diffusion dominated critical flux increases with the shear rate to the 1/3 power while shear-

induced diffusion dominated critical flux is proportional to the shear rate. The shear rate near the membrane surface and the corresponding critical flux are increased by vibrating the membrane module. The effective diffusion considering both back-transport mechanisms can be expressed by simply adding the values together [37,93]:

$$D_s = D_{br} + D_{sh} = \frac{kT}{6\pi\mu a} + 0.03\dot{\gamma}a^2 \tag{50}$$

Similar to effective diffusion, as suggested by Ingmar and Christian [20], the effective critical flux can be described by:

$$J_{crit} = \sqrt{J_{crit,br}^2 + J_{crit,sh}^2} \tag{51}$$

Equation (51) gives the final express for the critical flux combining the effects of the Brownian diffusion mechanism and the shear-induced diffusion mechanism. The value of critical flux is not enough to calculate the particle deposition rate using equation (44), the expression of deposition fraction, θ, is also needed.

Not all particles at the fluid-cake interface are deposited to form part of the porous cake during the particle deposition process. Only the fraction θ of particles will successfully deposit on the interface, and the remaining (1 - θ) will be carried back to the bulk flow. Knutsen and Davis [94] proposed that particle-rolling caused by the viscous shear flow may be the reason for the fractional deposition phenomenon. Higher shear rate at the membrane surface will enhance the particle rolling and reduce the particle deposition fraction. Experiments performed by Chong and Fane [38] show that the

fractional deposition of particles is a function of crossflow velocity during the colloidal fouling process in a flat-channel membrane system. Higher crossflow velocity in a flat-channel means higher membrane shear rate, which coincides with Knutsen and Davis's findings. In this study, the relationship between deposition fraction and crossflow velocity found by Chong and Fane [38] was adopted and transferred as the relationship between deposition fraction and shear rate:

$$\theta = \begin{cases} 1 & \dot{\gamma} < 214.29 \\ 1.2502 - 1.1676 \times 10^{-3} \dot{\gamma} & 214.29 < \dot{\gamma} < 985.71 \\ 0.0993 & \dot{\gamma} > 985.71 \end{cases} \quad (52)$$

The particle deposition rate term will also change the colloidal particle mass transfer and thus the hydrodynamics inside the membrane channel. At this point, all variables shown in equation (44) are defined and the particle deposition rate S_c for each cell can be calculated.

4.2.5. Fouling model summary

The above discussions yield the following conclusions for a given membrane desalination system:

1. Increasing the amount of colloidal particles in the feed solution increases the colloidal particle deposition.

2. Increasing the actual value of permeate flux increases colloidal particle deposition.

3. Areas with higher shear rate $\dot{\gamma}$ have lower local deposition fraction θ and higher local critical flux Jcrit. Thus, areas with higher shear rate $\dot{\gamma}$ have less colloidal particle deposition.

4.3. CFD Simulation, Numerical Method and Experimental Design

4.3.1. Model geometry and boundary conditions

The geometry analyzed in this study is a rectangular 2D membrane channel filled with 'zigzag' cylindrical spacers. This 'zigzag' geometry with l_m = 2.85 mm and r_s = *1/4 h* = 0.195 mm is similar to spacer-filled channels in industry applications. Each set of two successive spacers comprises one 'cell element' as shown in Figure 20. An array of 10 ‘cell elements’ makes the membrane area which has a length of 57 mm. The long entrance area before the membrane and the long exit area after the membrane are necessary to avoid the influence of inlet and outlet boundary conditions on membrane performance and flow development. Entrance and exit lengths are chosen as 30 and 50 times the spacer radius respectively, in this study.

A fully developed velocity profile and the constant concentrations of the solutes are given at the channel inlet. The velocity gradient and solute concentration gradient are assumed to be zero at the channel outlet since the outlet boundary is far away from the membrane zone. All wall surfaces, including the top impermeable wall, the feed spacer wall, the entrance and exit area walls, have no slip and no solute flux boundary conditions. No slip boundary conditions ($u = 0$) are also applied, and the permeate

velocity J is specified ($v = -J$) on the bottom membrane boundary. The diffusive and convective fluxes must be balanced for both *NaCl* and silica particle solutes:

$$D_n \frac{\partial c_n}{\partial y} = -J c_n R_{n,rej}$$
$$D_c \frac{\partial c_c}{\partial y} = -J c_c R_{c,rej} \quad (53)$$

where J is the membrane local permeate flux determined by equation (39). The terms $R_{n,rej}$ and $R_{c,rej}$ are the membrane intrinsic rejection factors for *NaCl* and silica colloidal particles, respectively, and are assumed to be 0.98 and 1, respectively.

A structured mesh generated using ICEM-CFD (ANSYS Inc., Canonsburg, PA) was adopted in the simulations and was validated by conducting a mesh independence test. The mesh near the membrane is much finer due to the expected large concentration gradient. This made the numerical implementation approach shown in section 4.4.2. sufficiently accurate for this study. The first cell height on the membrane boundary and spacer wall boundary is 0.8 μm and 3 μm, respectively.

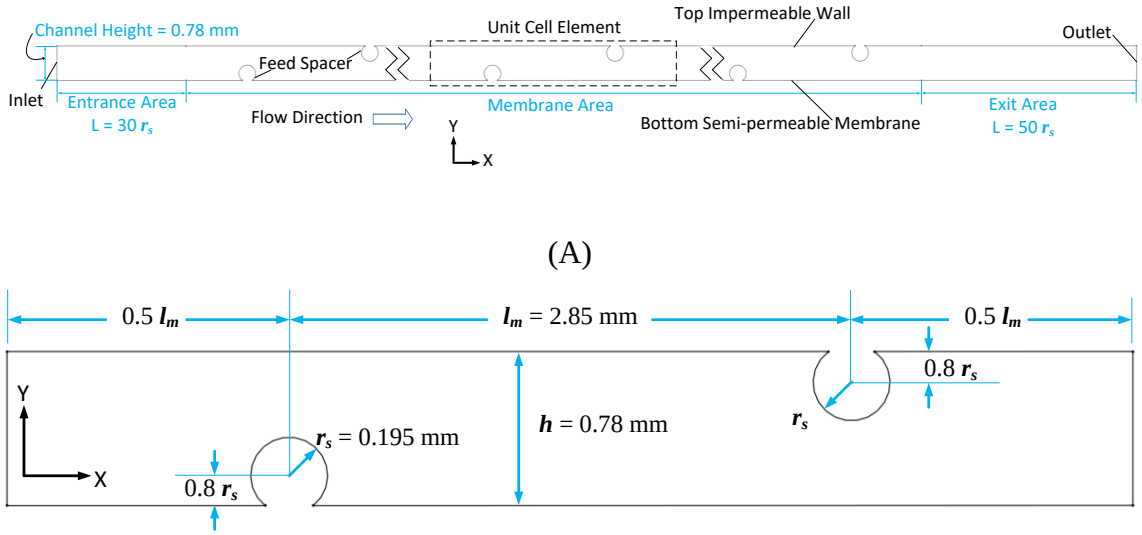

Figure 20. The schematic of geometry. (A) The whole simulation domain. The dashed box shows one unit cell element. (B) One unit cell element.

4.3.2. Numerical implementation of fouling layer evolution

Colloidal particle deposition first appears at the membrane surface as depicted in Figure 21. Once the silica colloidal porous cake begins particles will continue to deposit at the fluid-cake interface and increase the cake thickness. This fouling cake growth will reduce the flow area and change the mass transfer and hydrodynamics which will indirectly change the local fouling rate itself. A model was developed to approximate the fouling layer height and fluid cell porosity changes during the particle deposition process. The model simplifies the actual spatially continuous physical gradual deposition process into a cell by cell approximation.

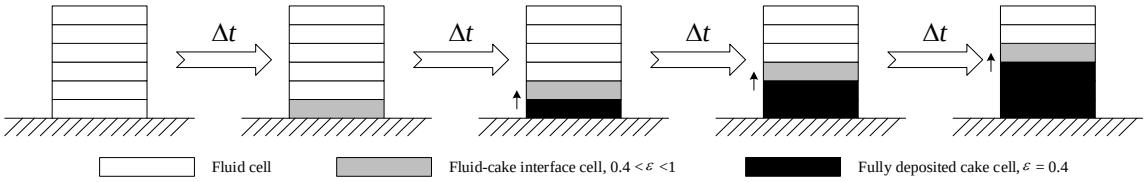

Figure 21. Scheme of the numerical treatment for the fouling cake growth.

As shown in Figure 21, a clean membrane is used at the beginning of the calculation. All computational cells above the membrane surface should be fluid cells. Colloidal particles will first deposit inside the first layer cell. This cell is the fluid-cake interface cell and will be treated as a porous media. The cell fouling thickness can be expressed as:

$$h_{cell,c} = \frac{1-\varepsilon}{1-\varepsilon_{min}} h_{cell} \tag{54}$$

where $m_{cell,c}$ is the accumulated fouling mass in this cell, ρ_c is the particle density, A is the cell bottom face area, and ε_{min} is the porosity of fully fouled cake cell which is assumed to be 0.4 [86]. In order to reduce computational time the cell height is not incremented continuously, but instead the cell porosity is varied as $h_{cell,c}$ varies from equation (54). In this manner, the cell porosity will be gradually reduced from 1 to the minimum porosity during the cell fouling process. The equivalent effective cell porosity is determined from:

$$\varepsilon = 1 - \frac{m_{cell,c}}{\rho_c A_{cell}} \tag{55}$$

where h_{cell} is the cell height, and $h_{cell,c}$ is the cell fouling thickness. Once the cell fouling thickness $h_{cell,c}$ reaches the top of this cell, particles will no longer be deposited in the cell, instead, the deposition process will ensue in the cell above this one. This cell will then be treated as 'fully deposited cake cell', at the same time, the cell above this one will be converted externally from a fluid cell into a porous media cell. This growth process is shown in Figure 21 and is similar with the method used by Paz [95] and El-Batsh [96]. For visualization purpose, the heights of cells shown in Figure 21 are not scaled.

4.3.3. Model solution

Fluent (ANSYS Inc., Canonsburg, PA) was used here as the CFD package to solve the coupled continuity, momentum and solute transport equations via the SIMPLEC algorithm. Due to the limitation of the available calculation resource and the long time needed to calculate all 35 cases for 12 hours' operation time, LES model adopted in the previous chapter was not applied in the simulation this chapter. Instead, the *RNG k-ε* model was used to simulate the turbulence effects caused by the spacer inside the narrow channel. Compared with the general *k-ε* model, the *RNG k-ε* model is more suitable for simulating a channel with spacers since it can accurately solve eddy development at relatively low Reynolds numbers. Figure 22 illustrates the approximate method used to model the colloidal fouling layer evolution with time inside the

membrane channel. The simulation model begins as a clean membrane channel, without silica colloidal particle deposition. The governing equations are then solved by FLUENT for both the fluid and porous media domains as time continues. Detailed steady state flow and solutes concentration fields are calculated, then the cake filtration and fouling equations provide the fouling deposition results to update the mesh and fluid properties for the next time step. Cells with fouling deposition are treated as porous media cells with constant porosity, and the remaining cells are treated as fluid cells. The updated fluid-porous domain model is then used for the next time step. This loop is repeated until the calculation time reaches the pre-set limit.

Batch processes and User Defined Function (UDF) subroutines were utilized to determine cell fouling status, cell cake fouling height, cell fouling particle deposition rate, cell local porosity and for changing the status of a cell from fluid to porous media. The time step depended on the value of averaged deposition rate, and was varied from 0.1 to 30 minutes to ensure that the fouling layer thickness change was not significant within the time step.

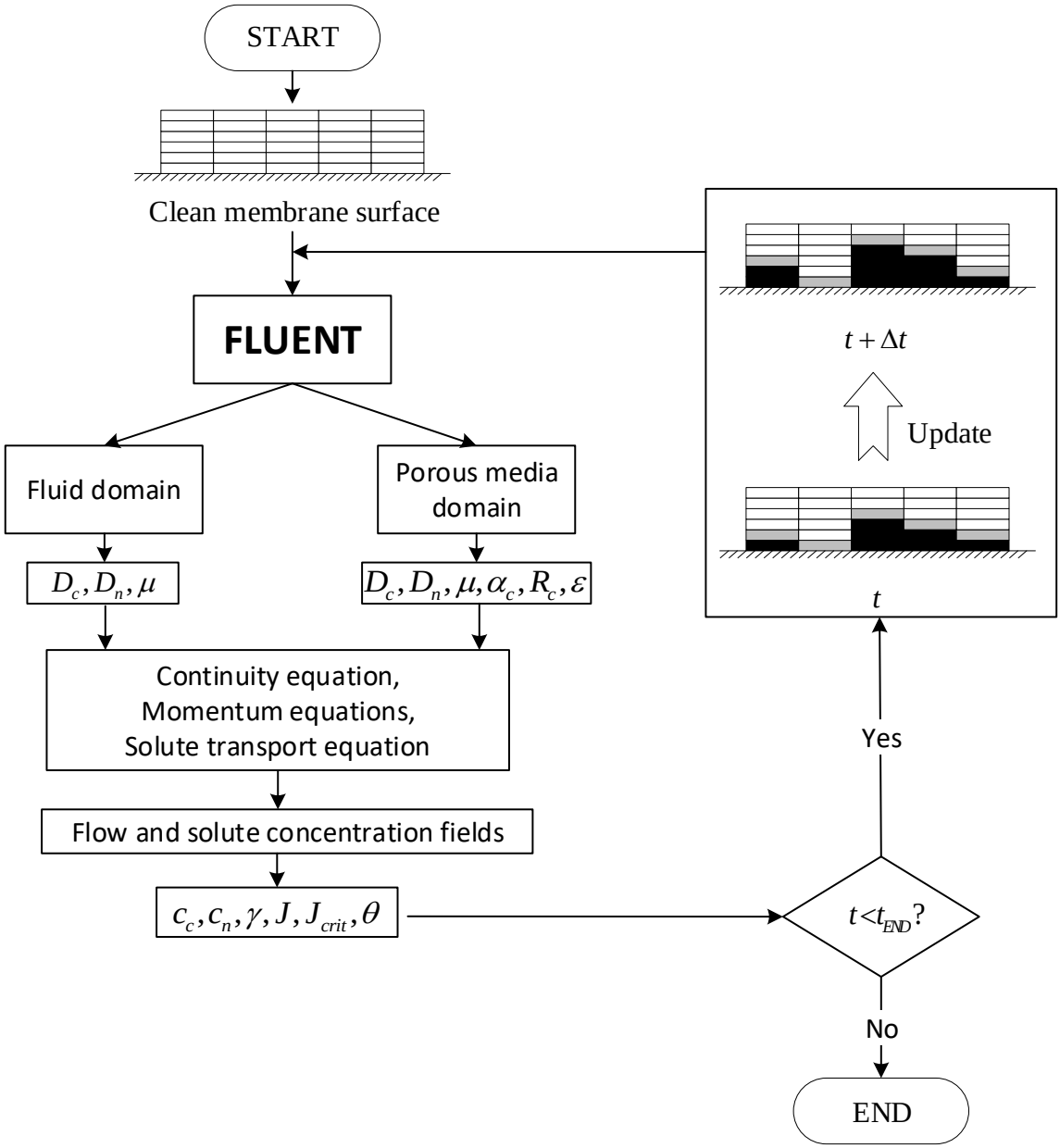

Figure 22. Scheme of fouling calculation loop.

4.3.4. Experimental design

A commercial RO membrane (Hydrnautics, model SWC6 MAX) was used in all experiments. The detailed specifications for this membrane are shown in Table 3 [66]. Each membrane sheet had the membrane size of 20 cm length × 3 cm width , resulting in 60 cm^2 effective membrane area. Silica colloids (Aerosil 200, Evonik Industries) and sodium chloride (Fisher Scientific) were used as colloidal fouant and the background ionic solution respectively. This silica particles have a specific surface area in the range of 175 to 225 m^2/g, a density of 2.2 g/cm^3 [97], and the mean hydrodynamic radius of 120 nm [28].

The same experimental system used in Chapter 3 was also adopted here. Figure 2 presents the diagram of the cross flow RO membrane desalination cell. The only difference is that vibration is not applied in the study in this Chapter.

A new membrane was used for each test and was first compacted using distilled water at an operating pressure of 55 bar for at least 4 h until a stable baseline permeate flux was obtained.

For the fouling tests, no pre-filtrations or other pretreatments were applied to the feed solution. A typical fouling test lasts for 12 hours. The permeate flux was collected and measured at intervals of 20 minutes. Permeate flow was poured back to the feed tank after measuring in order to keep the feed water salinity nearly constant.

Feed solution temperature is one of the key factors affect the performance of reverse osmosis membranes. During the fouling tests, the feed solution temperature was

controlled in the temperature range of 15 ± 2 °C and measured by a J-type thermocouple with 0.1 °C accuracy. The calculated permeate flux was corrected according to the temperature correction factor (TCF) theory to eliminate the effect of temperature fluctuations of the feed water during the fouling tests. For the RO membrane used in this investigation, an empirical formula was applied to get the corresponding TCF values:

$$TCF = e^{k_t\left(\left(\frac{1}{288}\right)-\left(\frac{1}{T}\right)\right)} \tag{56}$$

where T is the temperature of feed solution and k_t is a coefficient constant for a given membrane desalination system. In this equation, 288 K (15 ^{o}C) is set as the reference temperature, and k_t = 2700 is adopted [98].

4.4. Results and Discussion

Several important factors for colloidal fouling in the membrane desalination system were investigated, specifically the effect of feed flow composition, membrane system operating parameters and feed spacer presence. Table 7 summarizes cases studied in the combined CFD – experimental based investigation. The initial permeate flux is the value of the permeate flux of the membrane system at the beginning of the fouling test. At the beginning of the fouling test, the membrane is clean with no fouling particles deposited on the membrane surface. The value of the initial permeate flux can be controlled by adjusting the applied pressure of the feed pump in the experiment. In

the CFD simulation, value of the initial permeate flux is defined in the UDF code and applied to the membrane boundary.

4.4.1. Membrane desalination with silica colloidal fouling and fouling layer growth visualization

In this section, simulation case 1 (Table 7) was chosen as an example case to investigate the detailed information of flow hydrodynamics with silica colloidal fouling and the visualization of fouling layer growth.

Figure 23 presents the development of the porous cake layer growth next to membrane and corresponding velocity vector plots for different operation durations. To eliminate the effect of inlet and outlet boundary conditions, the 9^{th} unit element was chosen as representative of the entire channel. The bulk flow velocity direction is from left to right. At the beginning of the desalination process, no porous cake appears inside the feed channel. A small recirculation region is formed near the upstream face of the spacer while a larger recirculation region is located in the corresponding downstream area.

Table 7. Summary of simulation conditions for different calculated cases.

Case Set #	Inlet *NaCl* concentration $c_{n,\,b}$ (ppm)	Inlet silica colloidal concentration $c_{c,\,b}$ (ppm)	Inlet Re	Initial flux J (μm/s)	Feed Spacer	Note
1	32,000	400	400	14	Yes	Benchmark case
2	32,000	400	400	14	**No**	Impact of feed spacer
3	32,000	**200**	400	14	Yes	Impact of silica colloidal particle concentration
4	32,000	**800**	400	14	Yes	
5	32,000	400	**200**	14	Yes	Impact of Reynolds number
6	32,000	400	**600**	14	Yes	
7	32,000	400	400	**10**	Yes	Impact of initial permeate flux
8	32,000	400	400	**18**	Yes	

After a 3-hour operation, porous fouling cakes were found next to the membrane surface. There are four obvious porous cakes which are marked as 1 – 4 in this sub-figure. The positions of cake 1 and cake 4 are the stagnation points of the corresponding recirculation vortex, and cake 2 and cake 3 are located between the corresponding vortex and the feed spacer. In all these areas, the local *NaCl* concentrations are relatively high, which will be discussed in Figure 25, and the shear rates at the membrane surface are relatively low.

Sizes of all four cakes after a 12-hour operation are much larger than sizes after a 3-hour operation, with continuous cake growth. Since the vortex near the upstream face of the spacer is too small, cake 1 and cake 2 are connected and grow into one large cake during the cake growth.

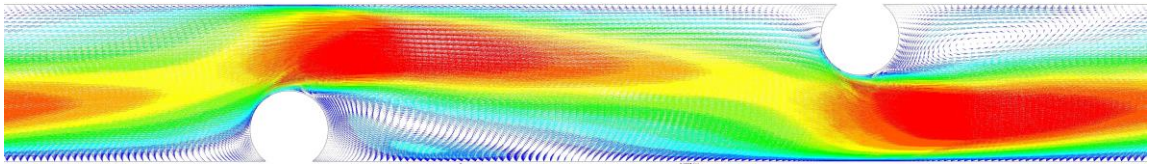

(A) initial clean membrane

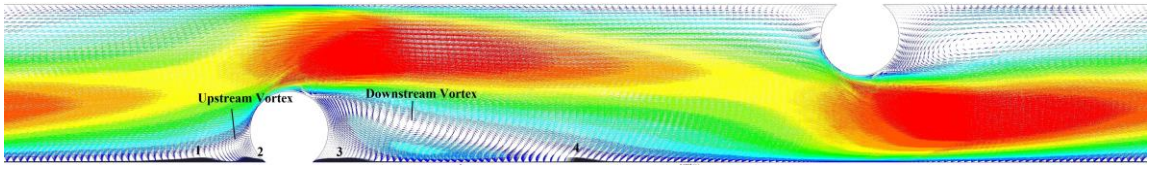

(B) 3 hours

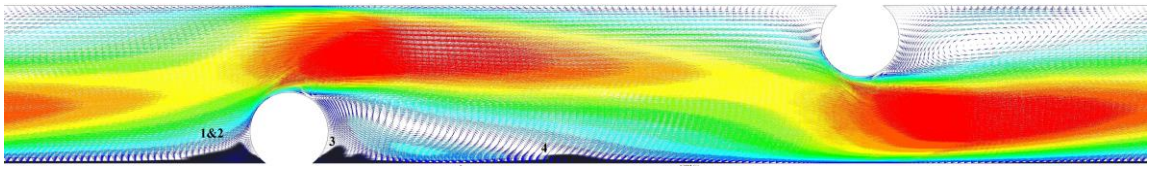

(C) 25 hours

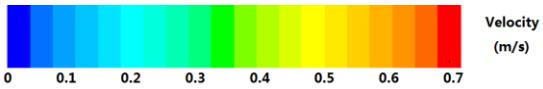

Figure 23. Development of porous cake layer growth next to membrane and corresponding velocity vector plots for different operation time: (A) initial clean membrane, (B) 3 hours, (C) 25 hours. Colors indicate the value of fluid velocity. Porous cake is shown in black next to the membrane surface.

In summary, colloidal porous cakes will grow in both membrane coverage and cake height with the increase of membrane system operation time. Big colloidal porous cakes can be found on the membrane surface near feed spacers. Similar phenomenon can also be found in other kinds of membrane fouling growth inside the spacer-filled channel, such as mineral fouling [99] and biofouling [100]. CEOP phenomenon caused

by colloidal porous cakes will hinder the solute mass transportation and increase local *NaCl* concentration.

The *NaCl* concentration profile at the location x = 51.7 mm in the downstream area of 9th spacer from the channel inlet is shown in Figure 24. The effect of porous cake on *NaCl* diffusion leading to CEOP phenomenon is clearly presented. In Figure 24, three flow areas can be found from left to right: porous cake area, recirculation area and bulk flow area.

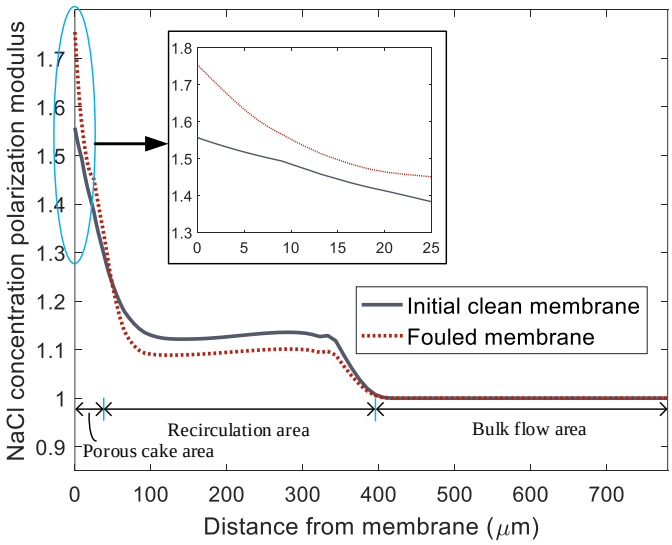

Figure 24. Comparison of NaCl concentration polarization modulus profile for the clean membrane and fouled membrane after 12 hours operation at the downstream area (x = 51.7 mm) of 9th spacer from the channel inlet.

For the clean membrane channel, a smooth *NaCl* concentration increase was found near the membrane surface with maximum CP value of 1.55. This increase is due to the membrane rejection on *NaCl* solute, which is well-known as the concentration polarization (CP) phenomenon in membrane desalination.

In contrast, *NaCl* concentration increases rapidly inside the porous cake area of the fouled membrane case due to the low effective *NaCl* diffusion coefficient within the porous cake and the lack of back-transportation to the bulk flow. *NaCl* concentration next to the membrane for fouled membrane case is about 13% higher than the clean membrane case. The increased *NaCl* concentration next to the membrane would increase the transmembrane osmotic pressure and reduce the local permeate flux under the same applied pressure. Concentration polarization is enhanced by the porous cake, which is known as the CEOP phenomenon.

Since the *NaCl* solute transportation to bulk flow is limited in the fouled membrane case, the concentration inside the recirculation area for the fouled membrane case is slightly lower than the clean membrane case. In the bulk flow area, both cases have the same bulk flow concentrations, which are equal to the inlet concentration.

4.4.2. Impact of feed spacer

Flat sheet membrane cells are often used in investigations of the membrane fouling under various operation conditions [101]. However, in commercial spiral wound RO systems, feed spacers are widely used since they can support the membrane leaves and increase the desalination system stability. Feed spacers have been shown to affect the fluid hydrodynamics and membrane concentration polarization in clean membrane cases [102,103] and fouling status in biofouling and inorganic fouling cases [99,100,104]. In this section, the impact of feed spacers on *NaCl* concentration distribution and membrane permeate flux of the colloidal fouling influenced membrane is analyzed. Results of simulation cases 1 and 2 (Table 7) will be discussed here.

Figure 25 and Figure 26 show the *NaCl* CP modulus and permeate flux distributions along the membrane surface for both cases with and without feed spacers. In Figure 25, *NaCl* CP modulus values increase with operation time along the membrane, for both with and without feed spacers. For the without-spacer case, the CP modulus value increases along the membrane length. At the end of membrane, the maximum CP modulus value for the 12 hours case is 1.96, which is even higher than the peak value for spacer cases. For the with-spacer cases, the sharp CP modulus peak values are around 1.85 and occur next to the feed spacer. In other areas, the CP modulus for the case with feed spacers is much lower than the corresponding case without feed spacers, even in the eddy recirculation area behind the feed spacer.

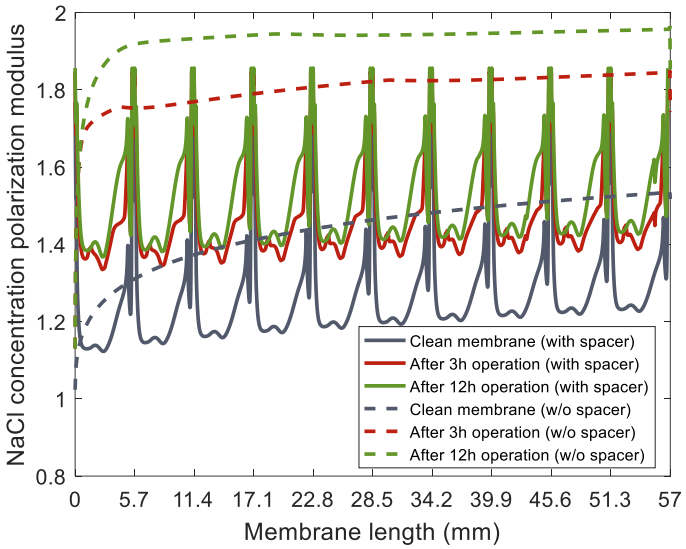

Figure 25. *NaCl* concentration polarization modulus distributions along the membrane surface for cases with and without feed spacers at different operation times.

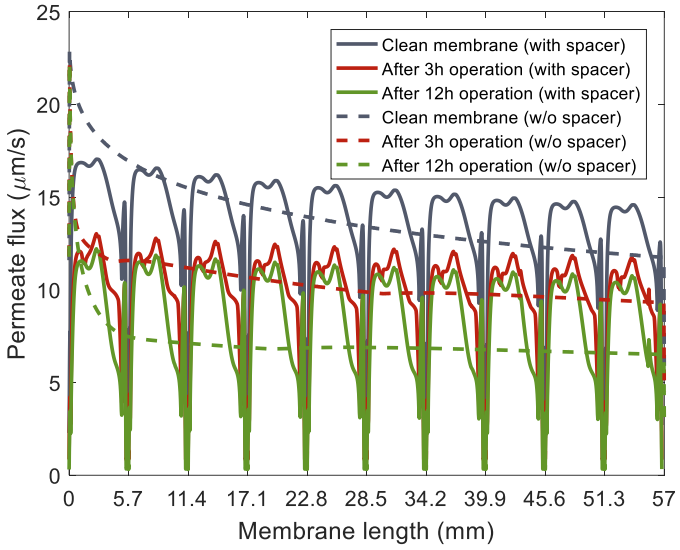

Figure 26. Permeate flux distributions along the membrane surface for cases with and without feed spacers at different operation times.

Similar conclusions can be found in the permeate flux profile in Figure 26. For both cases, permeate flux values decrease with operation time among the membrane surface. The averaged permeate flux for the with-spacer case is higher than the without-spacer case for corresponding operation times.

Figure 27 and Figure 28 are zoom views of the *NaCl* CP modulus and permeate flux distributions in the last unit cell element. High *NaCl* CP modulus can be found near the feed spacer for both the clean membrane and the fouled membrane cases. At the same operation time, *NaCl* CP modulus values in cases with feed spacers are lower compared with cases without feed spacers. After 12 hours, the *NaCl* CP modulus peak value in the with feed spacers case is even lower than the corresponding without feed spacers case. The *NaCl* CP modulus differences between the with and without feed spacer cases increase with system operation time. This increasing difference shows that feed spacers can reduce the membrane surface concentration polarization phenomenon, especially for a fouled membrane. Similar conclusions can be found in terms of membrane permeate flux. In most areas of the membrane surface, higher membrane permeate flux can be found in the with feed spacer case compared with the without feed spacer case. This improvement increases with operation time.

Figure 29 and Figure 30 show the normalized permeate flux and *NaCl* concentration polarization modulus change vs. operation time for with and without feed spacer cases. Simulation case 8 (initial permeate flux = 18 $\mu m/s$, Table 7) was included to show the effect of feed spacers.

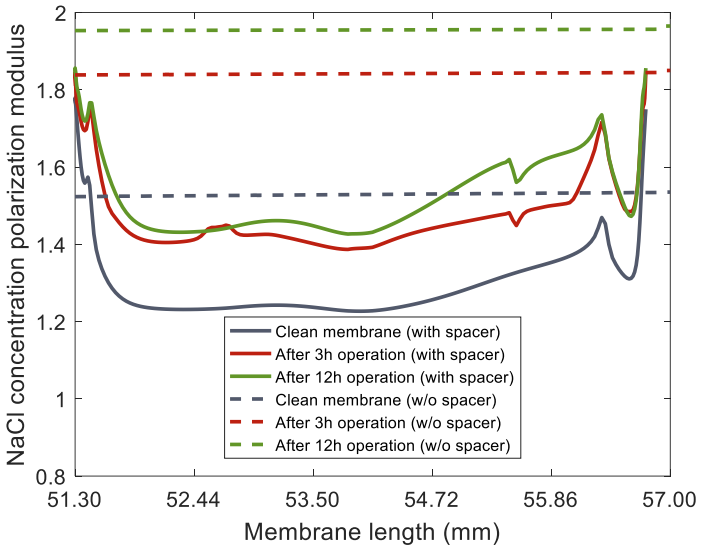

Figure 27. *NaCl* concentration polarization modulus distributions among the membrane surface for the 10th cell element in both cases with and without feed spacers at different operation time.

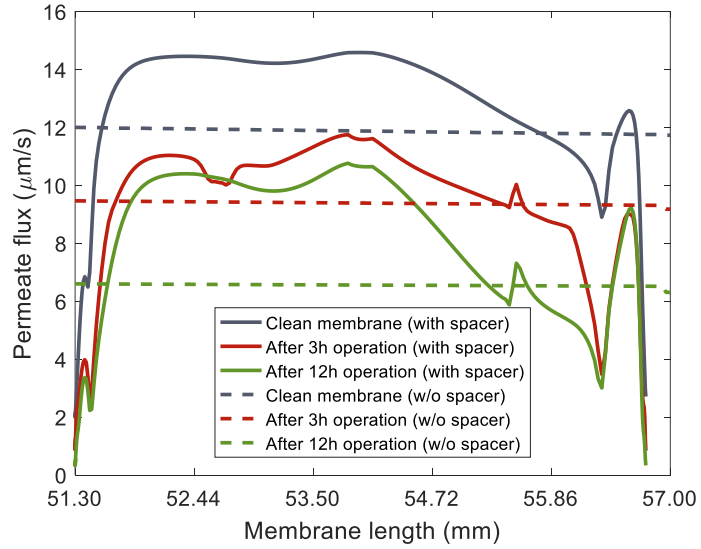

Figure 28. Permeate flux distributions among the membrane surface for the 10th cell element in both cases with and without feed spacers at different operation time.

Initially, the decline in the normalized permeate flux is greater in the with feed spacer cases than the without feed spacer case. This is mainly caused by the salt and particle accumulation near the feed spacers. Figure 25 and Figure 27 show that the salt concentrations are much higher near the feed spacers compared with the remaining areas. The shear rates are relatively low at the membrane surface near the feed spacers which attracts a greater level of colloidal particle deposition. This also leads to the rapid permeate flux reduction in both cases with feed spacers. The difference in normalized permeate fluxes reduces as the operation time increases. The normalized permeate flux of the without feed spacer cases becomes smaller than the corresponding with feed spacers case after the operation time exceeds 5 hours.

The normalized permeate flux for the with-spacer case is 20.8% greater than the without-spacer case after 12-hours of operation, and under the same initial permeate flux condition. Similar with the permeate flux profile, the *NaCl* CP modulus was increased by 28.2% after a 12-hour operation by removing feed spacers. Even with its higher initial permeate flux (18 $\mu m/s$), the without-spacer case still has much higher CP modulus value and lower normalized permeate flux than the with spacer case. The slope of the declining normalized permeate flux for the with feed spacers cases are much smaller compared with the without feed spacers case. It appears likely that the difference between the with and without feed spacer cases normalized permeate flux will continue to increase for times exceeding 12 hours.

The results show that the membrane surface *NaCl* CP modulus is higher for the without feed spacers case compared to the with feed spacers case during the entire 12 hours of operation.

Higher initial *NaCl* CP modulus requires a higher applied pressure to obtain the same initial permeate flux. The increased applied pressure will increase the system unit power consumption which is one of the most important indicators when evaluating a desalination plant. After 12 hours operation, the averaged *NaCl* CP modulus for case without feed spacers is 1.93 which is much higher compared with the value 1.51 for the case with feed spacers, and 1.70 for the case with feed spacers and higher initial permeate flux. Similar to the normalized permeate flux results, it is expected that the difference between *NaCl* CP modulus for the with and without feed spacers cases will increase as time increases beyond 12 hours.

4.4.3. Impact of silica colloidal particle concentration

Simulation cases 1, 3 and 4 (Table 7) are compared in this section to investigate the effect of inlet silica colloidal particle concentration on colloidal fouling. Figure 31 - Figure 33 show the change in normalized permeate flux, *NaCl* concentration polarization modulus and averaged cake height vs. operation time for different inlet silica particle concentrations. Experimental results are also included for the normalized permeate flux. Increasing silica particle concentrations is seen to increase *NaCl* CP modulus, increase cake height and decrease normalized permeate flux. The CP modulus values for all three cases are seen to nearly converge while the cake height differences continue to diverge

at the end of 12 hours of operation. These results indicate that the *NaCl* CP modulus and the CEOP effect become nearly insensitive to the inlet silica particle concentration after a certain membrane surface cake height is attained.

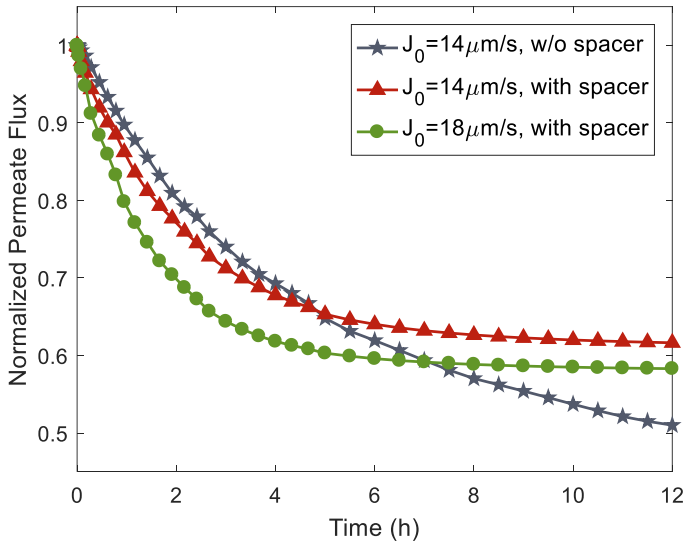

Figure 29. Change in normalized permeate flux with operation time for with and without feed spacers cases.

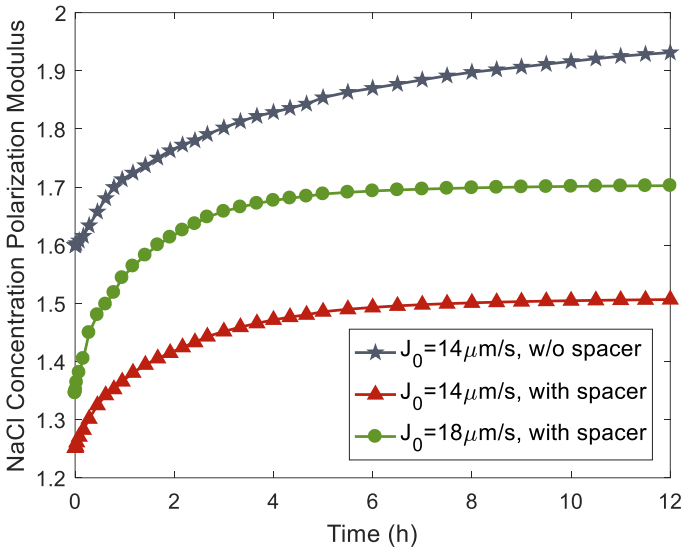

Figure 30. Change in NaCl concentration polarization modulus with operation time for with and without feed spacers cases.

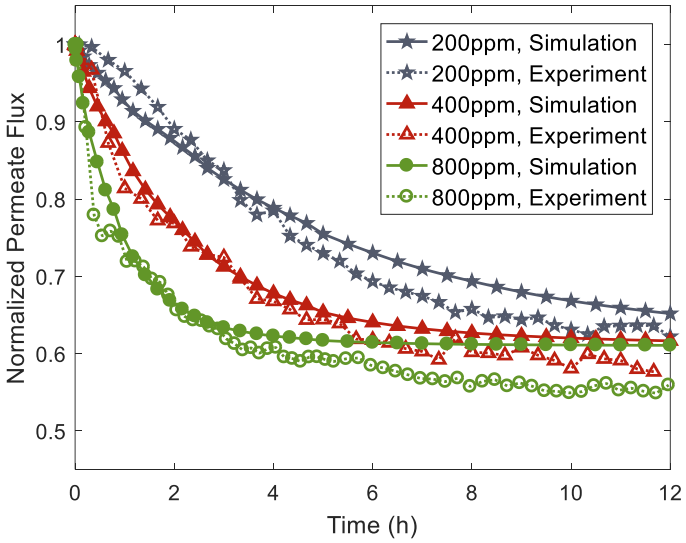

Figure 31. Change in normalized permeate flux vs. operation time for different inlet silica colloidal particle concentrations.

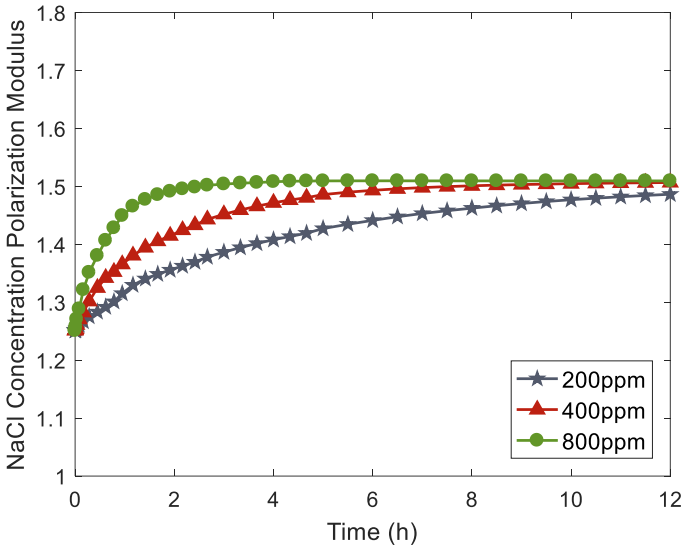

Figure 32. Change in *NaCl* concentration polarization modulus vs. operation time for different inlet silica colloidal particle concentrations.

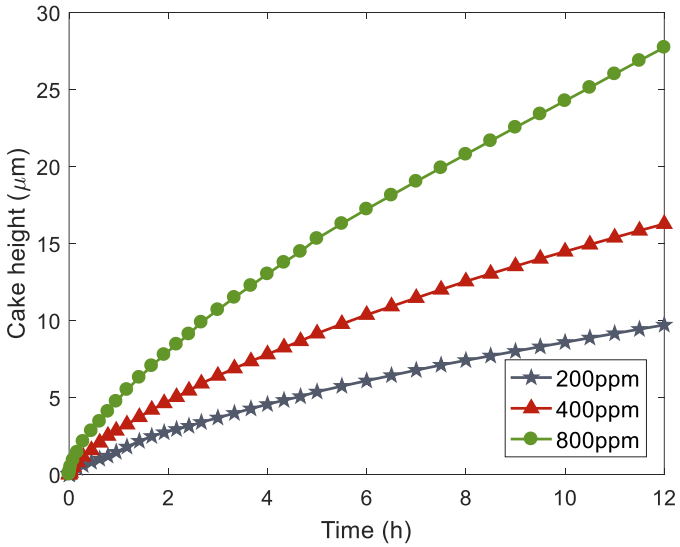

Figure 33. Change in averaged cake height vs. operation time for different inlet silica colloidal particle concentration.

4.4.4. Impact of desalination operation conditions

Figure 34- Figure 36 are obtained from simulation cases 1, 5 and 6 in Table 7, and show the change in normalized permeate flux, *NaCl* concentration polarization modulus and averaged cake height vs. operation time for different inlet Re numbers. Experimental results are also included for the normalized permeate flux. The results in these figures show that increasing inlet Re numbers improves membrane performance including lower cake height, higher permeate flux and lower *NaCl* concentration at the membrane surface. Higher inlet Re numbers have higher averaged inlet velocities which result in higher shear rates and enhance the particle mass transportation near the membrane surface. Both factors will decrease the particle deposition rate and improve the membrane performance.

Table 8 shows a comparison of membrane performance for cases with different Re number after 12 hours of operation. The improvement from Re = 200 to Re = 400 is much larger compared with the improvement from Re = 400 to Re = 600 for all three criteria including permeate flux (simulation and experiment), *NaCl* concentration, and cake height. This trend projects even lower membrane performance improvement by increasing inlet Re number for cases with Re numbers higher than 600. Pressure loss increases with increasing inlet Reynolds number [105] as does the capital costs for feed pumps with higher flow rates, and the propensity for flow instabilities. Hence there is a point of diminishing returns for improving membrane performance utilizing increased inlet Re number. Those findings point to a need to select an inlet Re number that balances membrane performance with capital cost, power loss and stable operation.

Table 8. Comparison of membrane performance after 12 hours when varying inlet Re numbers.

	Normalized permeate flux (simulation)	Normalized permeate flux (experiment)	*NaCl* CP modulus	Averaged cake height (μm)
Re = 200	0.5318	0.4881	1.7656	25.63
Re = 400	0.6164	0.5764	1.5066	16.28
Re = 600	0.6664	0.6356	1.4075	13.39
Improvement from Re = 200 to Re = 400	15.91%	18.09%	14.67%	36.48%
Improvement from Re = 400 to Re = 600	8.11%	10.27%	6.58%	17.73%

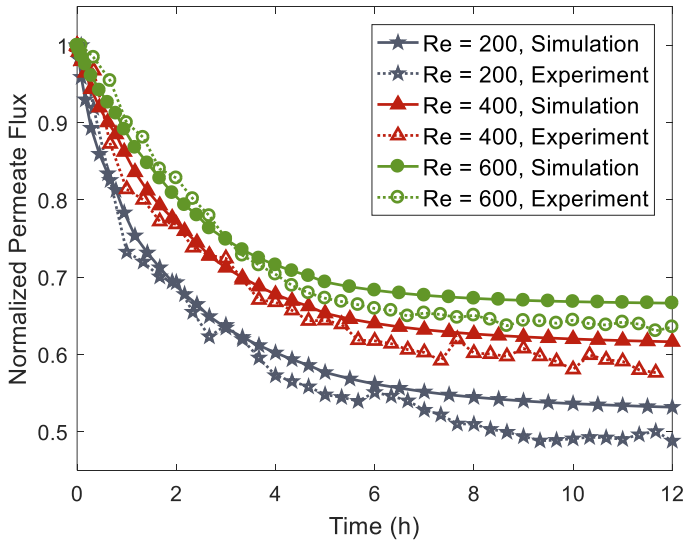

Figure 34. Change in normalized permeate flux vs. operation time for different inlet Re numbers.

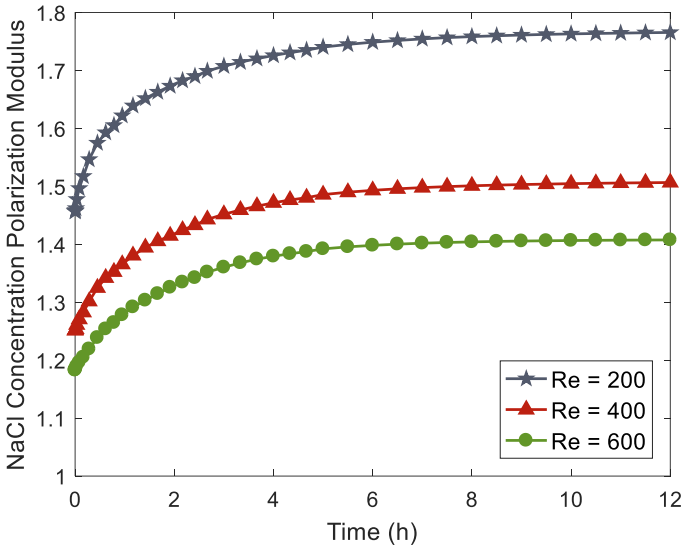

Figure 35. Change in *NaCl* concentration polarization modulus vs. operation time for different inlet Re numbers.

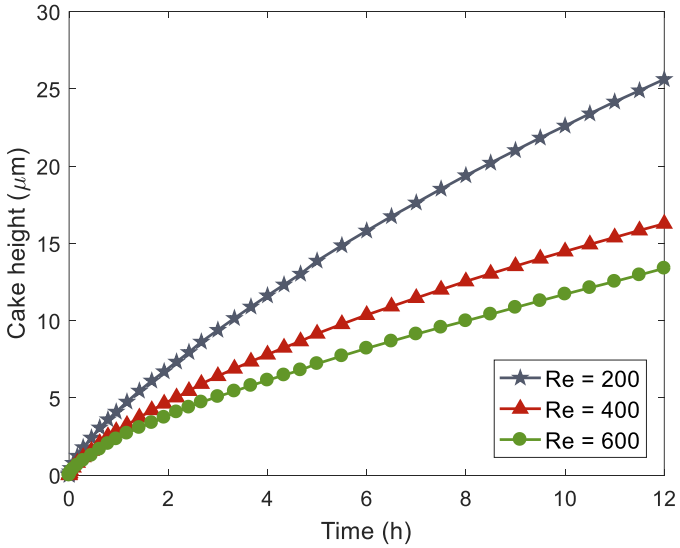

Figure 36. Change in averaged cake height vs operation time for different inlet Re numbers.

4.4.5. Impact of initial permeate flux

Figure 37- Figure 39 are obtained from simulation cases 1, 7 and 8 in Table 7, and show the change in normalized permeate flux, *NaCl* concentration polarization modulus and averaged cake height vs. operation time for different inlet permeate fluxes. Experimental results are also included for the normalized permeate flux. The cases with higher initial permeate flux are seen to have higher cake height, higher *NaCl* CP modulus value and lower normalized permeate flux during the 12 hours of operation.

The drag force created with membrane permeate flux is the primary driving force for the silica colloidal particles to deposit on the membrane surface. According to the particle deposition rate formula (equation (39)), a higher permeate flux will cause higher deposition rate and consequently a more rapid reduction of the membrane performance. Although the normalized permeate flux for the case with $J_0 = 18\ \mu m/s$ is relatively low, consideration of the high absolute value of the initial permeate flux, may yield an actual permeate flux even higher than the other two cases.

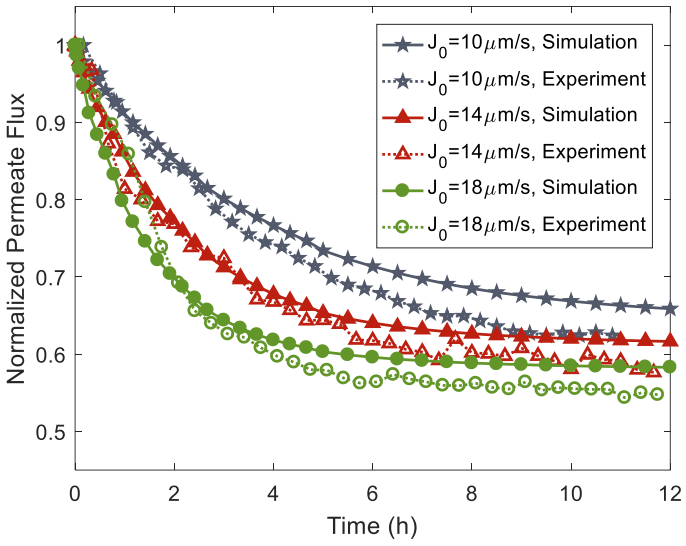

Figure 37. Change in normalized permeate flux vs. operation time for different initial permeate flux.

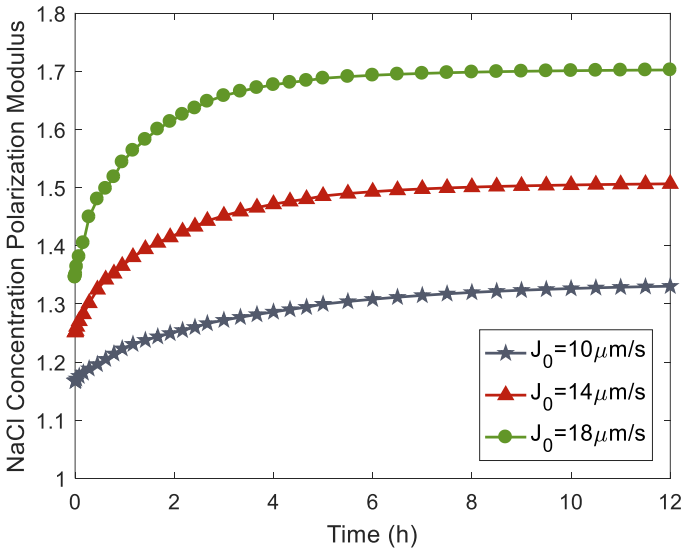

Figure 38. Change in *NaCl* concentration polarization modulus vs. operation time for different initial permeate flux.

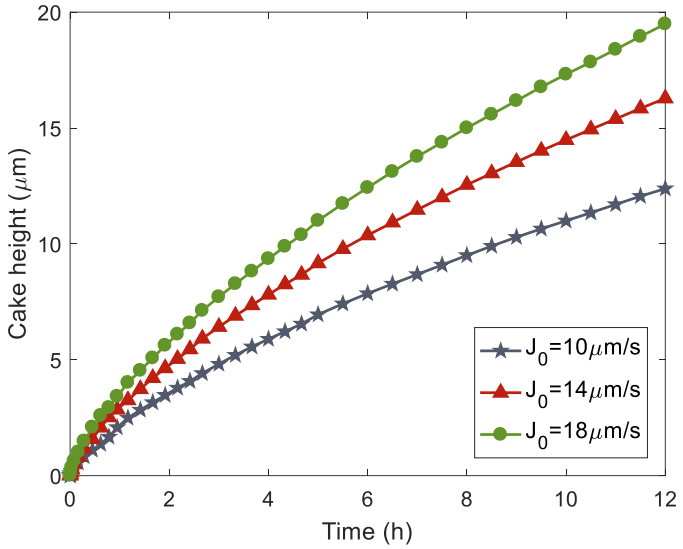

Figure 39. Change in averaged cake height vs. operation time for different initial permeate flux.

4.5. Conclusions

Membrane desalination was simulated with a two-dimensional model including colloidal particle deposition and fouling growth, and the integration of fluid flow and solute mass transfer inside the membrane feed channel. Concentration dependent fluid properties, axial variations of permeate flux and cake height, cake enhanced osmotic pressure (CEOP) effect and critical flux theory were included in the simulation model. The colloidal fouling simulation model was numerically solved utilizing the commercial Computational Fluid Dynamics (CFD) software package ANSYS FLUENT.

The animation of the colloidal fouling layer growth with time was depicted by simulating the process of colloidal particle deposition on the membrane surface and occupying the fluid zones into porous cake zones. An approximate computational approach was developed to simplify the model of gradual colloidal particle deposition into a cell by cell problem. The cell-based colloidal fouling cake layer, which was treated as a homogeneous porous media domain with constant porosity, has an effect on both fluid flow and solute mass transfer. The cake layer provides momentum resistance for flow inside the cake layer, reduces the effective channel height and changes the hydrodynamics inside the channel flow. The diffusion and concentration of *NaCl* solute was also influenced by the porous cake layer, well-known as the CEOP effect.

The influence of membrane desalination system operation parameters on membrane colloidal fouling, including initial permeate flux, inlet Reynolds number, and feed solution silica particle concentration were investigated to provide a references for future membrane system designs and upgrades. The impact of the feed spacer on membrane colloidal fouling was also studied: increased salt concentration polarization (CP) and more fouling deposition occur around the contact zones between feed spacers and membrane; however, in other areas on the membrane surface lower CP and fouling was found, which overall proves that feed spacers improve the membrane desalination performance. Lastly, model simulations are validated against experimental data of permeate fluxes with good agreement.

5. COLLOIDAL FOULING IN THE VIBRATION ENHANCED REVERSE OSMOSIS MEMBRANE DESALINATION SYSTEM

Computational fluid dynamics (CFD) simulations and experiments were performed to investigate the performance of a vibration enhanced reverse osmosis (VERO) membrane module under colloidal fouling for up to 12 hours of operation time. A porous cake mass transfer model for reverse osmosis (RO) colloidal fouling analysis was derived by combining the solute convection-diffusion model, cake filtration model, cake enhanced osmotic pressure (CEOP) effect, and the critical flux concept. The process of colloidal particle deposition and fouling accumulation on the membrane surface was visualized using this model. The local concentration dependent solute properties and variation of permeate flux and cake layer thickness over the membrane surface were predicted. Systematic studies including different initial permeate fluxes, Reynolds numbers, particle concentrations, and vibration frequencies were carried out to investigate the system performance under different operation conditions. The results suggest that colloidal fouling induced permeate flux decline could be improved by imposing vibration on the RO membrane. It was determined that the higher the vibration frequency, the higher the membrane permeate flux, while keeping the vibration amplitude constant. Model simulations were validated against experimental data of permeate fluxes with good agreement.

5.1. Introduction

Membrane fouling is considered to be a major challenge in seawater reverse osmosis (RO) membrane desalination. Fouling of RO membranes is typically caused by inorganic, colloidal, organic matters, and the development of biofilm on the membrane surface. Membrane fouling may lead to permeate flux decline, energy consumption growth, and short membrane lifetime [106]. Much effort has been devoted to the area of membrane system fouling control, especially for membrane colloidal fouling. This has focused on chemical treatment [41], feed solution pretreatment [40], and mechanical treatment including proposing high shear rate and shear stress on the membrane surface [42].

The investigations that take advantage of membrane vibration, all use torsional vibration to generate large shear rate at membrane surface. However, for the torsional vibration, points near the vibrating shaft will have much less vibration amplitude, which may inadequately utilize the vibration benefit for fouling control. A novel technique called vibration enhanced reverse osmosis (VERO) was proposed in our earlier work [82] aiming at improving membrane performance and permeate production. In this technique, a RO membrane desalination cell is driven by linear actuators to impose axial membrane vibration and large shear rate at membrane surface. Previous research successfully showed that this technique can enhance the permeate flux and mitigate the formation of inorganic fouling on the RO membrane surface [107]. Both Finite Element Method (FEM) and Computational Fluid Dynamics (CFD) simulations revealed that a lower concentration polarization (CP) modulus forms near the membrane surface with

vibration imposed, resulting in less fouling on the membrane surface with inorganic foulant.

The study reported here investigated the colloidal fouling growth and control in the VERO membrane system. A reverse osmosis membrane colloidal fouling model considering the cake enhanced osmotic pressure (CEOP) effect was proposed and combined with CFD simulations to predict the performance of a vibrating RO membrane under colloidal fouling. The effects of initial permeate fluxes, channel Reynolds numbers, inlet particle concentrations, and vibration frequencies are systematically investigated and presented for CFD simulations and experiments.

5.2. CFD simulation and Experimental Design

5.2.1. Fluid flow and boundary conditions

The hydrodynamics of the two-dimensional transient flow can be described by the following governing equations.

Continuity equation:

$$\frac{\partial \rho}{\partial t} + \frac{\partial (\rho u)}{\partial x} + \frac{\partial (\rho v)}{\partial y} = 0 \tag{57}$$

Momentum equations:

$$\frac{\partial(\rho u)}{\partial t}+\frac{\partial(\rho u^2)}{\partial x}+\frac{\partial(\rho uv)}{\partial y}=-\frac{\partial P}{\partial x}+\nabla\cdot(\mu\nabla u) \tag{58}$$

$$\frac{\partial(\rho v)}{\partial t}+\frac{\partial(\rho uv)}{\partial x}+\frac{\partial(\rho v^2)}{\partial y}=-\frac{\partial P}{\partial y}+\nabla\cdot(\mu\nabla v) \tag{59}$$

At the inlet (x = 0), the fully developed velocity profile and concentration profiles of the solutes are given as:

$$\begin{aligned} u &= 6\bar{u}\frac{y}{h}(1-\frac{y}{h}) \\ v &= 0 \\ c_n &= c_{n,b} \\ c_c &= c_{c,b} \end{aligned} \tag{60}$$

where $c_{n,b}$ and $c_{c,b}$ are the inlet bulk flow concentration of *NaCl* and silica colloidal particles, and $\bar{u}$ is the averaged crossflow velocity and is calculated with the corresponding channel Reynolds number.

At the outlet, the velocity and solute concentration gradients are assumed to be zero since the outlet boundary is far away from the membrane zone.

$$\begin{aligned} \frac{\partial c_n}{\partial x} &= 0 \\ \frac{\partial c_c}{\partial x} &= 0 \\ \frac{\partial u}{\partial x} &= 0 \end{aligned} \tag{61}$$

For top, non-membrane wall and feed spacers, the given vibration velocity and no solute flux boundary conditions are imposed:

$$\begin{aligned} u &= 2\pi f A \sin(2\pi f t) \\ v &= 0 \\ \frac{\partial c_n}{\partial \vec{n}} &= 0 \\ \frac{\partial c_c}{\partial \vec{n}} &= 0 \end{aligned} \tag{62}$$

where $\vec{n}$ is the unit normal vector at the wall boundary, A is the vibration peak amplitude, and f is the vibration frequency. In this investigation, A = 0.5 mm is applied in all vibration cases which results in the peak-to-peak amplitude = 1 mm. Four different vibration frequencies: 10 Hz, 20 Hz, 40 Hz, and 60 Hz were adopted to analyze the impact of membrane vibration.

For the bottom membrane boundary, the above mentioned vibration velocity is also applied and the permeate velocity, J, is specified. For both *NaCl* and silica particle solutes, the diffusive and convective fluxes must reach the balanced state:

$$
\begin{aligned}
u &= 2\pi f A \sin(2\pi f t) \\
v &= -J \\
D_n \frac{\partial c_n}{\partial y} &= -J c_n R_{n,\,rej} \\
D_c \frac{\partial c_c}{\partial y} &= -J c_c R_{c,\,rej}
\end{aligned}
\tag{63}
$$

where J is the membrane local permeate flux, $R_{n,rej}$ and $R_{c,rej}$ are the membrane intrinsic rejection coefficients for *NaCl* and silica colloidal particles and are assumed to be 0.98 and 1 respectively.

5.2.2. Numerical implementation and modeling of fouling layer evolution

The computational geometry and numerical implementation method analyzed in section 4.3. were also adopted in this study. Figure 40 illustrates the calculation algorithm used to model the above mentioned colloidal fouling layer evolution process in a VERO desalination module. Fluent (Ansys Inc., Canonsburg, PA) was utilized as the CFD solver to perform numerical simulations. Batch process subroutines and User Defined Function (UDF) were created to simulate the fouling layer evolution process, determine cell fouling status, calculate cell particle deposition rate, and change the type of cell from fluid cell to porous media cell when necessary.

There are two time loops inside flow diagram shown in Figure 40. The first one is the vibration time used in equation (62), and this time loop is marked blue in Figure 40. The length of one complete sinusoidal vibration cycle varies from 1/60 s to 1/10 s depending on the value of vibration frequency. Each sinusoidal vibration cycle is divided

by several time steps $\Delta t'$ to capture the effect of the boundary vibration on the fluid hydrodynamics and fouling rate. The value of the particle deposition rate S_c can be calculated for each time step. Since the length of a vibration cycle (varies from 1/60 s to 1/10 s) is too small compared with the length of the entire operation time (12 h), the profiles of cake distribution and the cell porosities do not change during the vibration time loop.

The second time loop is the fouling deposition time loop which is marked green in Figure 40. The deposition time step Δt is combined with the time averaged deposition rate $\overline{S_c}$ in equation (39) to calculate the deposition mass in the fluid-cake interface cell. This deposition time step Δt should be small enough to capture this gradual change process of the cell porosity and to make the simplification acceptably accurate. Depending on the value of $\overline{S_c}$, the values of deposition time step Δt varying from 0.1 mins to 30 mins were picked to make sure the fouling layer thickness change is not significant compared with the height of the cell within the given deposition time step.

The simulation begins with a clean membrane channel without silica colloidal particle deposition and all cells are defined as the fluid domain. The vibration velocity is updated using the corresponding vibration time by equation (62). Then, fluid properties, diffusion coefficients and parameters of the cake filtration model are updated and inserted in FLUENT to solve the governing equations in both the fluid and porous media domains, if applicable. Once the converged flow and solute concentration fields are calculated the deposition rate S_c for the vibration time is obtained and recorded. If the

total vibration time is less than the length of one vibration cycle, the vibration time will be updated and the vibration time loop will be repeated; otherwise, the time averaged deposition rate $\overline{S_c}$ will be calculated by averaging all values of the deposition rate S_c during the current vibration cycle. This time averaged deposition rate $\overline{S_c}$ will be combined with time step Δt of the particle deposition time loop to calculate the particle deposition mass at the fluid-cake interface. The cell with fouling deposition will be treated as a porous media and its new porosity can be calculated by equation (55). Once the cell porosity reaches the value of ε_{min}, this cell will be treated as a 'fully deposited cake cell', and the cell above this one will be treated as the new interface cell, and converted externally from a fluid cell to a porous media cell. This updated computational geometry will be updated in FLUENT for the next deposition time step. This fouling deposition time loop will be repeated until the calculation time reaches the pre-set calculation time limit, which is 12 hours in this investigation.

5.2.3 Experimental Design

The same experimental system used in Chapter 3 and Chapter 4 was also adopted here. Figure 2 presents the diagram of the cross flow RO membrane desalination cell. And Figure 4 shows the schematic diagram of the vibration enhanced reverse osmosis membrane system set-up. For all vibration cases, peak-to-peak vibration amplitude is fixed at 1 mm while vibration frequencies are 10 Hz, 20 Hz, 40 Hz, and 60 Hz.

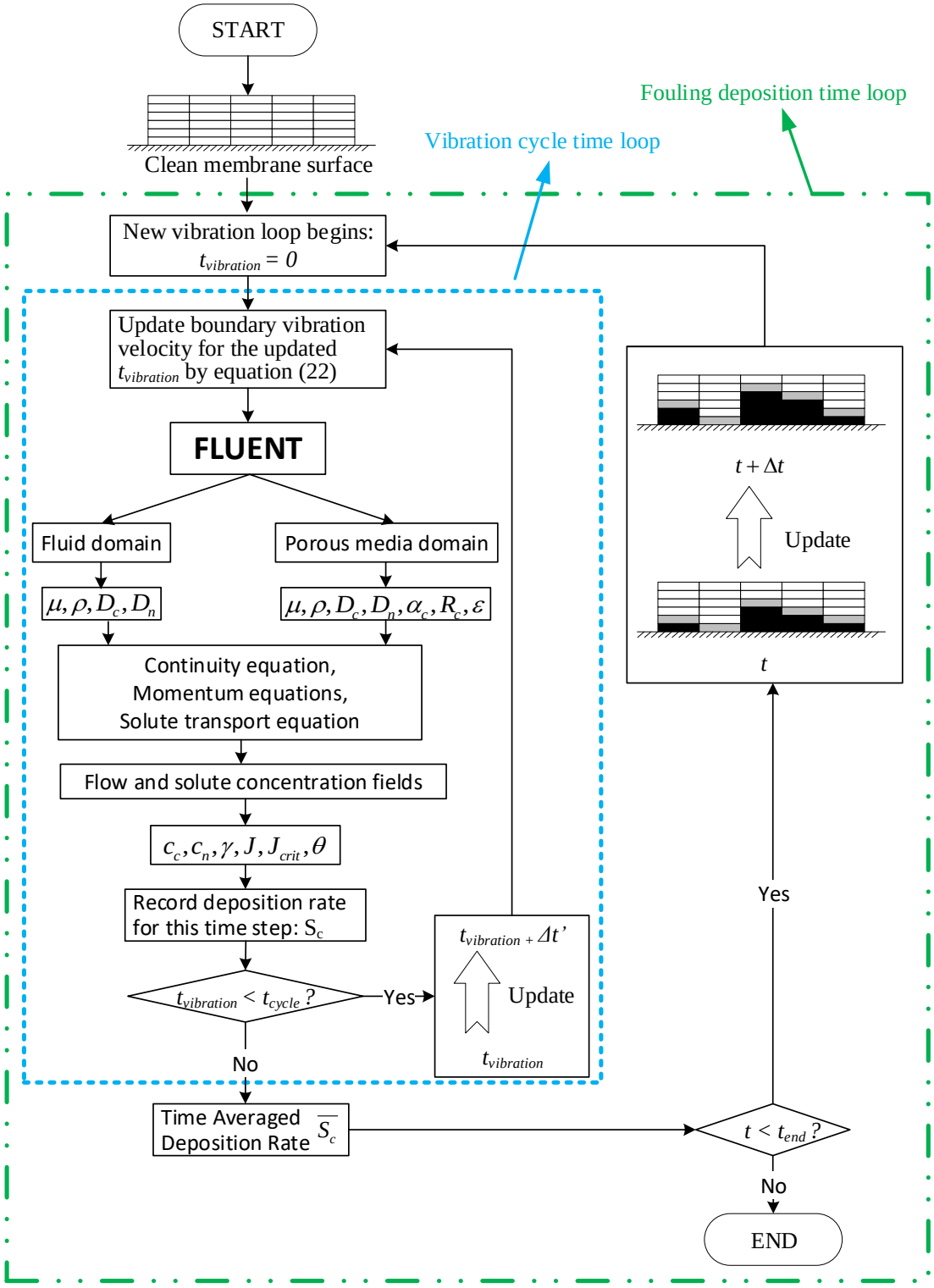

Figure 40. Scheme of fouling calculation algorithm.

5.3. Results and discussion

Several important factors influencing colloidal fouling in membrane desalination systems are investigated. Specifically feed colloidal concentrations, channel Re numbers, initial permeate fluxes, and membrane vibration frequencies are considered. The membrane vibration frequency study demonstrates the effectiveness of membrane vibration on colloidal fouling control. All simulations and experiments were performed for 12 hours.

Table 9 summarizes key parameters varied in the CFD simulation study. The table includes 7 sets of parameter values, with each set also including 5 cases which are defined by vibration frequency. The parameter “initial permeate flux” is the value of the permeate flux of the membrane module at the beginning of the fouling test (no initial fouling). Set 1 is the benchmark case, while the differences of simulation conditions between the other six case sets with set 1 are bolded. Five different vibration frequency cases are included with a constant peak-to-peak vibration amplitude of 1 mm, for all 7 parameter sets: 0 Hz, 10 Hz, 20 Hz, 40 Hz, and 60 Hz. Experiments were performed in some cases to validate the simulation results from the aspect of membrane permeate flux. All simulations and experiments were performed for a 12 hour total period.

Table 9. Summary of conditions for different parameter sets and frequency cases.

Case Set #	Inlet silica colloidal concentration (ppm)	Initial flux J_0 (μm/s)	Inlet Re	frequency (Hz)	amplitude (mm)	Section
1	400	14	400	0, 10, 20, 40, 60	1	Benchmark
2	**200**	14	400	0, 10, 20, 40, 60	1	Colloidal silica particle concentration
3	**800**	14	400	0, 10, 20, 40, 60	1	
4	400	14	**200**	0, 10, 20, 40, 60	1	Reynolds number
5	400	14	**600**	0, 10, 20, 40, 60	1	
6	400	**10**	400	0, 10, 20, 40, 60	1	Initial permeate flux
7	400	**18**	400	0, 10, 20, 40, 60	1	

Two non-dimensional parameters are used in this section to analyze the performance of the membrane under colloidal fouling conditions. The first is the membrane *NaCl* CP modulus at time *t*, with *f Hz* vibration in each case:

$$\Gamma_{t,fHz} = c_{n,m} / c_{n,b} \tag{64}$$

The averaged *NaCl* concentrations at the membrane surface and in the bulk flow are used to calculate the value of the CP modulus. In order to analyze the benefit of the membrane vibration on the CP phenomenon, a percent of *NaCl* accumulation reduction at time *t* caused by the *f Hz* vibration is defined as:

$$\Delta\Gamma_{t,fHz}\% = \left(\frac{\Gamma_{t,0Hz} - \Gamma_{t,fHz}}{\Gamma_{t,0Hz} - 1} \right) \times 100\% \tag{65}$$

The second non-dimensional parameter is the normalized membrane permeate flux. In order to show the percent of flux decline caused by the colloidal fouling and compare sets with different initial permeate fluxes, a normalized permeate flux is adopted instead of the actual value of permeate flux. Permeate flux at time *t* under the influence of *f Hz* vibration, $J_{t,fHz}$, is divided by the initial permeate flux (no fouling occurs at $t = 0$) of the corresponding no-vibration cases, $J_{0,0Hz}$, to get the normalized permeate flux:

$$\hat{J}_{t,fHz} = J_{t,fHz} / J_{0,0Hz} \tag{66}$$

5.3.1. Silica colloidal fouling and fouling layer growth visualization

The no-vibration case and the 60 Hz vibration case in the benchmark parameter set (set 1 in Table 9) are selected to investigate silica colloidal fouling inside the VERO membrane module. The fouling layer growths with time near the feed spacer (white circles) in the 9th unit element are illustrated in Figure 41 (left: no-vibration case, right: 60 Hz vibration case). Considering the highly transient velocity profile in the 60 Hz vibration case, only the streamlines for the no-vibration case are presented in this figure. Porous cakes are shown in black next to the membrane surface.

No porous cake appears in the feed channel at the beginning of the desalination process simulation. Four obvious porous cakes, marked 1-4, can be found in the no-vibration case after 3 hours. The positions of cake 1 and cake 2 are the stagnation points of the recirculation vortex that is formed near the upstream face of the feed spacer. Similarly, cake 3 and cake 4 are located at the stagnation points of the recirculation vortex near the downstream face of the feed spacer. Particle concentrations are relatively high in these areas while the shear rate values are low. These areas are expected to have more particle deposition according to the particle deposition rate S_c expression in equation (44), which agrees with the CFD simulation results. The size of all four cakes become much larger after 12 hours, for the no-vibration case. Cake 1 and cake 2 are connected together and grow into one large cake due to the low vorticity of the upstream vortex. Besides these obvious porous cakes, thin porous layers can also be found in other membrane surface areas.

For the 60 Hz vibration case, a thin porous layer can be found after 3 hours and a thicker porous layer can be found after 12 hours. Obvious cakes next to the feed spacer are not observed. It is interesting to see that the variation of the cake layer height along the membrane surface is small, which is very different than the no-vibration case. This difference shows that the colloidal particle deposition rate S_c does not change much along the membrane surface in the with vibration cases. Membrane vibration greatly changes the hydrodynamics near the membrane surface and reduces the influence of the feed spacer on the particle deposition.

In sum, colloidal porous cakes grow in both membrane coverage and cake height with increase in time for the no-vibration cases. Large colloidal porous cakes form next to feed spacers and at the stagnation points of vortices. For the 60 Hz vibration cases, a thin cake layer appears on the membrane surface and grows with time. This is in contrast with the formation of large colloidal porous cakes without vibration. Particle accumulation near the feed spacer is clearly reduced by membrane vibration.

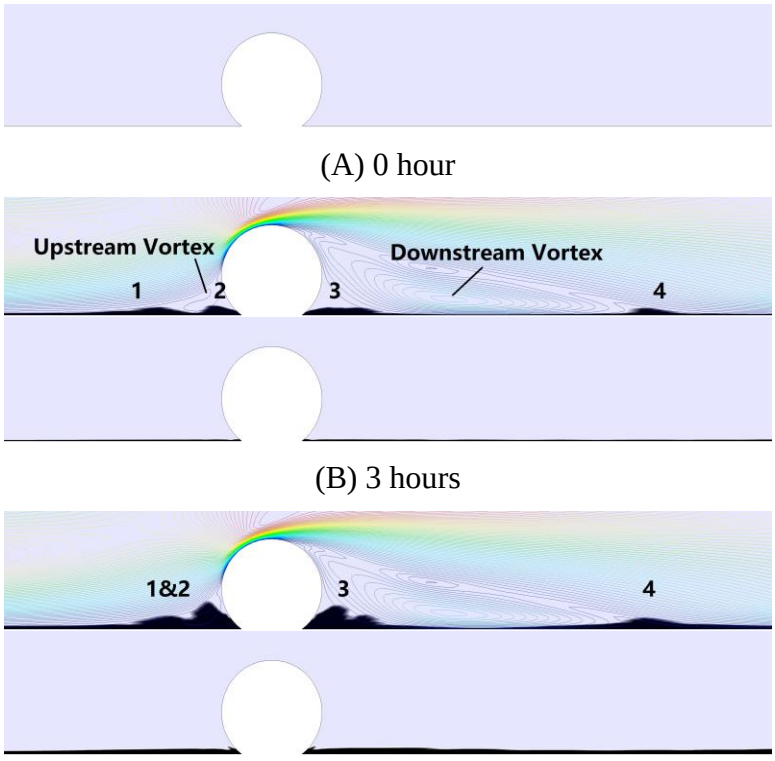

(A) 0 hour

(B) 3 hours

(C) 12 hours

Figure 41. Development of porous cake layer growth near the membrane and colored streamlines (for the no-vibration case) for the (top) no-vibration case and (bottom) 60 Hz vibration case at the end of (A) 0 hours, (B) 3 hours and (C) 12 hours. The porous cake is shown in black and the bulk flow direction is from left to right.

The effect of porous cake on NaCl diffusion and the CEOP effect are clearly presented in Figure 42. *NaCl* concentration profiles at location x = 51.7 mm with different vibration conditions (no-vibration and 60 Hz vibration) and membrane types (initial clean and fouled membranes) are shown in the figure. The chosen location (x = 51.7 mm) is in the downstream area of the 9^{th} spacer from the channel inlet. There are three flow areas in this figure: porous cake area near the membrane surface, recirculation area in the downstream area of the feed spacer, and the bulk flow area.

A smooth *NaCl* concentration increase is found near the membrane surface in the clean membrane cases, which is consistent with the well-known concentration polarization phenomenon caused by membrane rejection of *NaCl* solute. The *NaCl* concentration increase near the membrane surface in the fouled membrane cases are much sharper compared with the corresponding clean membrane cases, resulting in more severe concentration polarization phenomenon in the fouled membrane cases. The CP modulus values of the fouled membrane cases are higher than the corresponding clean membrane cases under the same vibration conditions. The CEOP phenomenon, as caused by colloidal porous cakes, hinders the solute mass transportation and increases *NaCl* concentration near the membrane surface.

The *NaCl* membrane CP modulus with the 60 Hz vibration, clean membrane case is around 1.18, which is much lower than the 1.55 in the no-vibration, clean membrane case. Similarly, membrane vibration also improves the CP phenomenon in fouled membrane cases by reducing the CP modulus from 1.75 to 1.38. These CP modulus value drops show the effects of membrane vibration on reducing the CP modulus and the

membrane colloidal fouling. The decreased *NaCl* concentration next to the membrane surface reduces the corresponding transmembrane osmotic pressure of *NaCl* and thus reduces the operation pressure required to produce the same amount of permeate flux.

The *NaCl* CP modulus for fouled membrane cases are slightly lower than the corresponding clean membrane cases in the recirculation area, since the solute back-diffusion to the bulk flow is limited by the porous cake in the fouled membrane cases. In the bulk flow area, the local *NaCl* concentrations are equal to the inlet concentration in all four cases.

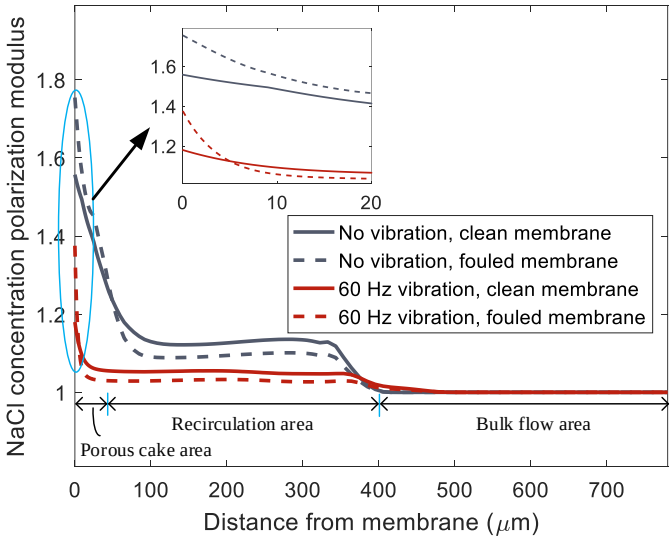

Figure 42. Comparison of the cross stream NaCl concentration polarization modulus profile for clean and fouled membranes in different vibration conditions at the downstream area (x = 51.7 mm) of the 9th spacer from the channel inlet.

5.3.2. Effect of membrane vibration in the benchmark case set

Figure 43 and Figure 44 show the *NaCl* CP modulus and normalized permeate flux variations with time for the benchmark set (set 1 in Table 9). The CP modulus initially increases rapidly, then increases slowly with time for all cases. The normalized permeate fluxes initially reduce rapidly, then reduce slowly with time for all cases. The initial normalized permeate fluxes for the four vibration cases are higher than 1, which is the value of the initial normalized permeate flux of the no-vibration case. The CP modulus decreases monotonically and the normalized permeate flux increases monotonically with increasing vibration frequency for all times. The simulation results indicate that applying membrane vibration improves the membrane performance and CP phenomenon in the benchmark colloidal fouling tests, for up to 12 hours operation. For instance, after 12 hours, 30% more permeate flux and 22% reduction of the *NaCl* accumulation are observed comparing the no-vibration case and the 60 Hz vibration case. High membrane vibration frequency induces high shear rates at the membrane surface, which enhances the back transport of solutes to the bulk flow, and reduces the colloidal particle deposition rate.

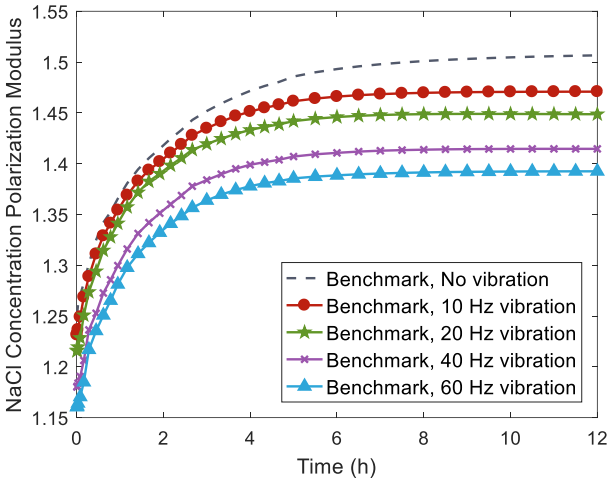

Figure 43. NaCl concentration polarization modulus vs. time for the benchmark set with feed *NaCl* concentration = 32,000 ppm, feed colloidal particle concentration = 400 ppm, Re = 400 and initial permeate flux = 14 μm/s.

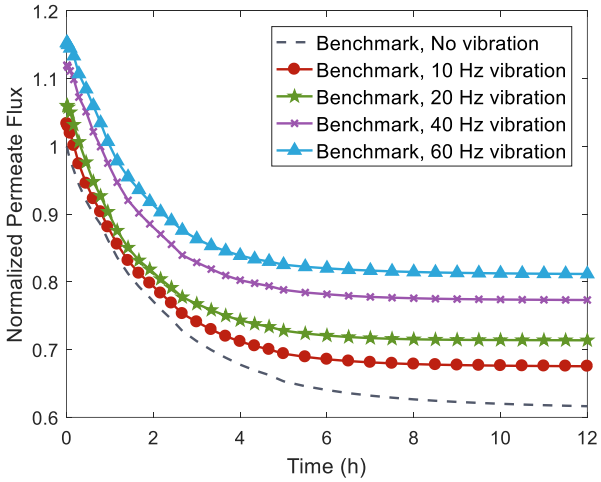

Figure 44. Normalized permeate flux vs. operation time for the benchmark case set with feed *NaCl* concentration = 32,000 ppm, feed colloidal particle concentration = 400 ppm, Re = 400 and initial permeate flux = 14 μm/s.

5.3.3. Effect of membrane vibration in cases with different silica colloidal particle concentrations

Sets 1, 2 and 3 (Table 9) are analyzed in this section to determine the effects of inlet silica colloidal particle concentration on membrane performance. Figure 45 and Figure 46 show the change in *NaCl* CP modulus and normalized permeate flux vs. time for the set 2 (200 ppm inlet silica particle concentration) and the set 3 (800 ppm inlet silica particle concentration). The inlet concentration of silica colloidal particle can be controlled or reduced by microfiltration or ultrafiltration pretreatments in commercial desalination plants.

Reducing the silica colloidal particle concentration reduces the *NaCl* CP modulus and increases the normalized permeate flux. For example, after 12 hours the *NaCl* CP modulus in the 800 ppm, no-vibration case is 1.51, which is higher than the 1.48 value in the 200 ppm, no-vibration case. Similarly, the normalized permeate flux in the 800 ppm, no-vibration case is 0.61 while the normalized permeate flux in 200 ppm, no-vibration case is 0.65. The *NaCl* CP modulus decreases monotonically and the normalized permeate flux increases monotonically with increasing vibration frequency for all times. At t = 12 hours, 26% more permeate flux and 21% reduction of the *NaCl* accumulation can be found when comparing the 200 ppm set with no-vibration and with 60 Hz imposed vibration.

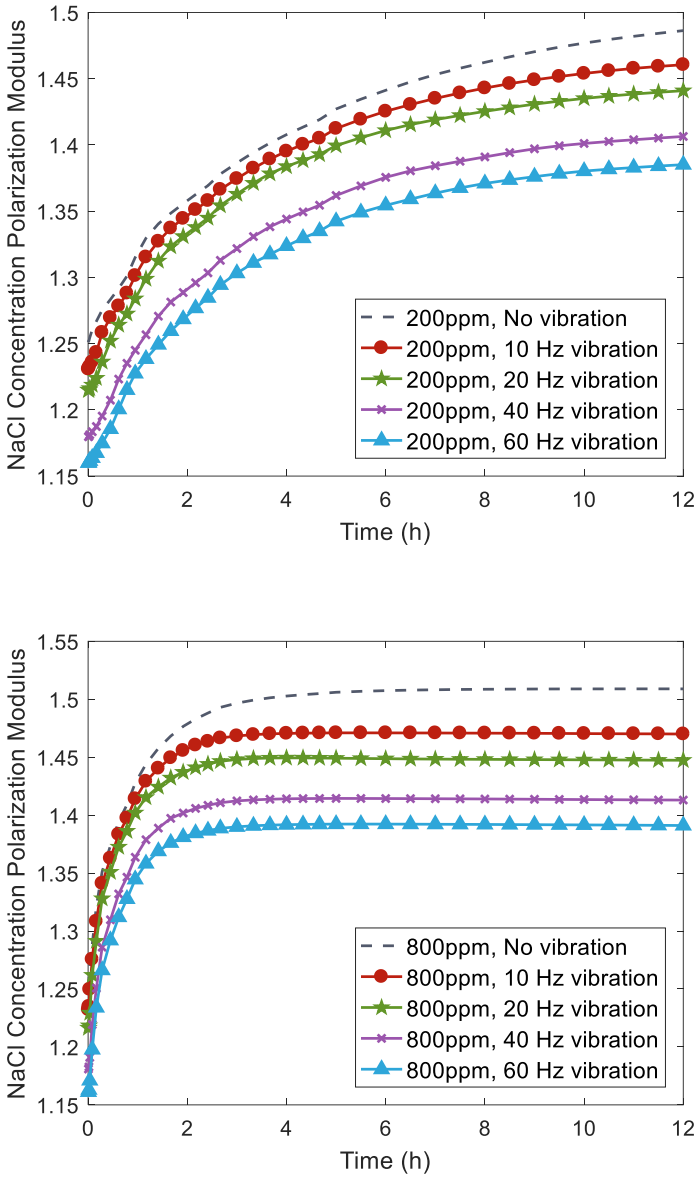

Figure 45. *NaCl* concentration polarization modulus vs. time for different inlet silica colloidal particle concentration, top: 200 ppm silica particle; bottom: 800 ppm silica particle.

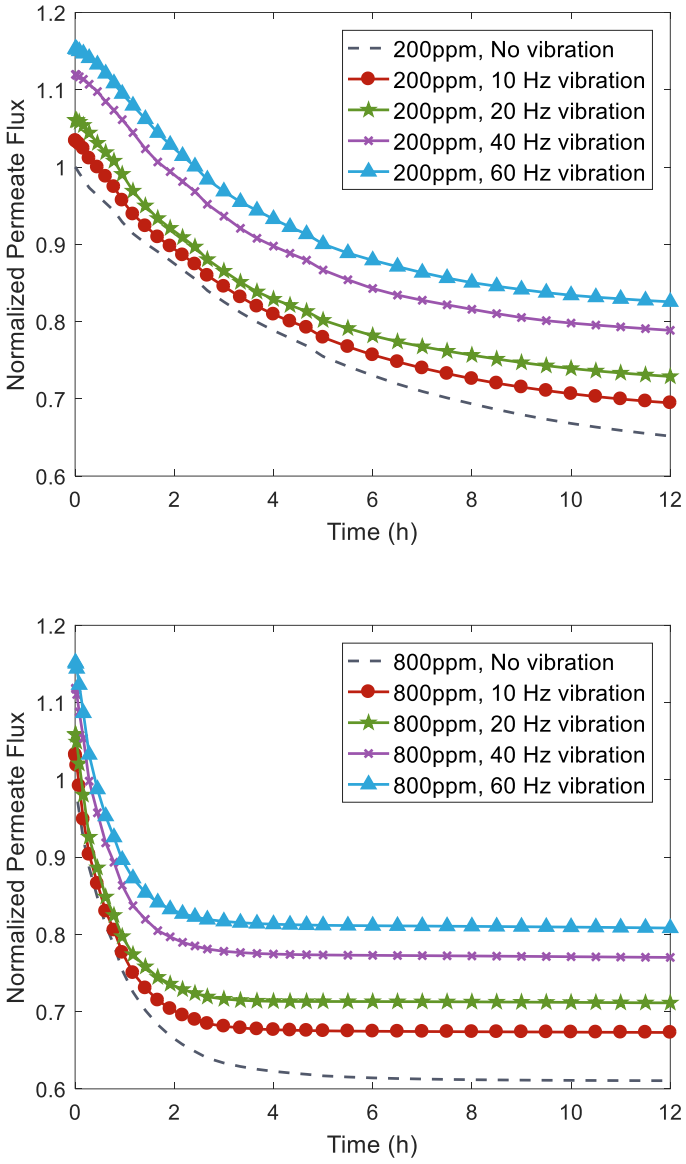

Figure 46. Normalized permeate flux vs. time for different inlet silica colloidal particle concentration, top: 200 ppm silica particle; bottom: 800 ppm silica particle.

5.3.4. Effect of membrane vibration in cases with different channel Reynolds numbers

Sets 1, 4 and 5 (Table 9) are discussed in this section in order to investigate membrane performance when changing the channel Reynolds number. Figure 47 and Figure 48 show the variation in *NaCl* CP modulus and normalized permeate flux vs. time for the set 4 (Re = 200) and the set 5 (Re = 600). The Reynolds number of the feed channel can be controlled by varying the feed pump flow rate in commercial desalination plant.

From Figure 47, it is clear to see, under the same vibration condition and operation time, the set with higher channel Reynolds number has lower value of the *NaCl* CP modulus. High channel Reynolds number induces high crossflow velocity and high shear rate near the membrane surface, which enhances the local particle mass transportation. Colloidal particles are less able to accumulate and deposit on the membrane surface in sets with higher Reynolds number. After 12 hours, the highest salt accumulation is found in the Re = 200, no-vibration case among all 7 sets considered. It should be noticed that, since the pressure applied in the cases with Re =200 is much higher than the cases with Re = 600 to obtain the same level of initial permeate flux (J_0 = 14 $\mu m/s$), the normalized permeate flux in the cases with Re = 200 maybe higher than the corresponding cases with Re = 600 even with higher *NaCl* CP modulus.

Membrane vibration benefits membrane performance for all three different Reynolds numbers, and increasing vibration frequency yields higher normalized permeate flux and lower *NaCl* CP modulus. The benefit of membrane vibration on membrane performance varies significantly with inlet channel Reynolds numbers. This

differs from the trend shown in Figure 45 and Figure 46, which demonstrated an almost invariance with different inlet silica colloidal particle concentrations. Table 10 summarizes the membrane performance in sets with different Reynolds numbers and vibration frequencies at t = 12 hours. Both percent reduction of *NaCl* accumulation and percent increase of the normalized permeate flux due to the membrane vibration, reduce with increasing inlet channel Reynolds number.

The membrane vibration increases the shear rate near the membrane surface, which in the set of high inlet Reynolds number is already high. Thus, the benefit of membrane vibration in increasing shear rate decreases with higher Reynolds numbers. Even lower membrane performance improvement due to membrane vibration can be expected for sets with Reynolds numbers higher than 600. It should be noted that, when the vibration frequency is 60 Hz, the difference of CP modulus between sets with Re = 400 and Re = 600 is very small (1.3924 vs. 1.3833). This suggests that, for membrane applications with Reynolds number higher than 400, it is not recommended to utilize membrane vibration considering the cost of implementing membrane vibration.

In contrast, varying the inlet particle concentration does not affect the shear rate near the membrane surface. As the result, the benefit of the membrane vibration for sets with different inlet silica colloidal particle concentrations do not vary much, which can be seen in Figure 45 and Figure 46.

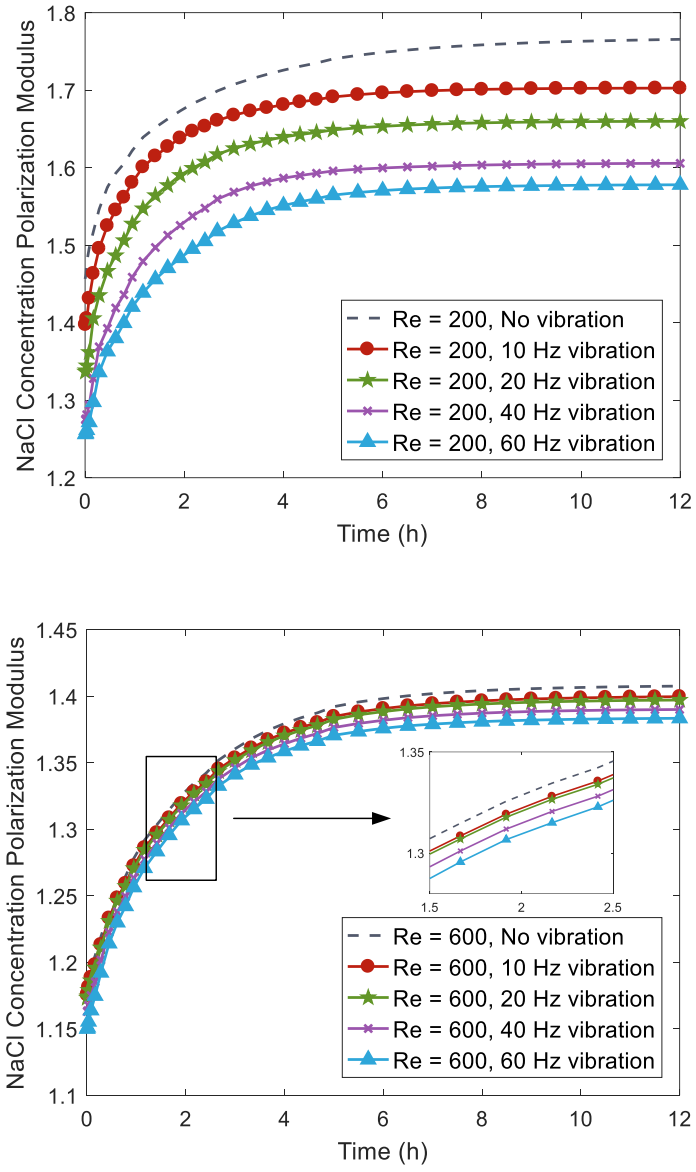

Figure 47. Change in *NaCl* concentration polarization modulus with operation time for different vibration frequencies, top: Re = 200; bottom: Re = 600.

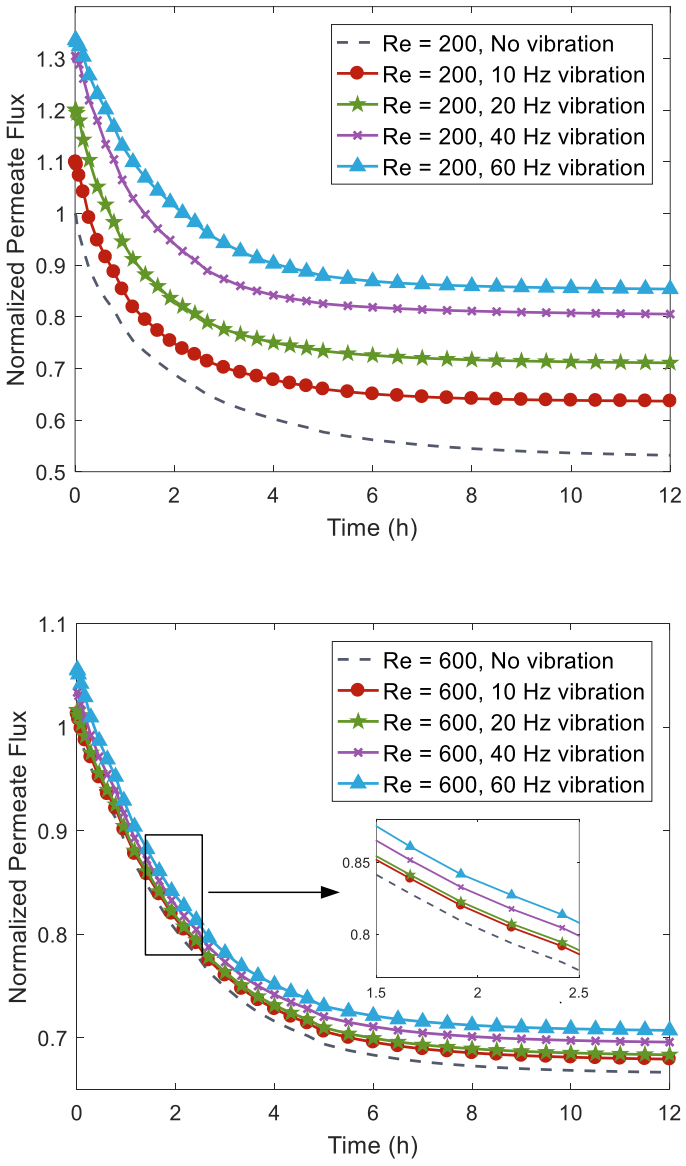

Figure 48. Change in normalized permeate flux with operation time for different vibration frequencies, top: Re = 200; bottom: Re = 600.

Table 10. Summary of membrane performance in cases with different Reynolds numbers and vibration frequencies when t = 12 hours.

		Re = 200	Re = 400	Re = 600
CP modulus	No vibration	1.7656	1.5066	1.4075
	60 Hz vibration	1.5779	1.3924	1.3833
percent reduction of the *NaCl* accumulation caused by 60 Hz vibration		24.52%	22.54%	5.94%
Normalized permeate flux	No vibration	0.5318	0.6164	0.6664
	60 Hz vibration	0.8535	0.8117	0.7070
percent increment of the normalized permeate flux caused by 60 Hz vibration		60.49%	31.68%	6.09%

5.3.5. Effect of membrane vibration in cases with different initial permeate fluxes

Sets 1, 6 and 7 (Table 9) are analyzed in this section to investigate the benefit of membrane vibration on the membrane performance with different initial permeate fluxes. Figure 49 and Figure 50 show the changes in *NaCl* CP modulus and normalized permeate flux vs. time for set 6 (J_0 = 10 $\mu m/s$) and set 7 (J_0 = 18 $\mu m/s$). The initial permeate flux may be controlled by varying the operating pressure of the feed pump in commercial desalination processes.

The set with a higher initial permeate flux has higher *NaCl* CP modulus and lower normalized permeate flux, under the same vibration conditions and operation time. For example, after 12 hours, the values of *NaCl* CP modulus in the no-vibration cases with J_0 = 10 $\mu m/s$ and J_0 = 18 $\mu m/s$ are 1.33 and 1.70, respectively. Similarly, when t = 12 hours, the normalized permeate flux in the J_0 = 10 $\mu m/s$, no-vibration case is 0.66 while the normalized permeate flux in the J_0 = 18 $\mu m/s$, no-vibration case is 0.58. This phenomenon can be explained from two separate perspectives. First, the membrane permeate flux accelerates the accumulation of *NaCl* on the membrane surface. Figure 49 shows that higher values of *NaCl* CP modulus occur in J_0 = 18 μm set, for the initial (t = 0) clean membrane. Secondly, the drag force created by the membrane permeate flux is also the primary driving force for silica particles to accumulate on the membrane surface. Increased initial permeate flux induces a larger net flux ($J - J_{crit}$) and a larger particle deposition rate S_c in equation (44). The formation and growth of colloidal fouling cakes will increase the hydraulic resistance R_c and result in the CEOP effect, which intensifies the accumulation of *NaCl* near the membrane surface. These

two reasons explain the greater flux decline rate and more *NaCl* accumulation in the set with higher initial permeate flux.

It is important to note that, although the normalized permeate flux for the case with J_0 = 18 μm/s is relatively low, considering the high actual value of the initial permeate flux, the absolute value of the permeate flux may be even higher than the other two cases. For example, after 12 hours, the relative permeate flux and the actual permeate flux for the J_0 = 18 μm/s, 10 Hz case are 0.65 and 11.7 μm/s. For the J_0 = 10 μm/s, 10 Hz case, they are 0.71 and 7.1 μm/s respectively.

Similar to the previous sections, membrane vibration contributes to improving the membrane performance for all three sets with different initial permeate fluxes. For instance, after 12 hours, 30% more permeate flux and 22% reduction of the *NaCl* accumulation are observed comparing the no-vibration case and the 60 Hz vibration case.

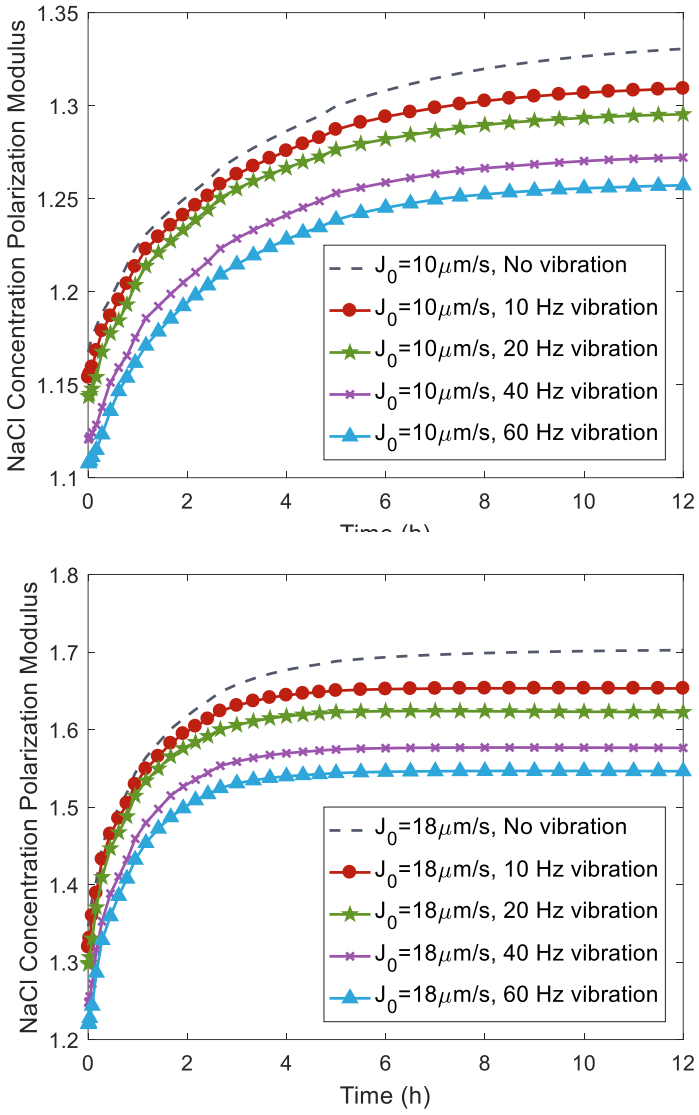

Figure 49. *NaCl* concentration polarization modulus vs. time for different initial permeate flux cases, left: J_0 = 10 μm/s; right: J_0 = 18 μm/s.

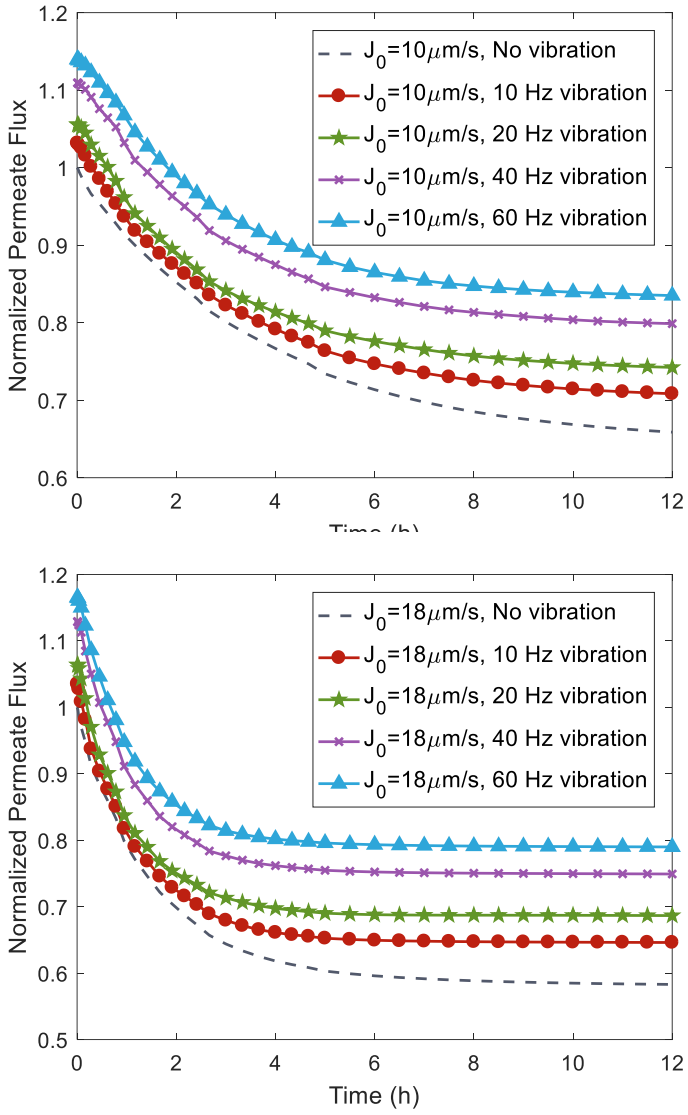

Figure 50. Normalized permeate flux vs. time for different initial permeate flux cases, left: J_0 = 10 μm/s; right: J_0 = 18 μm/s.

5.3.6. Experimental validation

Experiments were performed for several parameter sets in order to validate the CFD model results. Permeate flux was measured and compared with the corresponding simulation cases as shown in Figure 51. There is generally good agreement between the predicted and measured permeate flux variation with time. The differences can be attributed to the approximate cake layer model developed above, the assumption of constant porosity of the fully deposited cake, uncertainty in parameters, and experimental measurement error.

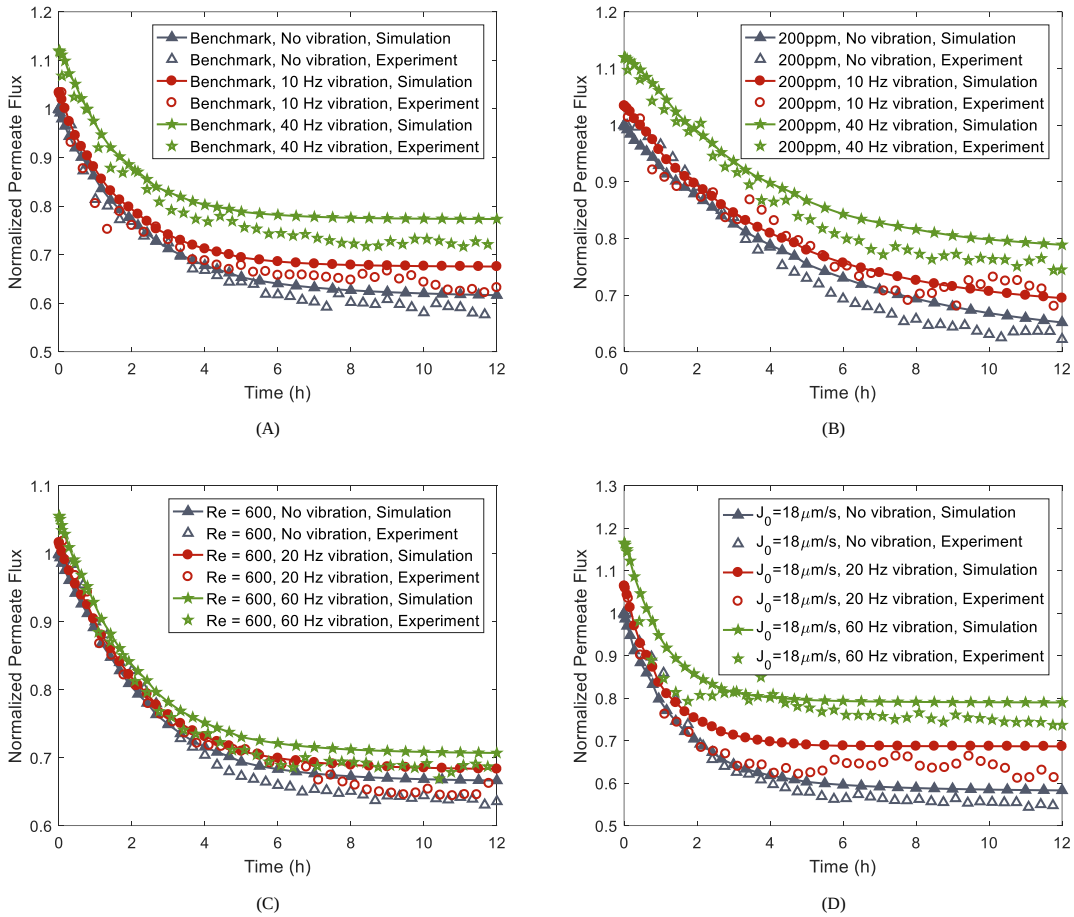

Figure 51. Experimental validation results for normalized permeate flux vs. time for different working conditions. (A) Benchmark cases. (B) Cases with $c_{c,b}$ = 200 ppm. (C) Cases with Re = 600. (D) Cases with J_0 = 18 μm/s.

5.4. Conclusions

The colloidal fouling control performance of a vibration enhanced reverse osmosis (VERO) approach was investigated utilizing Computational Fluid Dynamic (CFD) simulations and experiments for up to 12 hours. The experimental setup used linear motors to impart sinusoidal motion to the membrane in order to increase the membrane surface shear rate. This was shown to reduce membrane concentration polarization (CP) and permeate flux decline caused by colloidal fouling. The VERO module was investigated with different desalination system operation parameters including initial permeate flux, inlet Reynolds number, feed solution silica particle concentration and membrane vibration frequency, to show the wide applicability of the technique in colloidal fouling control.

A cell-based colloidal particle deposition and fouling growth model was proposed and numerically implemented in the CFD simulation to obtain detailed fouling cake distributions, flow patterns, and salt concentration distributions. The model includes concentration dependent fluid properties, axial variation of permeate flux and cake height, cake enhanced osmotic pressure (CEOP) effect, and critical flux theory. The model simulations are validated by comparison with experimentally measured permeate fluxes.

The CFD simulations and corresponding experimental results show that colloidal fouling has a significant influence on membrane performance with up to a 47% decline in permeate flux and a 1.77 *NaCl* CP modulus after 12 hours of operation. The results

also show that membrane performance can be improved by the VERO module for all 7 system parameter sets shown in Table 9. Membrane *NaCl* CP modulus decreases and permeate flux under the influence of colloidal fouling increases as the vibration frequency increases (up to 60 Hz), with a constant peak-to-peak vibration amplitude of 1 mm. Comparison of the 60 Hz vibration and no-vibration cases, in the parameter set with Re = 200, demonstrated a maximum 60% improvement of the normalized permeate flux and a 25% reduction in *NaCl* accumulation, after 12 hours of operation. The improvement is less in sets with high Reynolds number (Re = 600), since the shear rates near the membrane surface are already very high.

Future studies may involve the implementation of VERO approach on an industrial scale system. Objectives will include energy usage and capital cost minimization for the shaking force actuation system, while balancing permeate flowrate improvement level with initial and operating cost. Additional experimental and simulation investigations of the VERO approach can also be conducted to mitigate other types of fouling, such as organic fouling and biofouling.

6. CONCEPT AND ENERGY CONSUMPTION ESTIMATION OF A NEW CENTRIFUGAL REVERSE OSMOSIS DEVICE

6.1. Introduction

A new desalination technology called centrifugal reverse osmosis (CRO) was proposed by Carl Grenci [108] and developed by Peter Wild and Goeffrey Vickers [109–112]. Investigations showed that this CRO technology offers significant benefits relative to the conventional reverse osmosis [113].

CRO is similar to conventional reverse osmosis in that both processes are based on high-pressure membrane separation. However, a fundamental difference between the processes is the means by which the high pressure is developed. In conventional reverse osmosis, a high pressure feed pump is required, whereas in CRO the high pressure is developed within a centrifuge rotor. A key advantage of the new desalination technology CRO includes elimination of the high pressure feed pumps, and hence eliminating the wasted energy associated with high pressure brine exhaust, that presents in conventional RO desalination processes. It has been known for some time that the benefits of centrifugal seawater reverse osmosis desalination are potentially great.

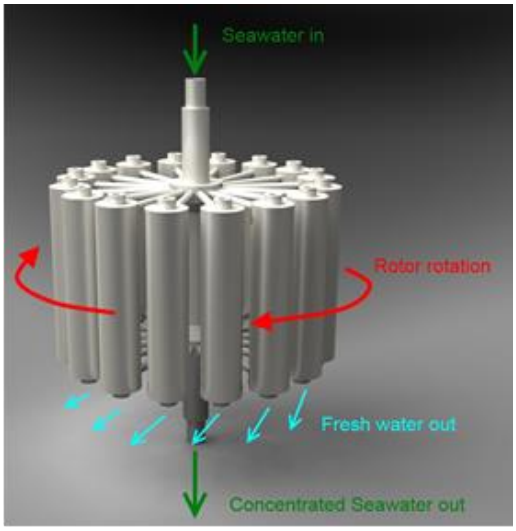

(a)

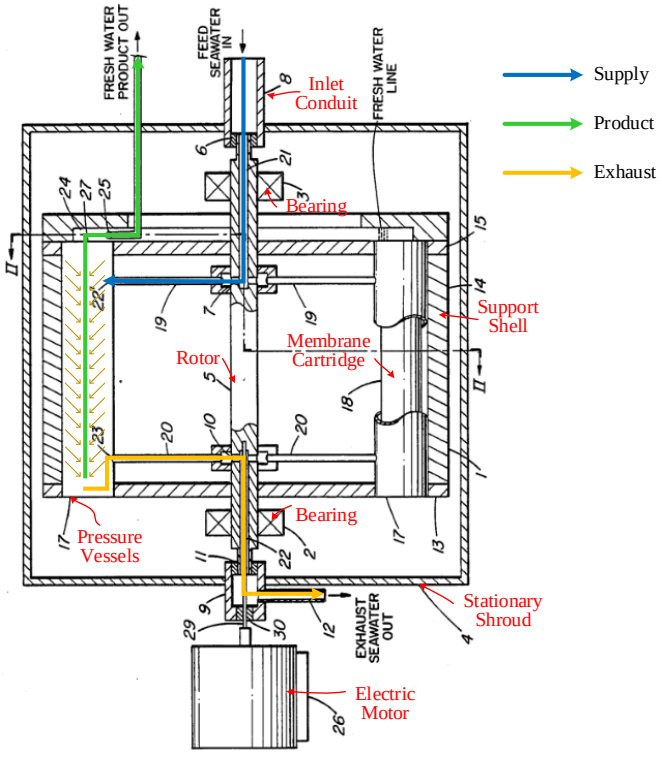

(b)

Figure 52. Schematic diagram of a centrifugal reverse osmosis desalination plant. (a) 3D modeling. (b) Cut plane and flow path.

Currently the main design concepts about the CRO device is proposed by Vickers etc. in 2000 [111], as shown in Figure 52. In this design, several commercial RO cartridges were placed around the rotor as a ‘Gatling gun’. The low pressure feed water enters the rotor axis, and pressurized by the centrifugal force through the radial passages (19 in Figure 52(b)), then flows into the RO cartridges. Rotor speed and radius are chosen so that the pressure inside the RO cartridges meets the desalination requirements. Inside the RO cartridges, permeate water is produced and transported outside the CRO device. The remaining high pressure brine solution is de-pressurized and returns to the rotor axis. In this process, the system works as a turbine to drive the rotor spinning. Finally, the low pressure brine solution exits the rotor. The potential benefits of CRO device is summarized in Table 11 [109].

In this study, a new CRO device was proposed to reduce the energy consumption and device size.

6.2. Comparison between the new CRO design with Vickers’ design

In Vickers’ design and designs from other peers, membrane cartridges in Gatling gun design are used for the CRO device. The configuration of membrane cartridges can be seen in the left sub-figure of Figure 53. It is clear to find that gaps between cartridges are not been properly used, which results in low space utilization ratio of the CRO device.

Table 11. The potential benefits of centrifugal RO [109].

	Conventional RO	Centrifugal RO
Energy Consumption	1. Pressure energy of exhaust brine is wasted. 2. Additional capital cost and complexity of energy recovery turbine justified only for very large systems.	Recovery of pressure energy of exhaust brine is an inherent feature of centrifugal reverse osmosis.
Reliability	1. High-pressure pump often a source of breakdown, particularly dynamic high-pressure seals. 2. High-pressure piping requires exotic alloys to minimize corrosion.	1. Simple design having only a single moving part. 2. No dynamic high-pressure seals. 3. Non-metallic construction, hence no corrosion problems.
Initial and replacement membrane costs	1. Operate at high recovery ratio in order to minimize power consumption. 2. High recovery ratio requires more initial membranes and reduces membrane life.	1. Operate at low recovery ratio as energy consumption is independent of recovery ratio. 2. Low recovery ratio requires fewer initial membranes and replacement is less frequent.

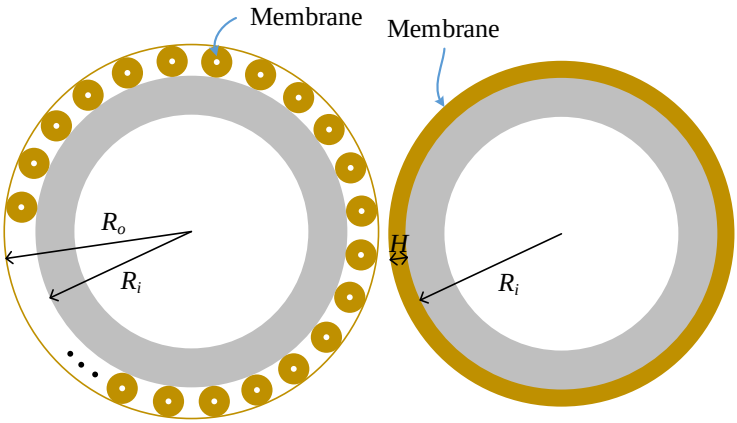

(a) Cut plane

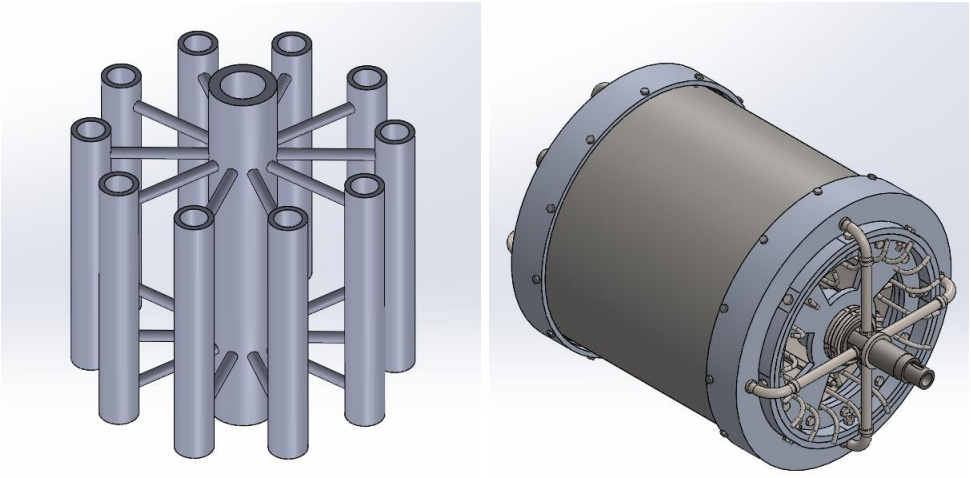

(b) 3D modeling

Figure 53. Vickers' design (left) and our new CRO design (right).

In this study, a new CRO design called 'big spiral membrane' is proposed shown in the right sub-figure of Figure 53. In this design, long spiral membrane envelops are used instead of the membrane cartridges. Long spiral membrane envelops fill in the ring shape chamber, resulting in a firm membrane pack shown as area with grey color in Figure 54(a). The green curve from the start point to the end point in Figure 54(a) is the

single spiral membrane envelop. Figure 54(b) shows the 3D model of the single spiral membrane envelop. For a CRO device with inner radius = 0.345 m and outer radius = 0.406 m, our device can increase the effective membrane area by 300% comparing with the device used in Vickers' design [109].

Figure 55 shows the schematic of RO membrane assembly. One envelop is formed by a half of a RO membrane and a half of RO membrane that close to it, and then inserted by one permeate carrier. This kind of design and assembly is easy to assemble, and the permeate carrier can be totally isolated from the feed spacer by the RO membrane. The envelope is then glued at three sides except the edge connected to the permeate tube. Feed spacers are inserted between membrane envelops to separate the membrane pieces and behave as the turbulence promotors. This type of the RO membrane assembly in the new CRO device is similar with the membrane wrapping method used in the commercial spiral wound membrane cartridges. The only difference is that for the commercial spiral wound membrane cartridge, the membrane elements are glued and wrapped on a permeate tube with small diameter, and for the desalination centrifuge, we will glue and wrap the membrane elements to a membrane cylinder with much larger diameter. Figure 56 shows the photos of the prototype assembly and the vacuum chamber.

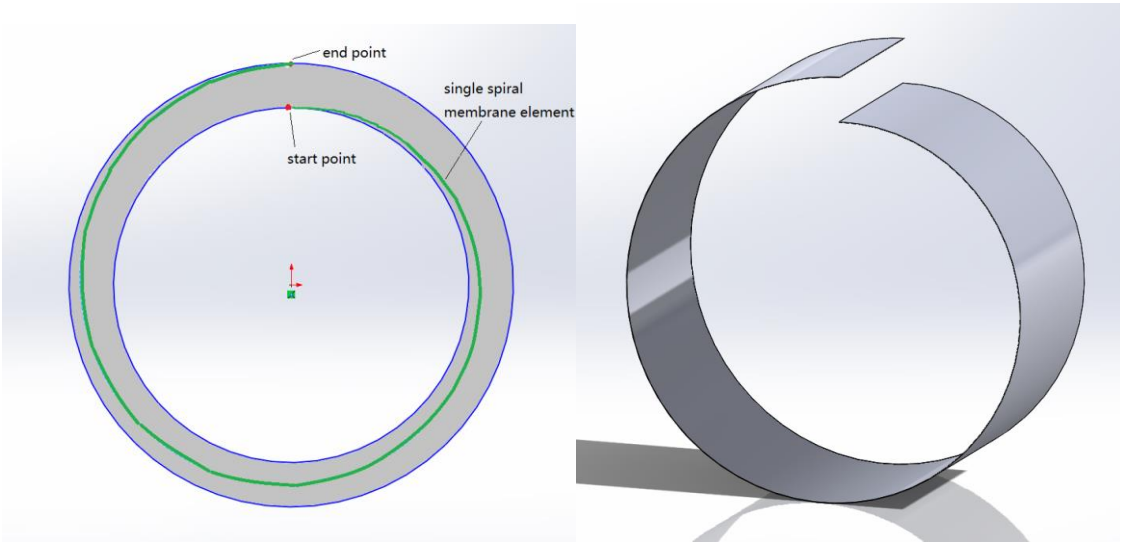

(a) (b)

Figure 54. Single spiral membrane element in new CRO design.

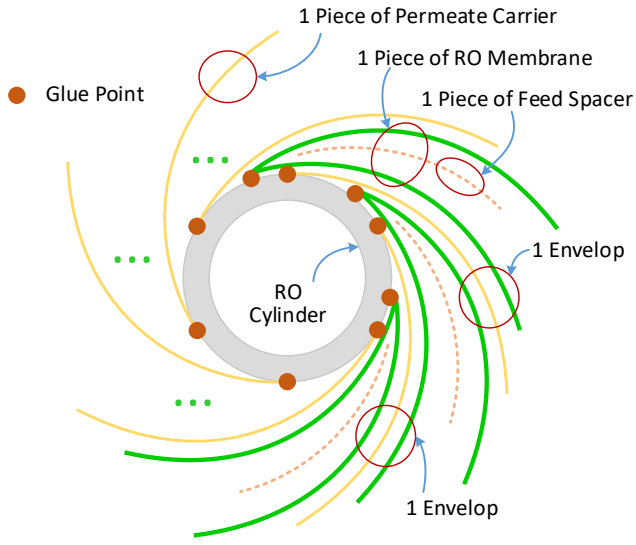

Figure 55. Schematic of RO membrane assembly.

Table 12 shows the system parameters of different new CRO designs and Vickers' design [109]. It is worth noticing that, although the size of the new CRO design with 1 m length × 0.4 m radius × 4 cm thickness (the first column) is around twice of Vickers' design, it can provide 364% and 454% more permeate production at 550 psi pressure and 600 psi respectively. This result shows that our new CRO design can greatly improve the performance of the traditional CRO device at the same device volume. The detailed system performance will be analyzed in the following sections.

6.3. Energy consumption estimation of the CRO device with different parameters

6.3.1. Total power consumption in the CRO device

In this section, the total power consumption in the CRO device is analyzed and summarized. The total power consumption is divided into three main parts: ideal power consumption without power loss, power loss in bearings (friction loss), and fluid pressure loss inside the flow path, and can be seen in equation (67). Considering the complexity of the flow characteristics inside the CRO device, the fluid pressure loss value will be given through CFD simulations. The equations to calculate the other two types of power consumption are derived in the following two sub-sections.

$$P_{total} = P_{ideal} + P_{loss} + P_f \tag{67}$$

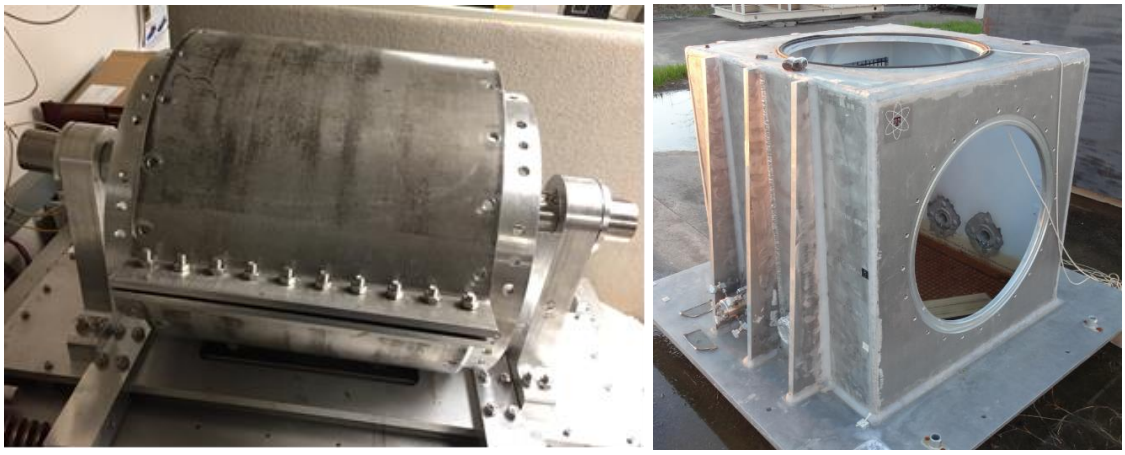

Figure 56. Photos of the prototype assembly (left) and vacuum chamber (right).

Table 12. Datasheet of the new CRO design and Vickers' design

	New CRO Design			Vickers' Design [109]
Dimensions of the membrane pack: length (m) × radius (m) × thickness (cm)	1 × 0.4 × 4	2 × 0.2 × 2	0.2 × 0.2 × 2	16 of the SW30-2521 cartridges
Feed flow rate (gpm)	40	10	10	31.74
Permeate flow rate (gpm)	6.380 gpm for 550 psi pressure	3.063 gpm for 600 psi pressure	0.652 gpm for 600 psi pressure	1.376 gpm for 800 psi pressure
	7.628 gpm for 600 psi pressure	3.482 gpm for 700 psi pressure	0.842 gpm for 700 psi pressure	
Effective membrane area (m2)	211.12	105.56	10.56	19.2
Device dimensions: length (m) × radius (m)	**1.46 × 0.48**	2.46 × 0.25	0.66 × 0.25	**0.733 × 0.406**

6.4.1.1. Ideal power consumption in CRO device

The process pressure of a centrifuge can be denoted as the following equation:

$$P_c = \rho\omega^2 r^2 / 2 \tag{68}$$

where ρ is the fluid density, ω is the centrifuge angular velocity, and r is the centrifuge radius.

Consider the idealized continuous flow centrifuge shown in Figure 57. Although during operation, the centrifuge is in a uniform angular motion, the power consumption is only due to friction, the feed water will be continuously driven by the centrifuge to gain a certain amount of angular momentum described as:

$$\Gamma_d = \rho Q_f \omega r^2 \tag{69}$$

In which Q_f is volumetric flow rate of feed water [m^3/s].

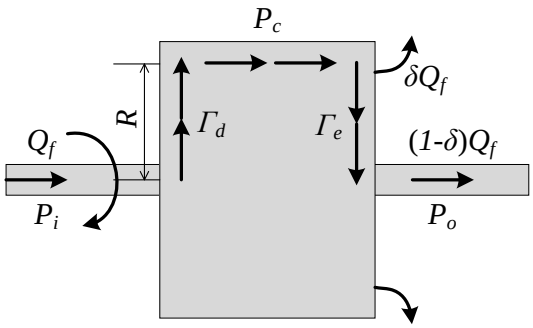

Figure 57. Simplified flow and torque in the desaliantion process.

The permeated pure water will be thrown out from the centrifuge orifice, while the concentrated exhaust water will be collected by the collection side spoke pipes. The angular momentum during this collection process is:

$$\Gamma_e = \rho(1-\delta)Q_f \omega r^2 \tag{70}$$

In which δ is the recovery ratio which describes the fraction of the feed sea water which is converted to fresh water. By conservation of angular momentum, the lost angular momentum by the permeate water is:

$$\Gamma_p = \rho\delta Q_f \omega r^2 \tag{71}$$

Thus in these ideal processes, the respective power consumption will be

$$\begin{aligned} P_d &= \rho Q_f \omega^2 r^2 \\ P_e &= -\rho(1-\delta)Q_f \omega^2 r^2 \end{aligned} \tag{72}$$

The minus of P_e means this power is collected from high pressure water. Thus the total ideal power consumption for these processes will be

$$P_{ideal} = P_d + P_e = \omega\Gamma_p = \rho\delta Q_f \omega^2 R^2 = 2\delta Q_f P_c \tag{73}$$

6.4.1.2. Power loss in bearings

Under certain conditions, the frictional moment can be estimated with sufficient accuracy using a constant coefficient of friction μ. the conditions are

(1) Bearing load P≈0.1C;

(2) Good lubrication;

(3) Normal operating conditions;

The frictional moment under these conditions can be estimated using:

$$\Gamma_f = \mu_b P d/2 \tag{74}$$

where P=equivalent dynamic bearing load [N]; Γ_f =frictional moment [N·m]; μ_b=constant coefficient of friction for the bearing; d_b=bearing bore diameter [m].

Radial bearings are often subjected to simultaneously acting radial and axial loads. If the resultant load is constant in magnitude and direction, the equivalent dynamic bearing load P_b can be obtained from the general equation:

$$P_b = XF_r + YF_a \tag{75}$$

where F_r=actual radial bearing load [N]; F_a=actual axial bearing load [N]; X=radial load factor for the bearing; Y=axial load factor for the bearing.

The actual radial bearing load should be calculated based on the centrifuge weight and the applied shaft radial load by V-Belt pulley and their distribution. Take the case with effective membrane length = 0.2 *m* as an example, the bearing load distribution can be seen in Figure 58. In this figure, the left bearings and right bearings are tapered roller bearings with back-to-back arrangement. The stiffness of this kind of arrangement is large, and it doesn't easy to block when thermal expansion and clearance increase, which is suitable for our application case. The centrifuge weight is W_c = 66 *kg*×9.8 m/s^2=646.7 N. Suppose the centrifuge is well balanced, and ignore the unbalance force. Initially suppose the V-Belt pulley force to the shaft is F_{rB} = 500 N. Since the calculation of bearing loads is for the approximation of frictional moment, the

calculation will be simplified by classifying the four bearings into the left bearings the right bearings.

The force and momentum equilibrium equations in y and z directions for this system can be written as:

$$\begin{aligned} &2F_{yL} + 2F_{yR} - W_c = 0 \\ &2F_{yL}a - 2F_{yR}(b-a) = 0 \\ &2F_{zL} + 2F_{zR} - F_{zB} = 0 \\ &2F_{zL}b + 2F_{zB}c = 0 \end{aligned} \tag{76}$$

By solving this set of equations, we can get F_{yL} = 161.68*N*, F_{yR} = 161.68*N*, F_{zL} = -20.86*N*, and F_{zL} = 270.86*N*, which results in the F_{rmax} = 315.45 N for the single bearing. And the axial forces induced by the radial forces is expressed by formula:

$$F_a = \frac{0.5F_r}{Y} \tag{77}$$

where F_a is the axial component force, F_r is the radial load, and Y is the axial load factor.

For the tapered roller bearing we select from McMaster, the similar tapered roller bearing with the same geometry SKF 32008 X/Q has X = 0.4, Y = 1.6, thus the F_{amax} = 98.58 *N*. And the equivalent dynamic bearing load P_b can be obtained:

$$P_b = 0.4F_{r\max} + 1.6F_{a\max} = 544.15\ N \tag{78}$$

In equation (74), the friction coefficient can be determined by the bearing type. For single row tapered roller bearing, the coefficient is 0.0018~0.0028. From the NSK bearing technical data in Figure 59, the friction is 0.0022. The bearing bore diameter is 40 *mm*.

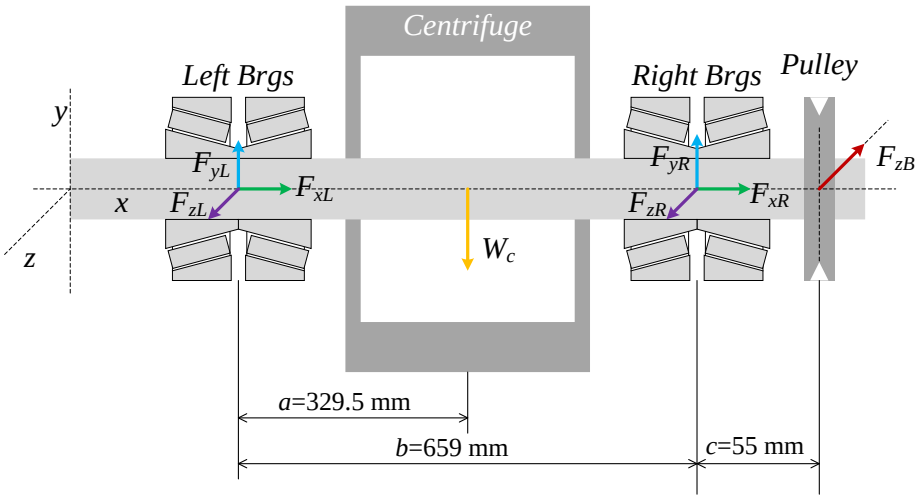

Figure 58. Bearing load distribution.

Bearing Types	Approximate values of μ
Deep Groove Ball Bearings	0.0013
Angular Contact Ball Bearings	0.0015
Self-Aligning Ball Bearings	0.0010
Thrust Ball Bearings	0.0011
Cylindrical Roller Bearings	0.0010
Tapered Roller Bearings	0.0022
Spherical Roller Bearings	0.0028
Needle Roller Bearings with Cages	0.0015
Full Complement Needle Roller Bearings	0.0025
Spherical Thrust Roller Bearings	0.0028

Figure 59. Coefficients of dynamic friction.

So we can calculate:

$$\Gamma_f = \mu P d/2 = 0.0022 \times 544.15N \times 0.04m/2 = 2.394 \times 10^{-2} N \cdot m \quad (79)$$

Thus power P_f required for continuous rotation at 445 *rad/s* and 480 *rad/s* of the centrifuge with 4 bearings are:

$$\begin{aligned} P_{f-445rad/s} &= 4\omega M_f = 4 \times 445\, rad/s \times 2.394 \times 10^{-2} N \cdot m = 42.61W \\ P_{f-480rad/s} &= 4\omega M_f = 4 \times 480\, rad/s \times 2.394 \times 10^{-2} N \cdot m = 45.96W \end{aligned} \quad (80)$$

Above mentioned calculation of the bearing power loss is just an example using the giving size and mass of the CRO device and the rotating speed. The final value may vary with different CRO device and rotating speed.

6.3.2. CFD simulations and power consumption calculations of the CRO concepts with different parameters

In this section, CRO concepts with different parameters (device length, radius and thickness of the membrane pack, feed flow rate, and equivalent applied pressure) were analyzed to get power consumption of each system. In order to compare the efficiency of different systems, 'Unit power consumption' (kWh/m^3) was used here and can be explained as the number of consumed power unit in kWh in order to produce 1 m^3 permeate water. Table 13 shows the detailed parameters for all 6 cases investigated.

Table 13. Parameter summary of all 6 CRO concepts

Case #	1	2	3	4	5	6
Length of the membrane pack (*m*)	1	1	2	2	0.2	0.2
Radius of the membrane pack (*cm*)	40	40	20	20	20	20
Thickness of the membrane pack (*cm*)	4	4	2	2	2	2
Equivalent applied pressure (*psi*)	550	600	600	700	600	700
Feed flow rate (*gpm*)	40	40	10	10	10	10

6.3.2.1. Power consumption of case 1 and case 2

Figure 60 shows the SolidWorks model of case 1 and case 2 used for CFD simulation. In order to get 550 psi and 600 psi applied pressure, this rotation speeds are 215 rad/s (2053 RPM) and 225 rad/s (2148 RPM) respectively for this type of centrifuge device. In the CFD simulations, the applied pressure = 550 psi (37.92 bar) or 600 psi (41.37 bar), feed salt concentration = 32,000 ppm, and feed water volumetric flow rate is $2.5236\times10^{-3}\ m^3/s$ (40 *gpm*). The permeate flux profile among the membrane surface can be found in Figure 61 and Figure 62 for 550 psi and 600 psi applied pressure.

We may find the permeate flux will decrease among the membrane length. When the applied pressure is 550 psi, the averaged permeate flux for 1 m membrane is 1.91×10^{-6} m/s, which results in the recovery ratio = 15.95 %.

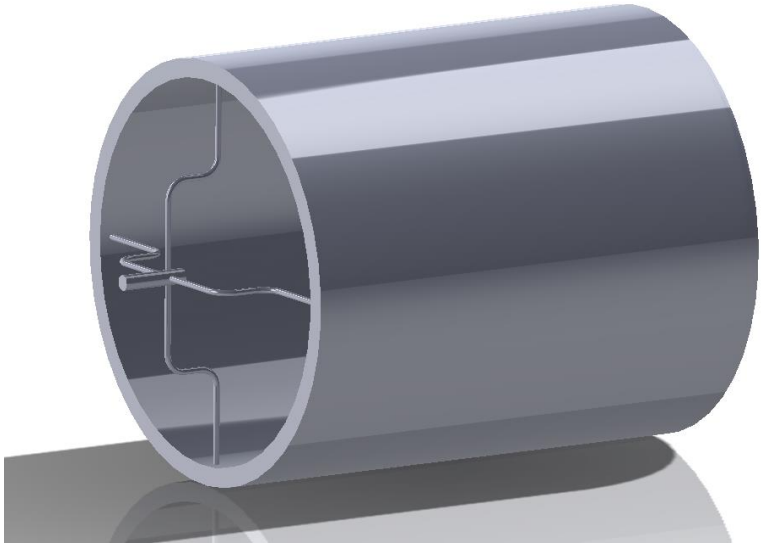

Figure 60. 3D model of the fluid path in the CRO concept with length of 1 m, membrane pack radius of 40 cm, and membrane pack thickness of 4 cm (case 1 and case 2).

Thus, the ideal power consumption during the 550 psi desalination process is:

$$P_{ideal-case1} = 2\delta Q_f P_c = 2\times 0.1595\times 2.5236\times 10^{-3}\times 3.7921\times 10^{6} W = 3052W \qquad (81)$$

When the applied pressure is 600 psi, the averaged permeate flux for 1 m membrane is 2.28×10^{-6} m/s, which results in the recovery ratio = 19.07 %. In this case, the ideal power consumption during the 600 psi desalination process is:

$$P_{ideal-case2} = 2\delta Q_f P_c = 2\times 0.1907\times 2.5236\times 10^{-3}\times 4.137\times 10^{6} W = 3982W \qquad (82)$$

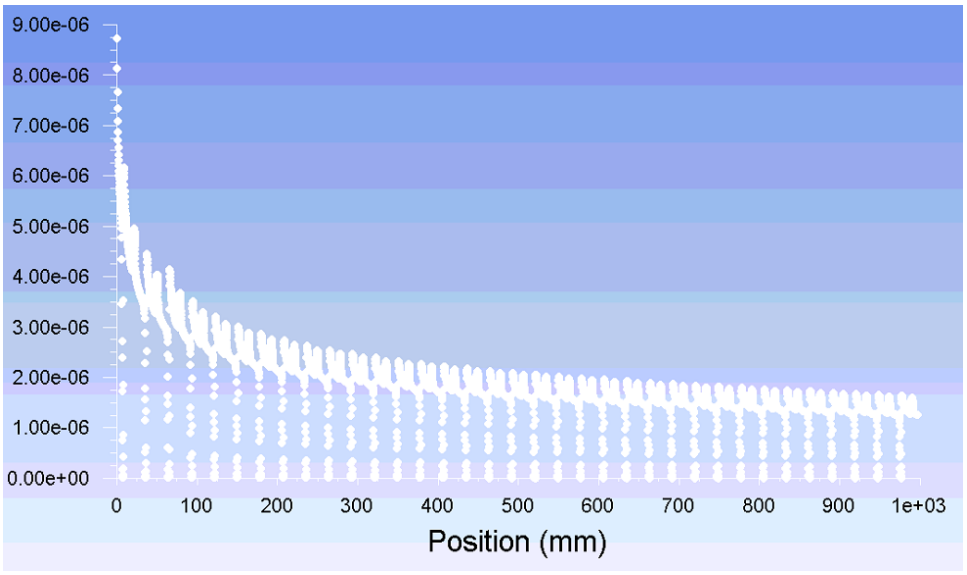

Figure 61. Permeate flux (m/s) distribution among the membrane surface in case 1.

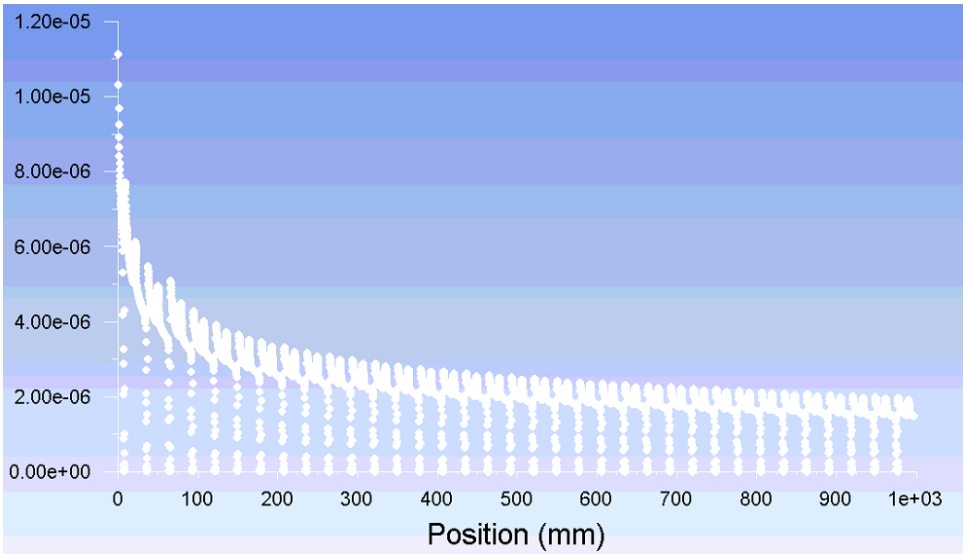

Figure 62. Permeate flux (m/s) distribution among the membrane surface in case 2.

When we consider the pressure loss inside the water desalination process, we need to calculate the averaged pressure difference between device inlet and device outlet.

Figure 63 shows the pressure distribution inside the membrane pack for case 1. We may find the pressure increases linearly with the distance from the rotation axis. And the pressure range of the membrane wrap is 550 *psi* to 610 *psi*. Figure 64 shows the pressure distribution in the cut plane of case 1. Similar with case 1, simulation for case 2 was also performed. Figure 65 and Figure 66 show the pressure distribution inside the membrane pack and the cut plane for case 2.

Pressure loss inside the centrifuge device can be calculated by subtract outlet pressure by inlet pressure. Figure 67 shows the averaged inlet and outlet pressure calculated by CFD simulations for CRO cases with 1 *m* membrane length and the pressure loss is 28.33 *psi* (1.95 *bar*).

Thus, the pressure loss induced energy consumptions for case 1 and case 2can be calculated as the following equations:

$$\begin{aligned} P_{loss-case1} &= 2(1-\delta)Q_f \Delta P = 2\times(1-0.1595)\times 2.5236\times 0.195\times 10^3 W = 828W \\ P_{loss-case2} &= 2(1-\delta)Q_f \Delta P = 2\times(1-0.1907)\times 2.5236\times 0.195\times 10^3 W = 798W \end{aligned} \tag{83}$$

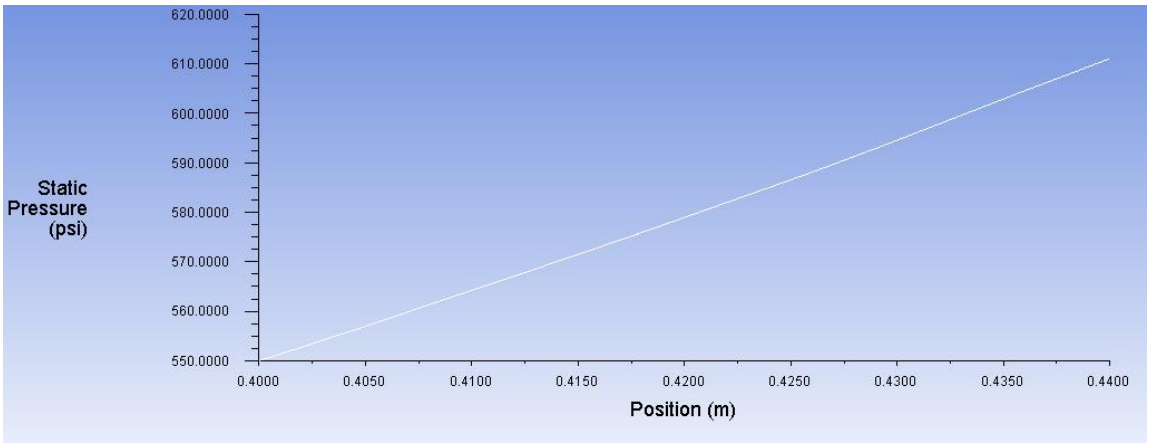

Figure 63. Pressure distribution inside the membrane pack (case 1).

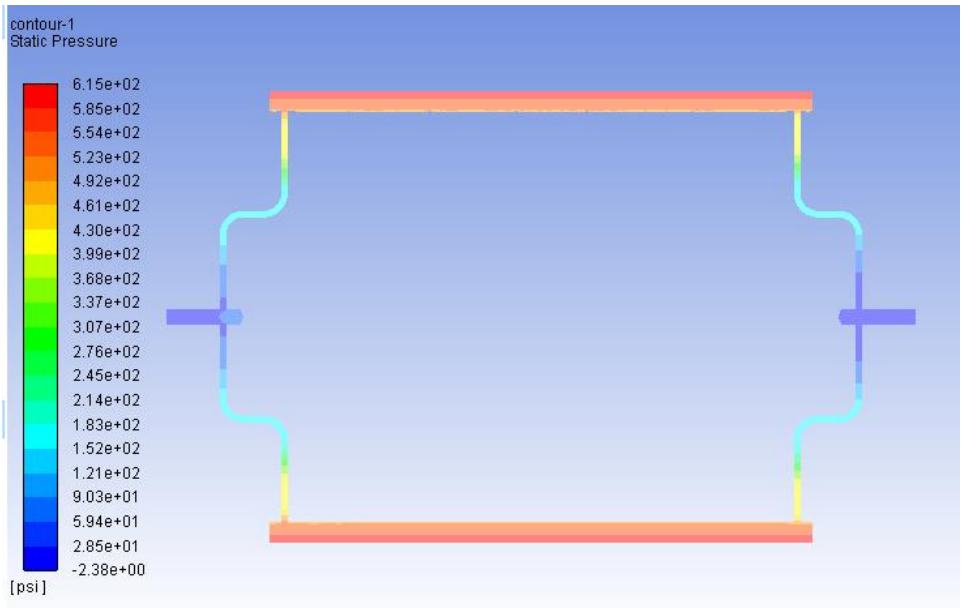

Figure 64. Pressure distribution in the cut plane of case 1.

Considering the size of the CRO device deployed in both case 1 and case 2 (0.4 m radius x 1 m length), the corresponding bearing friction losses for both cases can be calculated as:

$$\begin{aligned} P_{f-case1} &= 4\omega_{case1} M_f = 4 \times 215\, rad/s \times 7.944 \times 10^{-2}\, N \cdot m = 68W \\ P_{f-case2} &= 4\omega_{case2} M_f = 4 \times 225\, rad/s \times 7.944 \times 10^{-2}\, N \cdot m = 71W \end{aligned} \tag{84}$$

And the total power consumptions for case 1 and case 2 are:

$$\begin{aligned} P_{total-case1} &= P_{ideal-case1} + P_{loss-case1} + P_{f-case1} = 3052 + 828 + 68W = 3948W \\ P_{total-case2} &= P_{ideal-case2} + P_{loss-case2} + P_{f-case2} = 3982 + 798 + 71W = 4851W \end{aligned} \tag{85}$$

The corresponding permeate rates for case 1 and case 2 are:

$$\begin{aligned} Q_{p-case1} &= \delta_{case1} Q_f = 0.1595 \times 40gpm = 6.38gpm = 1.45\, m^3/h \\ Q_{p-case2} &= \delta_{case2} Q_f = 0.1907 \times 40gpm = 7.63gpm = 1.73\, m^3/h \end{aligned} \tag{86}$$

So, the corresponding unit power consumptions for 550 psi case and 600 psi case are:

$$\begin{aligned} G_{case1} &= P_{total-case1} / Q_{p-case1} = 2.72 \text{kWh/m}^3 \\ G_{case2} &= P_{total-case2} / Q_{p-case2} = 2.80 \text{kWh/m}^3 \end{aligned} \tag{87}$$

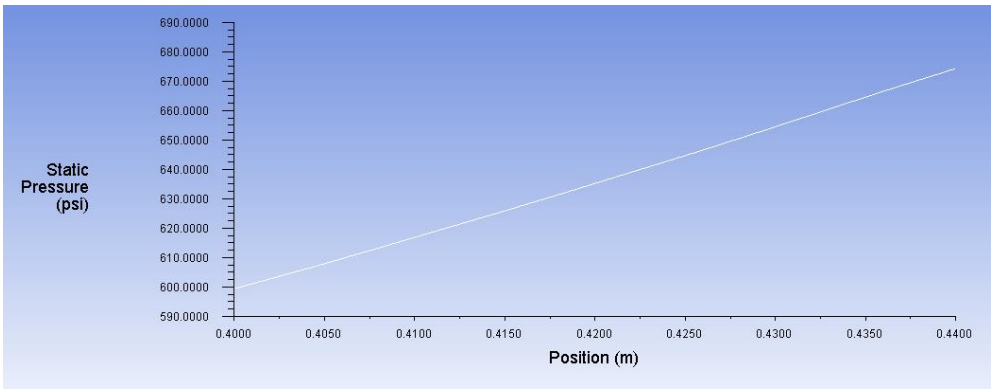

Figure 65. Pressure distribution inside the membrane pack (case 2).

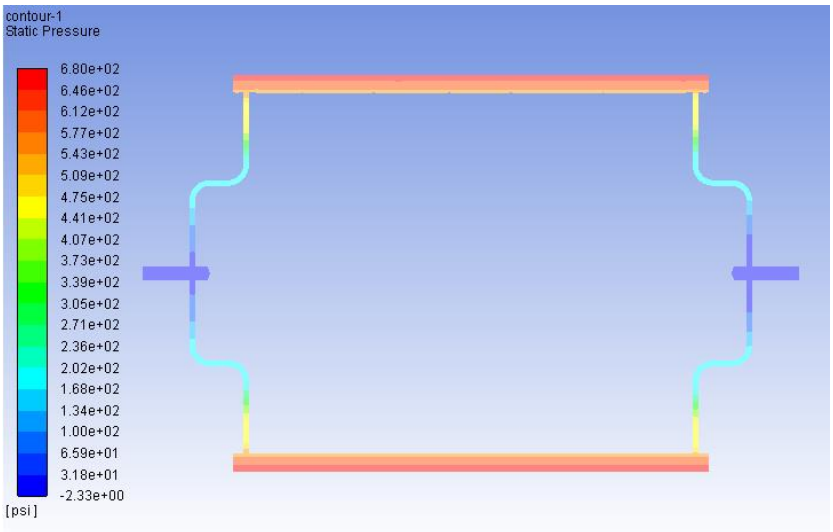

Figure 66. Pressure distribution in the cut plane of case 2.

	Area-Weighted Average Static Pressure (psi)
inlet	28.336298

	Area-Weighted Average Static Pressure (psi)
outlet	-0.00083547689

Figure 67. Averaged inlet and outlet pressure for CRO concepts with length of 1 m.

6.3.2.2. Power consumption of case 3 and case 4

Figure 68 shows the SolidWorks model of the computational domain used for case 3 and case 4. In order to get the corresponding equivalent applied pressure as 600 *psi* and 700 *psi*, centrifuge rotation speeds should be 447 *rad/s* (4268 *RPM*) and 482 *rad/s* (4600 *RPM*) respectively. In this set of CFD simulations, the applied pressure = 600 *psi* (41.37 *bar*) or 700 *psi* (48.26 *bar*), feed salt concentration = 32,000 *ppm*, and feed water volumetric flow rate = $6.3\times10^{-4}\ m^3/s$ (10 *gpm*). The permeate flux profile among the membrane surface can be found in Figure 69 and Figure 70 for case 3 and case 4. From these two figures, we can calculate the averaged permeate flux and recovery ratio for case 3 are 1.83×10^{-6} *m/s* and 30.63%; the averaged permeate flux and recovery ratio for case 4 are 2.08×10^{-6} *m/s* and 34.82 %. Thus, the ideal power consumption for both cases are:

$$P_{ideal-case1} = 2\delta Q_f P_c = 2\times 0.3063\times 6.3\times 10^{-4}\times 4.137\times 10^6 W = 1597W$$
$$P_{ideal-case2} = 2\delta Q_f P_c = 2\times 0.3482\times 6.3\times 10^{-4}\times 4.826\times 10^6 W = 2117W \quad (88)$$

Figure 71 shows the pressure distribution inside the membrane pack for case 3. We may find the pressure increases linearly with the distance from the rotation axis. And the pressure range of the membrane wrap is 600 psi to 680 psi. Figure 72 shows the pressure distribution in the cut plane of case 3. Similar with case 3, simulation for case 4 was also performed. Figure 73 and Figure 74 show the pressure distribution inside the membrane pack and the cut plane for case 4.

Pressure loss inside the centrifuge device can be calculated by subtract outlet pressure by inlet pressure. Figure 75 shows the averaged inlet and outlet pressure calculated by CFD simulations for 2 meter CRO cases and the pressure loss is 39.68 *psi* (2.73 *bar*).

Thus, the pressure loss induced energy consumptions for case 3 and case 4 can be calculated as the following equations:

$$P_{loss-case3} = 2(1-\delta)Q_f \Delta P = 2\times(1-0.3063)\times 6.3\times 10^{-4}\times 0.273\times 10^6 W = 239W$$
$$P_{loss-case4} = 2(1-\delta)Q_f \Delta P = 2\times(1-0.3482)\times 6.3\times 10^{-4}\times 0.273\times 10^6 W = 225W \quad (89)$$

Considering the size of the CRO device deployed in both case 3 and case 4 (0.2 m radius x 2 m length), the corresponding bearing friction losses for both cases can be calculated as:

$$P_{f-case3} = 4\omega_{case3} M_f = 4 \times 447\, rad/s \times 8.923 \times 10^{-2}\, N \cdot m = 159W$$
$$P_{f-case4} = 4\omega_{case4} M_f = 4 \times 482\, rad/s \times 8.923 \times 10^{-2}\, N \cdot m = 172W \quad (90)$$

And the total power consumptions for case 3 and case 4 are:

$$P_{total-case3} = P_{ideal-case3} + P_{loss-case3} + P_{f-case3} = 1597 + 239 + 159W = 1995W$$
$$P_{total-case4} = P_{ideal-case4} + P_{loss-case4} + P_{f-case4} = 2117 + 225 + 172W = 2514W \quad (91)$$

The corresponding permeate rates for case 3 and case 4 are:

$$Q_{p-case3} = \delta_{case3} Q_f = 0.3063 \times 10 gpm = 3.06 gpm = 0.7\, m^3/h$$
$$Q_{p-case4} = \delta_{case4} Q_f = 0.3482 \times 10 gpm = 3.48 gpm = 0.79\, m^3/h \quad (92)$$

So, the corresponding unit power consumptions for case 3 and case 4 are:

$$G_{case3} = P_{total-case3} / Q_{p-case3} = 2.85 \text{kWh/m}^3$$
$$G_{case4} = P_{total-case4} / Q_{p-case4} = 3.18 \text{kWh/m}^3 \quad (93)$$

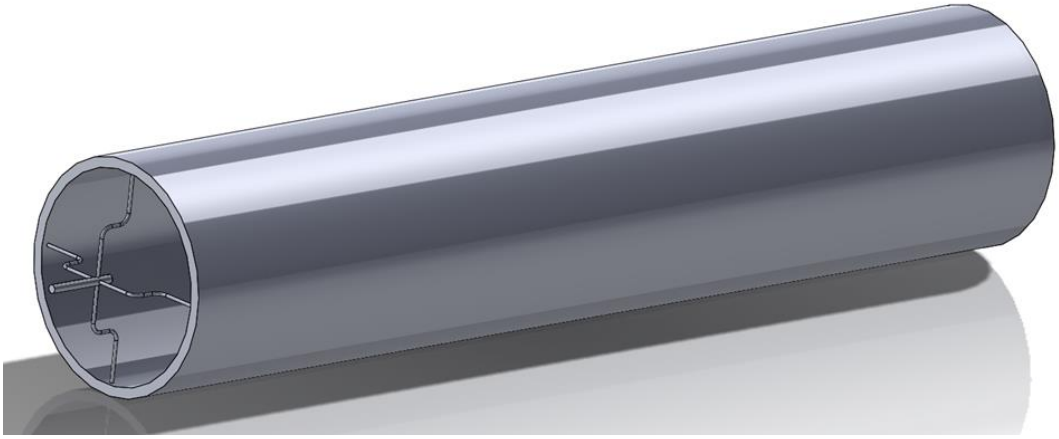

Figure 68. SolidWorks model of the fluid path in the CRO concept with length of 2 m, membrane pack radius of 20 cm, and membrane pack thickness of 2 cm (case 3 and case 4).

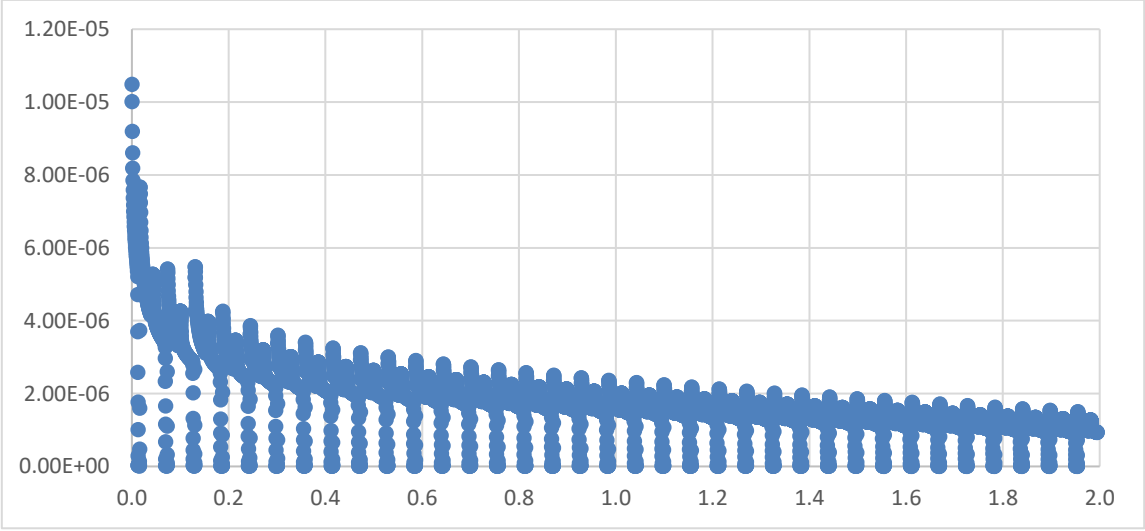

Figure 69. Permeate flux (m/s) distribution among the membrane surface (m) in case 3.

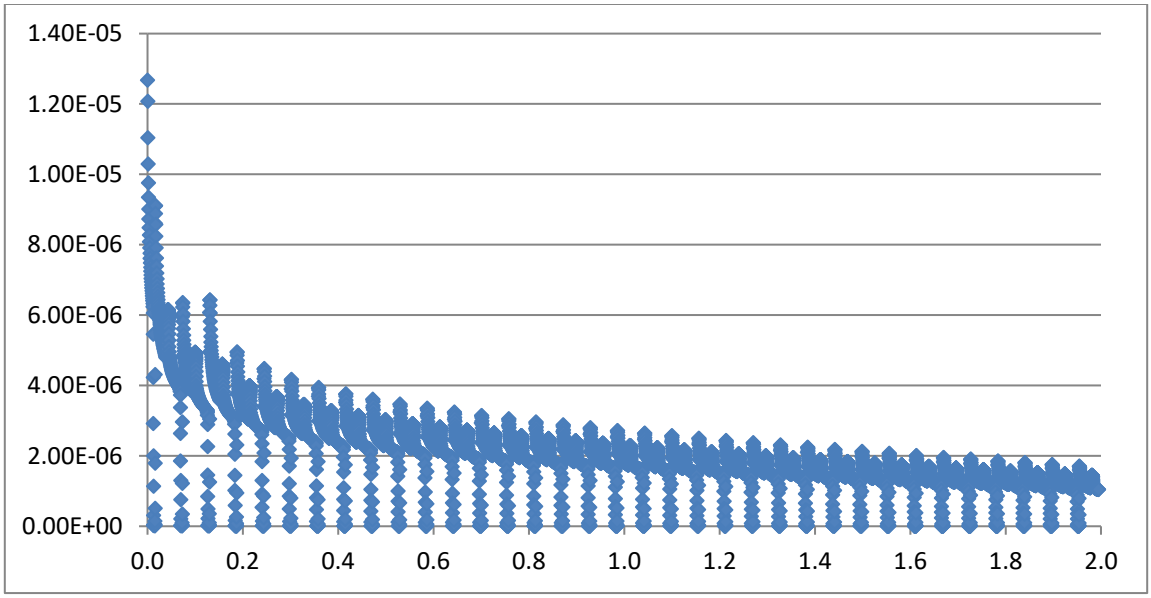

Figure 70. Permeate flux (m/s) distribution among the membrane surface (m) in case 4.

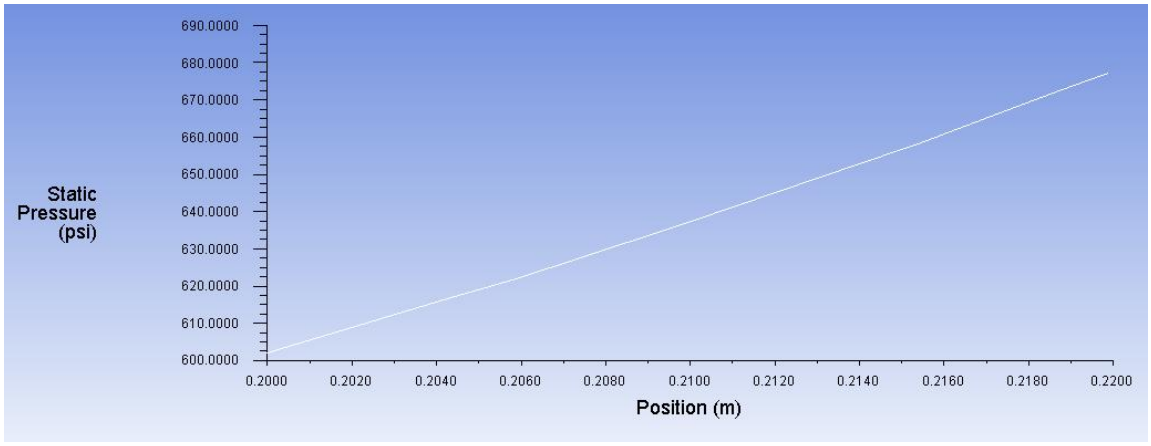

Figure 71. Pressure distribution inside the membrane pack (case 3).

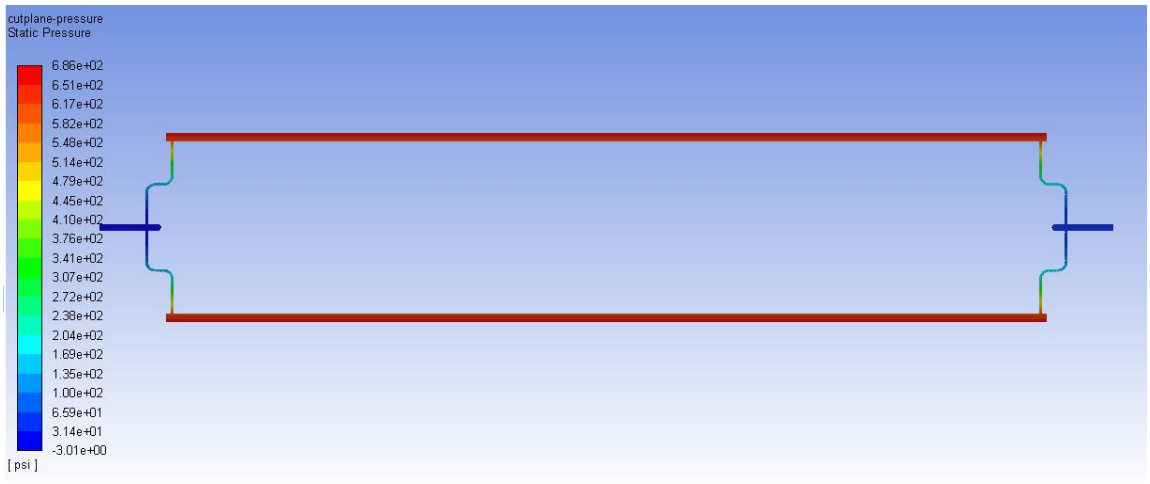

Figure 72. Pressure distribution in the cut plane of case 3.

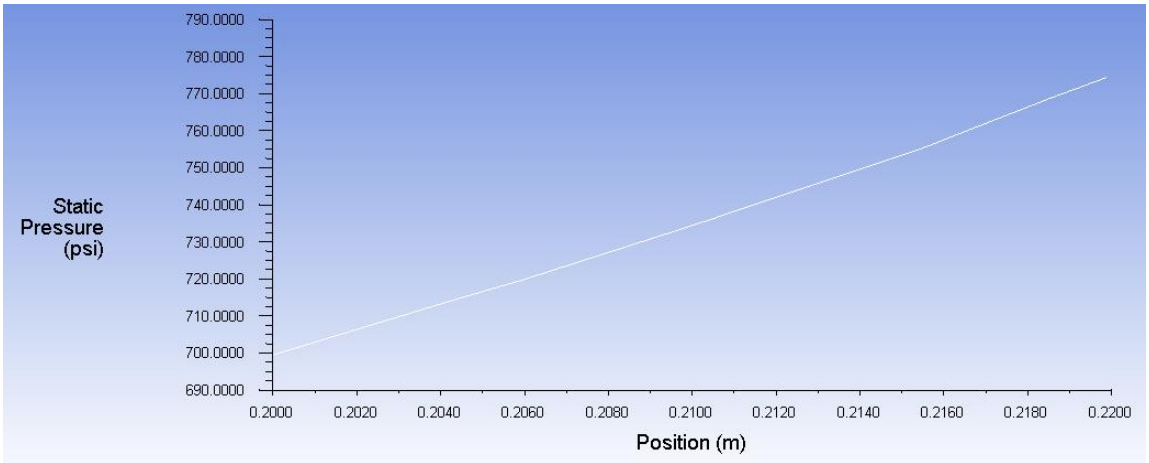

Figure 73. Pressure distribution inside the membrane pack (case 4).

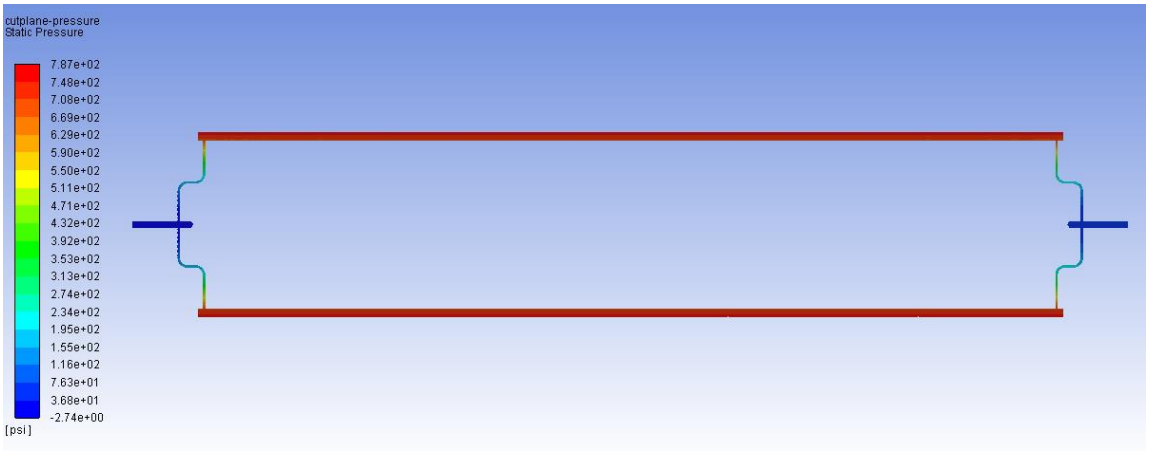

Figure 74. Pressure distribution in the cut plane of case 4.

Area-Weighted Average Static Pressure	(psi)
inlet	39.689766

Area-Weighted Average Static Pressure	(psi)
outlet	0

Figure 75. Averaged inlet and outlet pressure for CRO concepts with length of 2 m.

6.3.2.3. Power consumption of case 5 and case 6

Similar calculation processes can also be performed for case 5 and case 6. When the applied pressure is 600 *psi*, the averaged permeate flux for the 0.2 meter membrane is 3.86×10^{-6} *m/s*, which results in the recovery ratio = 6.52%. The ideal power consumption for case 5 is:

$$P_{ideal-case5} = 2\delta Q_f P_c = 2\times 0.0652\times 6.3\times10^{-4}\, m^3/s\times 4.137\times10^6\, N/m^2 = 340W \qquad (94)$$

When the applied pressure is 700 psi, the averaged permeate flux for the 0.2 meter membrane is 4.99×10^{-6} m/s, which results in the recovery ratio = 8.42 %. Thus, the ideal power consumption for case 6 is:

$$P_{ideal-case6} = 2\delta Q_f P_c = 2\times 0.0842\times 6.3\times10^{-4}\, m^3/s\times 4.826\times10^6\, N/m^2 = 512W \qquad (95)$$

From the results of CFD calculations, for 0.2 *m* CRO devices, the pressure loss from inlet to the outlet is around 1.35 *bar*. Thus, the pressure loss caused energy consumption can be calculated as the following equations:

$$\begin{aligned} P_{loss-case5} &= 2(1-\delta)Q_f\Delta P = 2\times(1-0.0652)\times 6.3\times10^{-4}\times 0.135\times10^6 W = 159W \\ P_{loss-case6} &= 2(1-\delta)Q_f\Delta P = 2\times(1-0.0842)\times 6.3\times10^{-4}\times 0.135\times10^6 W = 156W \end{aligned} \qquad (96)$$

As we calculated in section 6.3.1.2., the bearing friction losses for case 5 and case 6 should be 43 *W* and 46 *W*. So, the total power consumptions for both cases are:

$$\begin{aligned} P_{total-case5} &= P_{ideal-case5} + P_{loss-case5} + P_{f-case5} = 340+159+43W = 542W \\ P_{total-case6} &= P_{ideal-case6} + P_{loss-case6} + P_{f-case6} = 512+156+46W = 714W \end{aligned} \qquad (97)$$

The corresponding permeate rates for case 5 and case 6 are:

$$Q_{p-case5} = \delta_{case5} Q_f = 0.0652 \times 10 gpm = 0.652 gpm = 0.148 m^3/h$$
$$Q_{p-case6} = \delta_{case6} Q_f = 0.0842 \times 10 gpm = 0.842 gpm = 0.191 m^3/h \quad (98)$$

So, the corresponding unit power consumptions for case 5 and case 6 are:

$$G_{case5} = P_{total-case5} / Q_{p-case5} = 3.66 \text{kWh/m}^3$$
$$G_{case6} = P_{total-case6} / Q_{p-case6} = 3.74 \text{kWh/m}^3 \quad (99)$$

6.3.2.4. Summary

Table 14 summarizes the main calculation results for all 6 CRO devices. Typical cost of energy ranges for medium & large SWRO plants are listed in Table 15 [114]. By comparing the system energy usage data in both tables, it is clear to see the unit power consumption of all 6 CRO concepts are within the typical energy use range of the mediums and large size SWRO systems. And case 1 and case 2 are within the low-end bracket classification which have extreme low energy use.

It is worthy noticing that the medium and large size SWRO systems typically have huge capital cost varying from 50 million – 600 million US$, however, the capital cost of our CRO concepts is less than 50 thousands US$, which is only 0.1% of the capital cost of typical medium and large size SWRO systems. In sum, our CRO concepts have extreme low capital cost and competitive energy cost compared with current medium and large size SWRO systems.

Table 14. Summary of power consumption estimations of all 6 CRO concepts.

Case #	1	2	3	4	5	6
Length of the membrane pack (*m*)	1	1	2	2	0.2	0.2
Radius of the membrane pack (*cm*)	40	40	20	20	20	20
Thickness of the membrane pack (*cm*)	4	4	2	2	2	2
Equivalent applied pressure (*psi*)	550	600	600	700	600	700
Feed Flow Rate (*gpm*)	40	40	10	10	10	10
Recovery ratio (%)	15.95	19.07	30.63	34.82	6.52	8.42
System power consumption (*W*)	3948	4851	1995	2514	542	714
Unit power consumption (*kWh/m^3*)	**2.72**	**2.80**	**2.85**	**3.18**	**3.66**	**3.74**

Table 15. Typical cost and energy use for medium and large SWRO systems [114].

Classification	Cost of water production (*US$/m^3*)	SWRO system energy use (*kWh/m^3*)
Low-End Bracket	0.5-0.8	2.5-2.8
Medium Range	0.9-1.5	2.9-3.2
High-End Bracket	1.6-3.0	3.3-4.0

6.4. Operation cost estimation and ROI study of the new CRO device

6.4.1. Operation cost estimation and comparison

In this section, the operation cost of the new CRO device and the conventional device are estimated and compared. The cost estimation of the conventional RO method using the spiral wound membrane module is investigated based on the 'RO tools – cost of operation' developed by GE Water Technologies & Solutions [115]. The input data for the RO tools are summarized in the Table 16 and the corresponding calculation results can be found in the screenshot Figure 76. From Figure 76, it is clear to see the total operation cost is 6.34 US$/kgal (≈1.68 US$/m^3). The operation cost estimated by the RO tools is reasonable and is inside the range of the high-end bracket in Table 15.

Table 16. Input Parameter for the GE RO Tools.

Input Parameters		**Value**	**Unit**
RO Specifications	Product Water Flow	1	GPM
	RO Recovery	35%	NA
Operation	Hours/Day of Operation	24	Hours
	Days/Year of Operation	365	Days
Utilities	Cost of Electricity	0.07	$/kWh
	Power	460	VAC
	RO Pump Efficiency	70%	NA
	RO Pump Pressure	600	PSI
RO Membrane	RO Membrane Replacement	2	Years
	No. of RO Membranes	1	NA
	Price Per RO Membrane	500	$
Cleaning	Cleaning Frequency	90	Days
	Cleaning Cost	7	$/lb. of Chemical

System Design				
Operating Hours:	24	hours per day		
Operating Days:	365	days per year		
Finished Water:	525,600	gallons per year		
Plant Recovery:	35	%		
RO Feed Flow:	3	gpm		
Total Concentrate Flow:	2	gpm		
Total Permeate Flow:	1	gpm		
Cost of Operations Totals				
Electricity:	19.74	kWh / 1000 gallons	$1.38	/ 1000 gallons
Chemicals:	1.357	lbs / 1000 gallons	$0.36	/ 1000 gallons
Inlet Cartridge Filters:	$0.00	per change	$0.00	/ 1000 gallons
RO Membrane Replace:	$500.00	per change	$0.48	/ 1000 gallons
Membrane Cleaning:	$14.00	per cleaning	$0.11	/ 1000 gallons
Labor:			$1.39	/ 1000 gallons
Feed Water:			$1.14	/ 1000 gallons
Sewer Treatment:			$1.49	/ 1000 gallons
TOTAL:	$6.34	/ 1000 gallons	of finished water produced	
TOTAL without Water/Sewer:	$3.72	/ 1000 gallons	of finished water produced	

Figure 76. Operation cost of conventional RO method calculated by GE RO tools。

The similar operation cost estimation can also be performed for the new CRO device, and can be found in Figure 77. The main differences between commercial product cost and cost of the new CRO device are:

(1) Since the centrifugal force inside the CRO device enhances the permeate flux production of the RO membrane [113], higher recovery rate is assumed to increase from 35% to 40% while keeping the recycle water ratio as the same. Higher recovery rate means that less feed flow rate is needed for the same permeate flow rate. Reduced feed

flow rate will reduce the electricity cost, chemicals cost, membrane cleaning cost, feed water cost and sewer treatment cost.

(2) In the new CRO device, no high-pressure flow loop system and high pressure pump are needed. A major source of unreliability in the commercial RO plant is the high-pressure pump and, in particular, the high-pressure seals. Missing high pressure components will greatly reduce the labor cost from $1.39/1000 gallons to $0.69/1000 gallons.

(3) The membrane fouling trend will be delayed due to the centrifugal force [116]. And this will reduce the chemical cost.

Due to the limitation of GE RO tools, the electricity cost for centrifuge components cannot be estimated via their tools. Electric rates of small commercials in the City of College Station, Texas is 0.1344 *US$/KWh* [117]. Based on the calculations performed in Section 6.3., the additional electricity cost is around 0.50 *US$/m*^{3}. Combining the results from Figure 77, the total operation cost of the new CRO device is 1.18 *US$/m*^{3} (4.47 *US$/kgal*). This value is 30% lower compared with the operation cost also calculated using the GE RO tools shown in Figure 76. This value is also within the medium range cost of water production for medium and large SWRO systems shown in Table 15.

By assuming the system working for 24 hours per day and 365 days per year, the annual operation cost for the new CRO device is:

$$\text{Cost} = 1.18 * 0.148 * 24 * 365 = 1529.85 \text{ USD / year} \quad (100)$$

System Design				
Operating Hours:	24	hours per day		
Operating Days:	365	days per year		
Finished Water:	525,600	gallons per year		
Plant Recovery:	40	%		
RO Feed Flow:	3	gpm		
Total Concentrate Flow:	2	gpm		
Total Permeate Flow:	1	gpm		
Cost of Operations Totals				
Electricity:	4.32	kWh / 1000 gallons	$0.30	/ 1000 gallons
Chemicals:	0.729	lbs / 1000 gallons	$0.18	/ 1000 gallons
Inlet Cartridge Filters:	$0.00	per change	$0.00	/ 1000 gallons
RO Membrane Replace:	$500.00	per change	$0.48	/ 1000 gallons
Membrane Cleaning:	$14.00	per cleaning	$0.11	/ 1000 gallons
Labor:			$0.69	/ 1000 gallons
Feed Water:			$1.00	/ 1000 gallons
Sewer Treatment:			$1.20	/ 1000 gallons
TOTAL:	$3.96	/ 1000 gallons	of finished water produced	
TOTAL without Water/Sewer:	$1.76	/ 1000 gallons	of finished water produced	

Figure 77. Operation cost of the new CRO device calculated by the GE RO tools.

6.4.2. Return on Investment (ROI) Study of the new CRO device

A performance measure used to evaluate the efficiency of an investment or to compare the efficiency of a number of different investments. ROI measures the amount of return on an investment relative to the investment's cost. To calculate ROI, the benefit (or return) of an investment is divided by the cost of the investment, and the result is expressed as a percentage or a ratio.

The return on investment formula:

$$\text{ROI} = \frac{\left(\text{Gain from Investment} - \text{Cost of Investment}\right)}{\text{Cost of Investment}} \tag{101}$$

The Gain from Investment is the sales income from the fresh water, which is around 443,000 gallons/year of the new CRO device. The estimated price of the fresh water is 1 cent per gallon. The cost investment includes the prototype development cost, which is summarized in Table 17, and the annual operation cost, calculated in section 6.4.1 as $1529.85. Please note that, the total investment listed in Table 17 is the initial development cost, which will be reduced in commercialization.

Table 17. Summary of the new CRO device development cost.

Part name	Price	Machine Shop/ Source
Bearing Housing and Cap	$1,292.00	On Campus
Base Plate	$840.00	On Campus
Bearing Drive Plate	$414.00	On Campus
Membrane Retaining Ring	$1,000.00	On Campus
Bearing Housing Cap	$310.00	On Campus
Keys	$135.00	On Campus
Driving Flange	$2,970.00	Conroe Machine
Rotor	$1,824.00	Conroe Machine
Cover Ring	$1,330.00	Conroe Machine
Collect Ring	$2,700.00	Conroe Machine
Cover Cylinder	$900.00	East Texas Machine
Permeate Cylinder	$2,950.00	East Texas Machine
1.25"*20" stainless steel Pipe	$125.34	Bryan Hose and Gasket
1"* 20" stainless steel pipe	$33.19	Bryan Hose and Gasket
1.25"-1" Al pipe elbow	$25.36	Bryan Hose and Gasket
3/4"* 20" stainless steel pipe	$51.44	Bryan Hose and Gasket
1"-3/4" Al pipe elbow	$39.88	Bryan Hose and Gasket
1.5"*20" stainless steel pipe	$49.31	McMaster
1-1/4"-1" Al inline reducing Tees	$33.58	McMaster
Inline Reducing Tee(3/4 FNPT inlet & outlet, 3/8 bypass)	$19.34	McMaster
Reducing tee (Al, 1 FNPT bypass &inlet, 3/4 FNPT outlet)	$25.39	McMaster
Reducing coupling (1-1/4 to 1)	$14.69	McMaster
Inline flow meter	$404.00	Grainger
Pressure gauge	$100.00	Bryan Hose and Gasket
Feed pump	$849.80	Hypropumps
Rotary union	$398.00	Rotary Unions
Pressure relief valve	$372.00	McMaster
Tank	$360.00	Sprayer Depot
Other piping system	$1,000.00	Bryan Hose and Gasket
Accessories	$2,894.00	McMaster
Reverse Osmosis Membrane	$1,780.00	Progressive Water
TOTAL	$25,240.32	

Figure 78 is the profit prediction for commercialization of the proposed new CRO technology. From Figure 78 we can see that the investor will start gain profit after 9 years of plant operation. By assuming the system can operate for 30 years, a total profit over 60k US$ can be achieved by this new CRO device which has the initial investment of 25.2k US$.

Figure 79 is the study result of the return on investment. From Figure 79 we can see that besides the conclusion that the plant will gain profit after 11 years, the ROI can reach 60% after 20 years of operation and 87% after 30 years of operation.

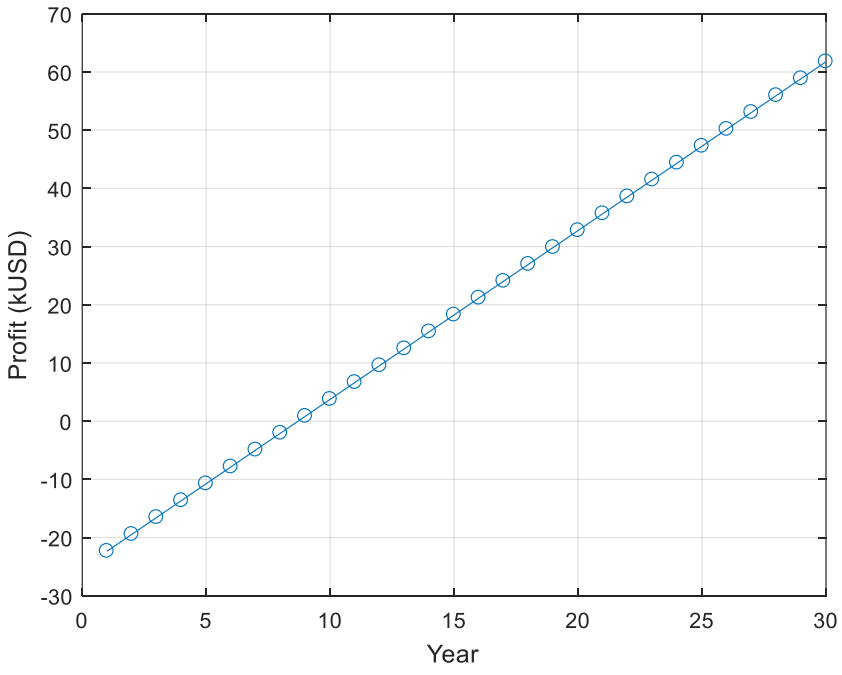

Figure 78. Profit prediction for commercialization of the proposed new CRO concept.

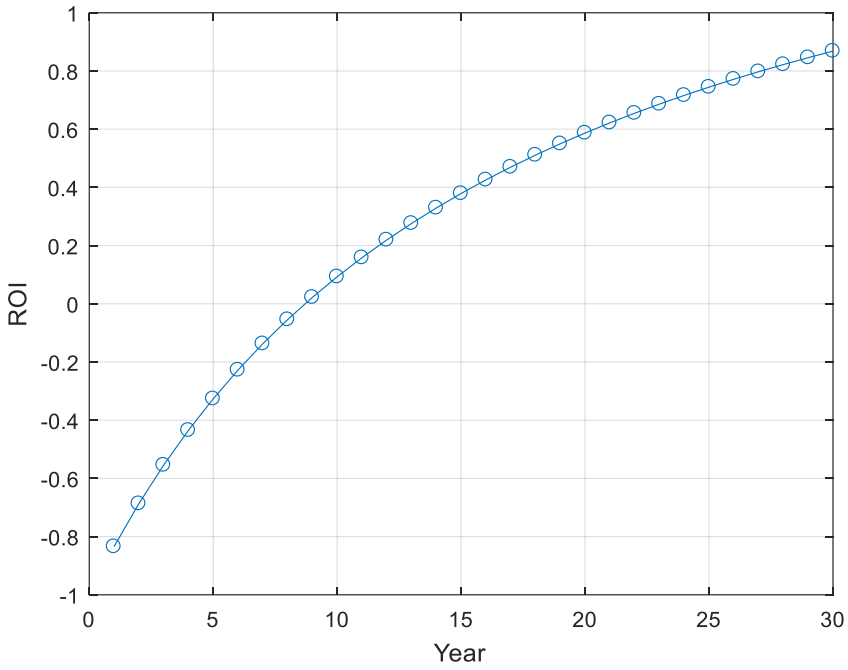

Figure 79. ROI prediction for commercialization of the proposed new CRO concept.

6.5. Conclusions

In this chapter, a new CRO technology is proposed to reduce the energy consumption and device size. The area of effective membrane surface increases by 300% compared with traditional CRO device in the same device size. Energy consumption estimations of 6 different new CRO devices were performed using CFD simulations. Results show that the energy cost of the new CRO concept is competitive compared with current medium and large size SWRO systems, while the capital cost is only 0.1% of the medium and large size SWRO systems. Finally, operation cost estimation was performed with the help of GE RO tools. Results show that, for the new CRO device, the initial capital investment is 25240.32 US$ and the annual operation cost is 1529.85 US$. This operation cost is 30% lower compared with the convectional membrane desalination plant. Return on Investment (ROI) study also shows that a total profit over 60k USD and 87% of the ROI can be achieved within 30 years operation of the new CRO system.

7. CONCLUSIONS AND FUTURE WORK

7.1. Conclusions

The growing need for clean fresh water for drinking and industrial usage has motivated significant research and development efforts for obtaining low cost and reliable approaches to desalination. Reverse osmosis (RO) membrane has been widely adopted in the desalination industry, especially in seawater desalination and brackish water desalination. Membrane fouling, especially colloidal fouling, is considered to be one of the major challenges in the RO desalination industry, which requires chemical cleansing or replacement. Accurate prediction and effective control of the membrane colloidal fouling are needed. Also, in the convectional RO plant, the high pressure pump increases the system instability and consumes a lot of energy.

In Chapter 2, a comprehensive literature review on fundamental of RO membrane desalination, membrane concentration polarization (CP), and colloidal fouling were presented.

In Chapter 3, a novel vibration enhanced reverse osmosis technology was proposed to address the RO membrane CP problem, with the aim of increasing membrane permeate flux and reducing membrane salt concentration. In this technique, a RO membrane desalination cell is driven by linear actuators to impose axial rapid membrane vibration and large membrane surface shear rates. The CFD predicted eddies near the membrane surface in the vibration cases reduced the *NaCl* and *CaSO4* CP and consequently increased the membrane mass transfer rate. The reduced membrane *CaSO4*

CP resulting from the imposed vibration also reduces the membrane local gypsum fouling rate. The simulations showed that the CP modulus decreases and the permeate flux increases as the vibration frequency increases, with a constant amplitude imposed vibration. The improvements in CP and flux change rapidly up to 20 Hz. and then slow considerably for higher frequencies. This suggests that in tuning the vibratory system it is important to locate and use the minimum frequency above which added benefits are relatively small. This will save power and equipment costs. This result was also confirmed by experimental measurements.

In Chapter 4, a numerical model simulating colloidal particle deposition and fouling was proposed to accurately predict the membrane performance under the colloidal fouling. The animation of the colloidal fouling layer growth with time was depicted by simulating the process of colloidal particles deposition on membrane surface and occupying fluid zone into porous cake zone. A numerical method was used to simplify this physical gradual deposition problem into a cell by cell problem. The cell-based colloidal fouling cake layer, which was treated as a homogeneous porous media domain with constant porosity, has the effect on both fluid flow and solute mass transfer. The influence of membrane desalination system operation parameters on membrane colloidal fouling, including initial permeate flux, inlet Reynolds number, feed spacers, and feed solution silica particle concentration were also investigated by both CFD simulations and experiments to provide references in future membrane system design and upgrade.

In Chapter 5, the vibration enhanced reverse osmosis technology proposed in Chapter 2 was adopted here to confirm its effectiveness in membrane colloidal fouling control for up to 12 hours operation time. Both CFD simulations and experimental results show the colloidal fouling has a huge influence on the membrane performance with up to 47% of the permeate flux decline and 1.77 of the NaCl CP modulus within 12 hours. Additionally, membrane performance can be improved by vibration enhanced reverse osmosis technique for all 7 system parameter combinations investigated in this study. Membrane *NaCl* CP modulus decreases and the permeate flux under the influence of colloidal fouling increases as the vibration frequency increases up to 60 Hz, with a constant vibration amplitude. By comparing the 60 Hz vibration and no vibration cases in case set 2 with Re = 200, a maximum 60% improvement of the normalized permeate flux and 25% reduction of the *NaCl* accumulation after 12 hours was found. This improvement is less obvious in cases with high Reynolds number (Re = 600), since its shear rate near the membrane surface is already high.

In Chapter 6, traditional centrifugal reverse osmosis (CRO) technology was introduced and a new CRO concept was proposed to reduce the energy consumption and device size. The area of effective membrane surface increases by 300% compared with traditional CRO device in the same device size. Energy consumption estimations of 6 different new CRO devices were performed using CFD simulations. Results show that the energy cost of the new CRO concept is competitive compared with current medium and large size SWRO systems, while the capital cost is only 0.1% of the medium and large size SWRO systems. Finally, operation cost estimation was performed with the

help of GE RO tools. Results show that, for the new CRO device, the initial capital investment is 25240.32 US$ and the annual operation cost is 1529.85 US$. This operation cost is 30% lower compared with the convectional membrane desalination plant. Return on Investment (ROI) study also shows that a total profit over 60k USD and 87% of the ROI can be achieved within 30 years operation of the new CRO system.

7.2. Future work

Areas of potential and future research are listed below:

For the numerical model of membrane colloidal fouling:

(1) Developing a three-dimensional fouling model instead of the existing two-dimensional one for better prediction of the fouling layer distribution.

(2) In the current study, the porosity of the porous cake was assumed to be a constant. Future studies with the cake porosity as a variable would be useful.

(3) More system parameters can be investigated including inlet *NaCl* concentrations, equivalent diameters of the colloidal particle, etc.

(4) Extending the application of this fouling model to other colloids such as alginic acid.

For the vibration enhanced reverse osmosis technology:

(1) To save the power and equipment costs, systematical energy consumption studies about the optimal vibration frequency and amplitude would be useful.

(2) Experimental investigations and simulations of this technique about mitigating other types of fouling, such as organic fouling and biofouling.

(3) Besides the plate and frame module studied here, the application of this technique can be extended to other conventional RO membrane modules, such as spiral wound module, tubular module, and hollow fiber module.

(4) Developing a passive vibration approach, such as magnets, to reduce the energy cost and system capital cost.

For the new centrifugal reverse osmosis concept:

(1) Developing a module combining the vibration enhanced reverse osmosis technology with the centrifugal reverse osmosis concept, which takes the benefits from both technologies.

(2) Detailed structural analysis of the critical parts including bearing housing, permeate cylinder, and rotor, to increase the system reliability.

(3) Parametric studies investigating the effect of the thickness and length of the membrane pack, radius and mass of the device, rotating speed, and properties of the inlet feed solution on the performance of the centrifugal reverse osmosis concept.

(4) Developing a ‘batch mode’ concept by driving multiple centrifuges from a single motor to further reduce the energy consumption and increase the system reliability.

REFERENCES

[1] United Nations, Transforming our world: the 2030 Agenda for Sustainable Development. Resolution adopted by the General Assembly on 25 September 2015, A/RES/70/1 (2015) 1–35. http://www.un.org/en/development/desa/population/migration/generalassembly/docs/globalcompact/A_RES_70_1_E.pdf.

[2] WHO/UNICEF Joint Monitoring Programme for Water Supply and Sanitation, Progress on drinking water, sanitation and hygiene: 2017 update and SDG baselines, 2017. doi:10.1111 / tmi.12329.

[3] N. Ghaffour, The challenge of capacity-building strategies and perspectives for desalination for sustainable water use in MENA, Desalin. Water Treat. 5 (2009) 48–53. doi:10.5004/dwt.2009.564.

[4] N. Ghaffour, T.M. Missimer, G.L. Amy, Technical review and evaluation of the economics of water desalination: Current and future challenges for better water supply sustainability, Desalination. 309 (2013) 197–207. doi:10.1016/j.desal.2012.10.015.

[5] C. Charcosset, A review of membrane processes and renewable energies for desalination, Desalination. 245 (2009) 214–231. doi:10.1016/j.desal.2008.06.020.

[6] J. Mulder, Basic principles of membrane technology, Springer Science & Business Media, 2012.

[7] D.E. Meyer, M. Williams, D. Bhattacharyya, Reverse osmosis, Kirk-Othmer Encycl. Chem. Technol. (2005).

[8] P. Bacchin, M. Meireles, P. Aimar, Modelling of filtration: From the polarised layer to deposit formation and compaction, Desalination. 145 (2002) 139–146. doi:10.1016/S0011-9164(02)00399-5.

[9] S. Kim, E.M. V Hoek, Modeling concentration polarization in reverse osmosis processes, Desalination. 186 (2005) 111–128. doi:10.1016/j.desal.2005.05.017.

[10] J.G. Wijmans, S. Nakao, J.W.A. Van Den Berg, F.R. Troelstra, C.A. Smolders, Hydrodynamic resistance of concentration polarization boundary layers in ultrafiltration, J. Memb. Sci. (1985). doi:10.1016/S0376-7388(00)80534-7.

[11] E. Lyster, Y. Cohen, Numerical study of concentration polarization in a rectangular reverse osmosis membrane channel: Permeate flux variation and hydrodynamic end effects, J. Memb. Sci. 303 (2007) 140–153. doi:10.1016/j.memsci.2007.07.003.

[12] R. Ghidossi, D. Veyret, P. Moulin, Computational fluid dynamics applied to membranes: State of the art and opportunities, Chem. Eng. Process. Process Intensif. 45 (2006) 437–454. doi:10.1016/j.cep.2005.11.002.

[13] L. Song, S. Ma, Numerical studies of the impact of spacer geometry on concentration polarization in spiral wound membrane modules, Ind. Eng. Chem. Res. 44 (2005) 7638–7645. doi:10.1021/ie048795w.

[14] A.I. Cavaco Morão, A.M. Brites Alves, V. Geraldes, Concentration polarization in a reverse osmosis/nanofiltration plate-and-frame membrane module, J. Memb. Sci. 325 (2008) 580–591. doi:10.1016/j.memsci.2008.08.030.

[15] S. Wardeh, H.P. Morvan, CFD simulations of flow and concentration polarization in spacer-filled channels for application to water desalination, Chem. Eng. Res. Des. 86 (2008) 1107–1116. doi:10.1016/j.cherd.2008.04.010.

[16] A. Chaudhuri, A. Jogdand, Permeate flux decrease due to concentration polarization in a closed roto-dynamic reverse osmosis filtration system, Desalination. 402 (2017) 152–161. doi:10.1016/j.desal.2016.10.005.

[17] V. Geraldes, V. Semião, M.N. De Pinho, Flow management in nanofiltration spiral wound modules with ladder-type spacers, J. Memb. Sci. 203 (2002) 87–102. doi:10.1016/S0376-7388(01)00753-0.

[18] G.A. Fimbres-Weihs, D.E. Wiley, D.F. Fletcher, Unsteady flows with mass transfer in narrow zigzag spacer-filled channels: A numerical study, Ind. Eng. Chem. Res. 45 (2006) 6594–6603. doi:10.1021/ie060243l.

[19] J. Gregory, Particles in water: properties and processes, CRC Press, 2005.

[20] I. Huisman, C. Trägårdh, Particle transport in crossflow microfiltration I. Effects of hydrodynamics and diffusion, Chem. Eng. Sci. 54 (1999) 271–280. doi:10.1016/S0009-2509(98)00222-X.

[21] R.W. Field, D. Wu, J.A. Howell, B.B. Gupta, Critical flux concept for microfiltration fouling, J. Memb. Sci. 100 (1995) 259–272. doi:10.1016/0376-7388(94)00265-Z.

[22] Y.P. Zhang, A.W.K. Law, A.G. Fane, Determination of critical flux by mass balance technique combined with direct observation image analysis, J. Memb. Sci. 365 (2010) 106–113. doi:10.1016/j.memsci.2010.08.047.

[23] D. Lisitsin, D. Hasson, R. Semiat, Critical flux detection in a silica scaling RO system, Desalination. 186 (2005) 311–318. doi:10.1016/j.desal.2005.06.007.

[24] H.J. Tanudjaja, W. Pee, A.G. Fane, J.W. Chew, Effect of spacer and crossflow velocity on the critical flux of bidisperse suspensions in microfiltration, J. Memb. Sci. 513 (2016) 101–107. doi:10.1016/j.memsci.2016.04.040.

[25] T.N.P. Nguyen, Y.C. Su, J.R. Pan, C. Huang, Comparison of membrane foulants occurred under different sub-critical flux conditions in a membrane bioreactor (MBR), Bioresour. Technol. 166 (2014) 389–394. doi:10.1016/j.biortech.2014.05.073.

[26] P. Bacchin, P. Aimar, R.W. Field, Critical and sustainable fluxes: Theory, experiments and applications, J. Memb. Sci. 281 (2006) 42–69. doi:10.1016/j.memsci.2006.04.014.

[27] A.G. Fane, H. Li, P. Beatson, P.R. Neal, Critical Flux Phenomena and its Implications for Fouling in Spiral-Wound Modules, in: IDA World Congr. Desalin. Water Reuse, 1999.

[28] X. Zhu, M. Elimelech, Colloidal fouling of reverse osmosis membranes:

Measurements and fouling mechanisms, Environ. Sci. Technol. 31 (1997) 3654–3662. doi:10.1021/es970400v.

[29] S.G. Yiantsios, A.J. Karabelas, The effect of colloid stability on membrane fouling, Desalination. 118 (1998) 143–152. doi:10.1016/S0011-9164(98)00110-6.

[30] E.M. V Hoek, M. Elimelech, Cake-Enhanced Concentration Polarization: A New Fouling Mechanism for Salt-Rejecting Membranes, Environ. Sci. Technol. 37 (2003) 5581–5588. doi:10.1021/es0262636.

[31] E.M. V. Hoek, A.S. Kim, M. Elimelech, Influence of Crossflow Membrane Filter Geometry and Shear Rate on Colloidal Fouling in Reverse Osmosis and Nanofiltration Separations, Environ. Eng. Sci. 19 (2002) 357–372. doi:10.1089/109287502320963364.

[32] B.P. Boudreau, The diffusive tortuosity of fine-grained unlithified sediments, Geochim. Cosmochim. Acta. 60 (1996) 3139–3142. doi:10.1016/0016-7037(96)00158-5.

[33] A.S. Kim, H. Chen, Diffusive tortuosity factor of solid and soft cake layers: A random walk simulation approach, J. Memb. Sci. 279 (2006) 129–139. doi:10.1016/j.memsci.2005.11.042.

[34] G.H. Neale, W.K. Nader, Prediction of transport processes within porous media: Diffusive flow processes within an homogeneous swarm of spherical particles, AIChE J. 19 (1973) 112–119. doi:10.1002/aic.690190116.

[35] T.H. Chong, A.G. Fane, Reverse osmosis desalination and reclamation : control of colloidal and biofouling, 2008. http://repository.ntu.edu.sg/handle/10356/12062.

[36] S.T. V Sim, A.H. Taheri, T.H. Chong, W.B. Krantz, A.G. Fane, Colloidal metastability and membrane fouling - Effects of crossflow velocity, flux, salinity and colloid concentration, J. Memb. Sci. 469 (2014) 174–187. doi:10.1016/j.memsci.2014.06.020.

[37] Y. Lee, M.M. Clark, A numerical model of steady-state permeate flux during cross-flow ultrafiltration, Desalination. 109 (1997) 241–251. doi:10.1016/S0011-9164(97)00070-2.

[38] T.H. Chong, F.S. Wong, A.G. Fane, Implications of critical flux and cake enhanced osmotic pressure (CEOP) on colloidal fouling in reverse osmosis: Modeling approach, J. Memb. Sci. 314 (2008) 101–111. doi:10.1016/j.memsci.2008.01.030.

[39] G.A. Fimbres Weihs, D.E. Wiley, CFD analysis of tracer response technique under cake-enhanced osmotic pressure, J. Memb. Sci. 449 (2014) 38–49. doi:10.1016/j.memsci.2013.08.015.

[40] S. Jamaly, N.N. Darwish, I. Ahmed, S.W. Hasan, A short review on reverse osmosis pretreatment technologies, Desalination. 354 (2014) 30–38. doi:10.1016/j.desal.2014.09.017.

[41] R. Semiat, I. Sutzkover, D. Hasson, Characterization of the effectiveness of silica anti-scalants, Desalination. 159 (2003) 11–19. doi:10.1016/S0011-9164(03)90041-5.

[42] M.Y. Jaffrin, Dynamic shear-enhanced membrane filtration: A review of rotating disks, rotating membranes and vibrating systems, J. Memb. Sci. 324 (2008) 7–25. doi:10.1016/j.memsci.2008.06.050.

[43] M.C. Amiri, M. Samiei, Enhancing permeate flux in a RO plant by controlling membrane fouling, Desalination. 207 (2007) 361–369. doi:10.1016/j.desal.2006.08.011.

[44] E. Neofotistou, K.D. Demadis, Use of antiscalants for mitigation of silica (SiO2) fouling and deposition: fundamentals and applications in desalination systems, Desalination. 167 (2004) 257–272.

[45] R. Semiat, I. Sutzkover, D. Hasson, Technique for evaluating silica scaling and its inhibition in RO desalting, Desalination. 140 (2001) 181–193. doi:10.1016/S0011-9164(01)00367-8.

[46] M. Chaussemier, E. Pourmohtasham, D. Gelus, N. Pécoul, H. Perrot, J. Lédion, H. Cheap-Charpentier, O. Horner, State of art of natural inhibitors of calcium carbonate scaling. A review article, Desalination. 356 (2015) 47–55. doi:10.1016/j.desal.2014.10.014.

[47] A. Sweity, Z. Ronen, M. Herzberg, Induced organic fouling with antiscalants in seawater desalination, Desalination. 352 (2014) 158–165. doi:10.1016/j.desal.2014.08.018.

[48] J. Duiven, B. Rietman, W. Van De Ven, Application of the membrane fouling simulator to determine biofouling potential of antiscalants in membrane filtration, J. Water Supply Res. Technol. - AQUA. 59 (2010) 111–119. doi:10.2166/aqua.2010.041.

[49] R. Bian, K. Yamamoto, Y. Watanabe, The effect of shear rate on controlling the concentration polarization and membrane fouling, Desalination. 131 (2000) 225–236. doi:10.1016/S0011-9164(00)90021-3.

[50] K. Takata, K. Yamamoto, R. Bian, Y. Watanabe, Removal of humic substances with vibratory shear enhanced processing membrane filtration, Desalination. (1998). doi:10.1016/S0011-9164(98)00118-0.

[51] J. Nuortlla-joklnen, A. Kuparinen, M. Nystrm, Tailoring an economical membrane process for intemal purification in the paper industry, Desalination. 119 (1998) 11–19.

[52] J. Nuortila-Jokinen, M. Nyström, Membrane filtration of paper mill coating effluent, in: Proc. 8th World Congr. Filtr. Bright. UK, 2000: pp. 1015–1018.

[53] S.C. Low, H.H. Juan, L.K. Siong, A combined VSEP and membrane bioreactor system, Desalination. 183 (2005) 353–362. doi:10.1016/j.desal.2005.04.028.

[54] M.M. Dal-Cin, C.N. Lick, A. Kumar, S. Lealess, Dispersed phase back transport during ultrafiltration of cutting oil emulsions with a spinning membrane disc geometry, J. Memb. Sci. 141 (1998) 165–181. doi:10.1016/S0376-7388(97)00304-9.

[55] B. Culkin, A.D. Armando, N.L. Inter-, New separation system extends the use of membranes, Filtr. Sep. 29 (1992) 376–378. doi:http://dx.doi.org/10.1016/0015-1882(92)80196-P.

[56] T. Li, A.W.K. Law, M. Cetin, A.G. Fane, Fouling control of submerged hollow fibre membranes by vibrations, J. Memb. Sci. 427 (2013) 230–239. doi:10.1016/j.memsci.2012.09.031.

[57] M.R. Bilad, G. Mezohegyi, P. Declerck, I.F.J. Vankelecom, Novel magnetically induced membrane vibration (MMV) for fouling control in membrane bioreactors, Water Res. 46 (2012) 63–72. doi:10.1016/j.watres.2011.10.026.

[58] O. Al-Akoum, L.H. Ding, M.Y. Jaffrin, Microfiltration and ultrafication of UHT skim milk with a vibrating membrane module, Sep. Purif. Technol. 28 (2002) 219–234. doi:10.1016/S1383-5866(02)00076-X.

[59] W. Shi, M.M. Benjamin, Fouling of RO membranes in a vibratory shear enhanced filtration process (VSEP) system, J. Memb. Sci. 331 (2009) 11–20. doi:10.1016/j.memsci.2008.12.027.

[60] W. Shi, M.M. Benjamin, Effect of shear rate on fouling in a Vibratory Shear Enhanced Processing (VSEP) RO system, J. Memb. Sci. 366 (2011) 148–157. doi:10.1016/j.memsci.2010.09.051.

[61] W. Shi, M.M. Benjamin, Membrane interactions with NOM and an adsorbent in a vibratory shear enhanced filtration process (VSEP) system, J. Memb. Sci. 331 (2009) 11–20. doi:10.1016/j.memsci.2008.12.027.

[62] A. Rahardianto, W.Y. Shih, R.W. Lee, Y. Cohen, Diagnostic characterization of gypsum scale formation and control in RO membrane desalination of brackish water, J. Memb. Sci. 279 (2006) 655–668. doi:10.1016/j.memsci.2005.12.059.

[63] H.M. Yeh, T.W. Cheng, Analysis of the slip effect on the permeate flux in membrane ultrafiltration, J. Memb. Sci. 154 (1999) 41–51. doi:10.1016/S0376-7388(98)00272-5.

[64] S. Chellam, M.R. Wiesner, C. Dawson, Slip at a uniformly porous boundary: effect on fluid flow and mass transfer, J. Eng. Math. 26 (1992) 481–492. doi:10.1007/BF00042765.

[65] O. Al Akoum, M.Y. Jaffrin, L. Ding, P. Paullier, C. Vanhoutte, An hydrodynamic investigation of microfiltration and ultrafiltration in a vibrating membrane module, J. Memb. Sci. 197 (2002) 37–52. doi:10.1016/S0376-7388(01)00602-0.

[66] Hydranautics Corporate, Membrane element, SWC6 MAX, (2013). http://www.membranes.com/docs/8inch/SWC6MAX.pdf (accessed May 28, 2018).

[67] G. Schock, A. Miquel, Mass transfer and pressure loss in spiral wound modules, Desalination. 64 (1987) 339–352. doi:10.1016/0011-9164(87)90107-X.

[68] W.C. Reynolds, The potential and limitations of direct and large eddy simulations. ' 'Whither Turbulence? Turbulence at the Crossroads: Proceedings of a Workshop Held at Cornell University, Ithaca, NY, March 22–24, 1989, in: J.L. Lumley (Ed.), Springer Berlin Heidelberg, Berlin, Heidelberg, 1990: pp. 313–343. doi:10.1007/3-540-52535-1_52.

[69] P. Sagaut, Large eddy simulation for incompressible flows: an introduction, Springer Science & Business Media, 2006.

[70] M. Lohász, P. Rambaud, C. Benocci, LES Simulation of Ribbed Square Duct Flow with FLUENT and Comparison with PIV Data, Conf. Model. Fluid Flow 12th Int. Conf. Fluid Flow Technol. (2003) 1–8.

[71] M.P. Martin, U. Piomelli, G. Candler, Subgrid-scale models for compressible large-eddy simulation, Theor. Comput. Fluid Dyn. 13 (2000) 361–376.

[72] B.E. Poling, J.M. Prausnitz, J.P. O'connell, The properties of gases and liquids, Mcgraw-hill New York, 2001.

[73] S. Sourirajan, Reverse osmosis., London, UK: Logos Press Ltd., 1970.

[74] V. Geraldes, V. Semião, M.N. De Pinho, Flow and mass transfer modelling of nanofiltration, J. Memb. Sci. 191 (2001) 109–128. doi:10.1016/S0376-7388(01)00458-6.

[75] C.T. Baird, Guide to Petroleum Product Blending, HPI Consultants, Inc., Houst. (1989).

[76] C.P. Koutsou, S.G. Yiantsios, A.J. Karabelas, Numerical simulation of the flow in a plane-channel containing a periodic array of cylindrical turbulence promoters, J. Memb. Sci. 231 (2004) 81–90. doi:10.1016/j.memsci.2003.11.005.

[77] N. Alkhamis, D.E. Oztekin, A.E. Anqi, A. Alsaiari, A. Oztekin, Numerical study of gas separation using a membrane, Int. J. Heat Mass Transf. 80 (2015) 835–843. doi:10.1016/j.ijheatmasstransfer.2014.09.072.

[78] E. Lyster, M. man Kim, J. Au, Y. Cohen, A method for evaluating antiscalant retardation of crystal nucleation and growth on RO membranes, J. Memb. Sci. 364 (2010) 122–131. doi:10.1016/j.memsci.2010.08.020.

[79] A.R. Bartman, E. Lyster, R. Rallo, P.D. Christofides, Y. Cohen, Mineral scale monitoring for reverse osmosis desalination via real-time membrane surface image analysis, Desalination. 273 (2011) 64–71. doi:10.1016/j.desal.2010.10.021.

[80] P. Dydo, M. Turek, J. Ciba, K. Wandachowicz, J. Misztal, The nucleation kinetic aspects of gypsum nanofiltration membrane scaling, Desalination. 164 (2004) 41–52. doi:10.1016/S0011-9164(04)00154-7.

[81] G.P. Keir, Coupled modelling of hydrodynamics and mass transfer in membrane filtration, Deakin University, 2012.

[82] X. Su, W. Li, A. Palazzolo, S. Ahmed, Concentration polarization and permeate flux variation in a vibration enhanced reverse osmosis membrane module, Desalination. 433 (2018) 75–88. doi:10.1016/j.desal.2018.01.001.

[83] J. Schwinge, P.R. Neal, D.E. Wiley, A.G. Fane, Estimation of foulant deposition

across the leaf of a spiral-wound module, Desalination. 146 (2002) 203–208. doi:10.1016/S0011-9164(02)00471-X.

[84] R.H. Davis, Modeling of fouling of crossflow microfiltration membranes, Sep. Purif. Methods. 2119 (1992) 75–126. doi:10.1080/03602549208021420.

[85] P.C. Carman, Fluid Flow Through Granular Beds, Trans. - Inst. Chem. Eng. 15 (1937) 150–166. citeulike-article-id:711017.

[86] Y.P. Zhang, T.H. Chong, A.G. Fane, A. Law, H.G.L. Coster, H. Winters, Implications of enhancing critical flux of particulates by AC fields in RO desalination and reclamation, Desalination. 220 (2008) 371–379. doi:10.1016/j.desal.2007.02.043.

[87] P.R. Neal, H. Li, A.G. Fane, D.E. Wiley, The effect of filament orientation on critical flux and particle deposition in spacer-filled channels, J. Memb. Sci. 214 (2003) 165–178. doi:10.1016/S0376-7388(02)00500-8.

[88] H. Li, A.G. Fane, H.G.L. Coster, S. Vigneswaran, An assessment of depolarisation models of crossflow microfiltration by direct observation through the membrane, J. Memb. Sci. 172 (2000) 135–147. doi:10.1016/S0376-7388(00)00334-3.

[89] D.R. Trettin, M.R. Doshi, Limiting flux in ultrafiltration of macromolecular solutions, Chem. Eng. Commun. 4 (1980) 507–522. doi:10.1080/00986448008935925.

[90] A. Einstein, Investigations on the Theory of Brownian Movement, Courier Corporation, 1956.

[91] G. Green, G. Belfort, Fouling of Ultrafiltration Membranes: Lateral Migration and the Particle Trajectory Model., Desalination. 35 (1980) 129–147. doi:10.1016/S0011-9164(00)88607-5.

[92] A.L. Zydney, C.K. Colton, a Concentration Polarization Model for the Filtrate

Flux in Cross-Flow Microfiltration of Particulate Suspensions, Chem. Eng. Commun. 47 (1986) 1–21. doi:10.1080/00986448608911751.

[93] M.R. Wiesner, S. Chellam, Mass transport considerations for pressure-driven membrane processes, J. / Am. Water Work. Assoc. 84 (1992) 88–95.

[94] J.S. Knutsen, R.H. Davis, Deposition of foulant particles during tangential flow filtration, J. Memb. Sci. 271 (2006) 101–113. doi:10.1016/j.memsci.2005.06.060.

[95] C. Paz, E. Suarez, A. Eiris, J. Porteiro, Development of a Predictive CFD Fouling Model for Diesel Engine Exhaust Gas Systems, Heat Transf. Eng. 34 (2013) 674–682. doi:Doi 10.1080/01457632.2012.738321.

[96] H. El-Batsh, Modeling Particle Deposition on Compressor and Turbine Blade Surfaces, Vienna University of Techhnology, 2001.

[97] M. Ettlinger, Highly Dispersed Metallic Oxides Produced by the AEROSIL® Process, Tech. Bull. Pigment. (1993).

[98] Thomas D. Wolfe, Membrane Process Optimization Technology, (2003).

[99] A.I. Radu, L. Bergwerff, M.C.M. van Loosdrecht, C. Picioreanu, A two-dimensional mechanistic model for scaling in spiral wound membrane systems, Chem. Eng. J. 241 (2014) 77–91. doi:10.1016/j.cej.2013.12.021.

[100] C. Picioreanu, J.S. Vrouwenvelder, M.C.M. van Loosdrecht, Three-dimensional modeling of biofouling and fluid dynamics in feed spacer channels of membrane devices, J. Memb. Sci. 345 (2009) 340–354. doi:10.1016/j.memsci.2009.09.024.

[101] S. Lee, J. Cho, M. Elimelech, Influence of colloidal fouling and feed water recovery on salt rejection of RO and NF membranes, Desalination. 160 (2004) 1–12. doi:10.1016/S0011-9164(04)90013-6.

[102] A.R. Da Costa, A.G. Fane, D.E. Wiley, Spacer characterization and pressure drop

modelling in spacer-filled channels for ultrafiltration, J. Memb. Sci. 87 (1994) 79–98. doi:10.1016/0376-7388(93)E0076-P.

[103] J. Schwinge, D.E. Wiley, D.F. Fletcher, A CFD study of unsteady flow in narrow spacer-filled channels for spiral-wound membrane modules, Desalination. 146 (2002) 195–201. doi:10.1016/S0011-9164(02)00470-8.

[104] A.I. Radu, L. Bergwerff, M.C.M. van Loosdrecht, C. Picioreanu, Combined biofouling and scaling in membrane feed channels: a new modeling approach., Biofouling. 31 (2015) 83–100. doi:10.1080/08927014.2014.996750.

[105] J. Schwinge, D.E. Wiley, D.F. Fletcher, Simulation of the Flow around Spacer Filaments between Channel Walls. 2. Mass-Transfer Enhancement, Ind. Eng. Chem. Res. 41 (2002) 4879–4888. doi:10.1021/ie011015o.

[106] C.R. Bartels, M. Wilf, K. Andes, J. Iong, Design considerations for wastewater treatment by reverse osmosis., Water Sci. Technol. 51 (2005) 473–482.

[107] W. Li, X. Su, A. Palazzolo, S. Ahmed, E. Thomas, Reverse osmosis membrane, seawater desalination with vibration assisted reduced inorganic fouling, Desalination. 417 (2017) 102–114. doi:10.1016/j.desal.2017.05.016.

[108] C.A. Grenci, Centrifugal reverse osmosis for desalination, 1968.

[109] P. Wild, G. Vickers, N. Djilali, The fundamental principles and design considerations for the implementation of centrifugal reverse osmosis, Proc. Inst. Mech. Eng. Part E J. Process Mech. Eng. 211 (1997) 67–81. doi:10.1243/0954408971529566.

[110] P.M. Wild, G.W. Vickers, D.A. Hopkin, A. Moilliet, Centrifugal reverse-osmosis desalination unit, 1989.

[111] D.A. Hopkin, P.M. Wild, G.W. Vickers, A. Moilliet, Centrifugal reverse-osmosis desalination unit incorporating an annular membrane cartridge, 2000.

[112] A. Bergen, N. Djilali, T.M. Fyles, G.W. Vickers, P.M. Wild, An experimental assessment of centrifugal membrane separation using spiral wound RO membrane elements, Desalination. 154 (2003) 225–232. doi:10.1016/S0011-9164(03)80037-1.

[113] A. Bergen, T.M. Fyles, D.S. Lycon, G.W. Vickers, P. Wild, Flux enhancement in reverse osmosis using centrifugal membrane separation, J. Memb. Sci. 176 (2000) 257–266. doi:10.1016/S0376-7388(00)00473-7.

[114] N. Voutchkov, Energy use for membrane seawater desalination - current status and trends, Desalination. 431 (2018) 2–14. doi:10.1016/j.desal.2017.10.033.

[115] G.E.W.& P. Technologies, RO tools - cost of operation, (2017). http://rotools.gewater.com/Cost-Of-Operations (accessed March 13, 2017).

[116] T.M. Fyles, D.S. Lycon, Fouling reduction using centrifugal membrane separation, J. Memb. Sci. 176 (2000) 267–276.

[117] C. of College Station, Coollege Station Utilies - Electric Rates, (2018). http://cstx.gov/index.aspx?page=3852 (accessed June 30, 2018).